EPFL

Purely Organic Optical Sensor for Broad-Range and Reversible Oxygen Sensing

Présentée le 13 décembre 2021

Faculté des sciences et techniques de l'ingénieur
Laboratoire de la matière molle
Programme doctoral en science et génie des matériaux

pour l'obtention du grade de Docteur ès Sciences

par

Efe ARMAGAN

Acceptée sur proposition du jury

Dr Y. Leterrier, président du jury
Prof. E. Amstad, Prof. R. M. Rossi, directeurs de thèse
Dr L. Boesel , rapporteur
Dr T. Kodger, rapporteur
Dr F. Sorin, rapporteur

■ École
polytechnique
fédérale
de Lausanne

2021

Acknowledgements

I meet very special people who helped me personally or professionally in achieving this PhD thesis. I would like to thank all of you for your physical and mental contributions before starting the list;

- Firstly, I would like to thank my thesis director, Prof. Esther Amstad, for accepting me as an external PhD student to her lab. She pushed me to learn how to organize my research plan and experiments that I was not talented enough before starting my PhD. Although I am not physically in Lausanne, she always replies to my questions very quickly that helped me to forward my research without wasting time. I am very proud to obtain my PhD degree from her lab.

- I owe a debt of gratitude to my group leader in Empa St. Gallen, Prof. René Rossi. His door was always open to me when I wanted to make any scientific or work discussion. He is a great role model and indeed a great mentor to me. I always remember him while I am organizing my research plan.

- I would like to say special thanks to our amazing postdoc, Dr. Kongchang Wei. He always pushed and drove me to get better every time. I can't make this success without his scientific contributions. It was a great pleasure to work with him in the same lab.

- Prof. Giuseppino Fortunato for helping me anytime I need. I will never forget you. Rest in peace…

- Prof. Luciano Boesel for all scientific contributions since the first day of my PhD thesis.

- I also want to thank Alexis Anthis, Khushdeep Sharma, Chieh-Szu Huang, Sebastian Ulrich, Haijan Zhang, and Jialuo Luo for their special help and support during my PhD Thesis

- Dr. Peng Zeng from ETH ScopeM for helping me in sample imaging with TEM microscopy

- Ann-Christine Vetsch for helping me with all lab orderings and bureaucratic problems.

- All other PhD and Master students in Empa St. Gallen for their kind friendship and nice coffee breaks.

- The Turkish community in St. Gallen, Ezgi Bülbül, Berna Şentürk, Sinem Özer, Gökçe Yazgan and Emel Mert Aslan for hanging out with me and making me very happy even in most depressing winter time. I never forget our beer time which makes me feel in my comfort zone.

- Çağdaş Aslan, my beer and basketball buddy…. probably I feel very alone at the weekends if I don't meet you. Thanks for sharing great time with me.

- Akin Gursoy for his great support either personally or professionally in the lab or outside the lab. It was a great pleasure to work with you in D floor labs. I never forget your helps!!

- All my virtual twitter buddies for having fun together when I feel very depressed. I can't make this success without your tons of interactions……

- Guney Atilgan for their endless support during my PhD thesis

- "Goygoy ve Ötesi", Alihan Çelik, Onur Demir, Ekrem Taşer, Hikmet Coşkun, Ozan Mert, Faruk Ulusoy and Meriç İşgenç for feeling me in Istanbul….

- My other friends in Sabanci University, Çağıl Mayda, Yasin Razlık, Canhan Şen, Onur Özensoy, Burçin Üstbaş and Billur Seviniş, for their nice friendship

- Of course, I would like to thank my parents Gülden and Kadri Armağan for all the support they gave me ever since. I can't achieve this success without their endless help and support. They were always with me whenever I call "mommy" or "daddy". Most importantly, they thought me how to become a good person. I am very proud of being "minik oğlunuz"….. I love you!!

- Finally, I want to send a very warm thank to my brother, Emre Armağan… He is always my role model in this life. Whenever I have any problem, I know my brother is there. I can ask for a help anytime, this feels me very comfortable throughout my life. I hope you will move to Europe and we will see each other more frequently. I am also very proud of being your sibling…

Abstract

Oxygen (O_2) molecule is of paramount importance in nature, and it takes part in several biological and chemical activities such as energy generation, cellular respiration, and food deterioration, to name a few. Detection of O_2 concentration is of extreme importance in many application fields to monitor the above-mentioned activities. In the last decade, optical oxygen sensors have become a popular research topic due to the need for continuous, reversible, and non-destructive O_2 sensing. Rational design of O_2 sensing materials, optimal integration of reporter luminophore chemistry with the other sensor components (encapsulation matrix, support material, additives), and simple fabrication procedures are the main bottlenecks and challenges in producing simple and affordable optical O_2 sensors with stable and predictable sensing performance. The traditional approach, such as developing metal ion-based luminophores and integrating these sensing units into organic/inorganic matrix have shown their utility in many optical O_2 sensor systems. However, a high degree of toxicity of metal ions hampers the effective use of such systems in many application areas. Therefore, it is crucial to develop purely organic optical O_2 sensors to overcome the above-mentioned problem. Although a few studies investigate the O_2 sensing performance of organic optical O_2 sensors, their narrow O_2 sensitivity range and poor reversibility are two main drawbacks of these sensors. In this thesis, I study improving the O_2 sensitivity range of organic optical O_2 sensors with good sensing reversibility by developing diamine-based organic O_2 sensing material and embedding these indicators within a polymer matrix.

In the first part, I focused on fabricating a diamine-based organic O_2 sensing unit with a rigid crosslinking network. Firstly, a new luminophore was synthesized through a one-pot hydrothermal synthesis using p-phenylenediamine (PPD) and urea. As-synthesized nanoparticles show multi-emissive behavior with three main emission centers. The multi-emission was attributed to the ensemble of chemical structures resulting from self-oxidation of p-phenylenediamine under oxidative conditions. Each emissive state shows oxygen quenching within the range of 0-8% O_2. To improve that O_2 sensing range, I selected using highly rigid linkers, instead of urea, between each diamine unit. Therefore, imidization

chemistry was used to enhance the structural rigidity of the PPD-based sensing unit. I could obtain an O_2 sensitivity range of 0-16% O_2, whereas the similar system could only detect O_2 in the range of 0-8% O_2. I found that the structural rigidity leads to efficient room-temperature phosphorescence (RTP) mechanism, enabling O_2 quenching at higher O_2 concentrations.

In the second part, I focused on polymer matrix selection, O_2 permeability and the shape of the sensor on O_2 sensing performance. Polyimide-based O_2 sensing materials were separately embedded into conventional poly(vinyl alcohol) (PVA) and PVA hydrogel film to investigate the O_2 sensitivity range. Luminophores integrated into PVA hydrogels show O_2 response at physiological O_2 range (0-21% O_2). This improvement was attributed to the high O_2 permeability of PVA hydrogel compared to conventional PVA polymer. Finally, the response time of my sensor was enhanced when the luminophores were embedded into wet-spun PVA hydrogel fiber due to its high surface-to-volume ratio. The fabricated metal ion-free, purely organic sensors that enable continuous, repetitive, and fast detection of O_2 within a physiological O_2 sensing range are appealing, especially for monitoring packaged food, biomonitoring, and biosensing applications.

Keywords

Zusammenfassung

Das Sauerstoffmolekül (O_2) ist in der Natur von überragender Bedeutung und nimmt an verschiedenen biologischen und chemischen Aktivitäten teil, wie z. B. der Energieerzeugung, der Zellatmung und dem Verfall von Lebensmitteln, um nur einige zu nennen. Die Erfassung der O_2-Konzentration ist in vielen Anwendungsbereichen von großer Bedeutung, um die oben genannten Aktivitäten zu überwachen. Im letzten Jahrzehnt sind optische Sauerstoffsensoren zu einem beliebten Forschungsthema geworden, da eine kontinuierliche, wiederholbare und zerstörungsfreie O_2-Messung erforderlich ist. Rationales Design von O2-Sensormaterialien, optimale Integration der Reporter-Luminophorchemie mit den anderen Sensorkomponenten (Verkapselungsmatrix, Trägermaterial, Additive) und einfache Herstellungsverfahren sind die größten Engpässe und Herausforderungen bei der Herstellung einfacher und erschwinglicher optischer O_2-Sensoren mit stabiler und vorhersagbarer Sensorleistung. Der traditionelle Ansatz, wie die Entwicklung von Luminophoren auf Metallionenbasis und die Integration dieser Sensoreinheiten in eine organische/anorganische Matrix, hat seine Nützlichkeit in vielen optischen O_2-Sensorsystemen gezeigt. Allerdings behindert eine hohe Toxizität der Metallionen den effektiven Einsatz solcher Systeme in vielen Anwendungsbereichen. Daher ist es entscheidend, rein organische optische O_2-Sensoren zu entwickeln, um das oben erwähnte Problem zu überwinden. Obwohl einige wenige Studien die O_2-Erfassungsleistung von organischen optischen O_2-Sensoren untersuchen, sind der fehlende O_2-Empfindlichkeitsbereich und die schlechte Reversibilität zwei Hauptnachteile dieser Sensoren. In dieser Arbeit untersuche ich die Verbesserung des O_2-Empfindlichkeitsbereichs von organischen optischen O_2-Sensoren mit guter Sensorreversibilität durch die Entwicklung von organischem O_2-Sensormaterial auf Diaminbasis und die Einbettung dieser Indikatoren in eine Polymermatrix.

Im ersten Teil konzentrierte ich mich auf die Herstellung einer diaminbasierten organischen O_2-Sensoreinheit mit einem starren Vernetzungsnetzwerk. Zunächst wurde ein neues Luminophor durch eine Ein-Topf-Hydrothermalsynthese unter Verwendung von p-Phenylendiamin (PPD) und Harnstoff synthetisiert. Die so synthetisierten Nanopartikel zeigen ein multiemittierendes Verhalten mit drei Hauptemissionszentren. Die Mehrfachemission wurde auf

das Ensemble chemischer Strukturen zurückgeführt, die aus der Selbstoxidation von p-Phenylendiamin unter oxidativen Bedingungen resultieren. Jeder emittierende Zustand zeigt eine Sauerstofflöschung im Bereich von 0-8% O_2. Um diesen O_2-Erfassungsbereich zu verbessern, wählte ich die Verwendung von hochsteifen Linker, anstelle von Harnstoff, zwischen den einzelnen Diamineinheiten. Daher wurde die Imidisierungschemie verwendet, um die strukturelle Steifigkeit der PPD-basierten Sensoreinheit zu erhöhen. Wir konnten einen O_2-Empfindlichkeitsbereich von 0-16% O_2 erreichen, während das ähnliche System nur O_2 im Bereich von 0-8% O_2 erkennen konnte. Ich fand heraus, dass die strukturelle Steifigkeit zu einem effizienten Raumtemperatur-Phosphoreszenz (RTP)-Mechanismus führt und dadurch ein O_2-Löschen bei höheren O_2-Konzentrationen ermöglicht.

Im zweiten Teil konzentrierte ich mich auf die Auswirkungen der Auswahl der Polymermatrix und der Form des Sensors auf die O_2-Sensorleistung. Polyimid-basierte O_2-Sensormaterialien wurden separat in konventionellen Poly(vinylalkohol) (PVA) und PVA Hydrogel Film eingebettet, um den O_2-Empfindlichkeitsbereich zu untersuchen. Die in PVA-Hydrogelen integrierten Luminophore zeigen eine O_2-Antwort im physiologischen O_2-Bereich (0-21% O_2). Diese Verbesserung wurde auf die hohe O_2-Durchlässigkeit des PVA-Hydrogels im Vergleich zum herkömmlichen PVA-Polymer zurückgeführt. Schließlich wurde die Ansprechzeit meines Sensors verbessert, wenn die Luminophore in nassgesponnene PVA-Hydrogel-Fasern eingebettet wurden, aufgrund des hohen Oberflächen-Volumen-Verhältnisses. Die metallfreien, rein organischen Sensoren, die eine kontinuierliche, wiederholte und schnelle Detektion von O_2 innerhalb eines physiologischen O_2-Sensorbereichs ermöglichen, sind insbesondere für die Überwachung von verpackten Lebensmitteln, Biomonitoring und Biosensorik-Anwendungen interessant.

Stichworte

Kohlenstoff-Nanopunkte, Raumtemperatur-Phosphoreszenz, optischer Sauerstoffsensor, Lumineszenz-Abschreckung, Polymermatrizen

Contents

List of Figures

List of Tables

To my beloved family

Chapter 1

Introduction

Note: This sub-chapter has been adapted from "CHAPTER 2:New Polymer-based Sensor Materials and Fabrication Technologies for Large-scale Applications" , E. Armagan, D.B Papkovsky, C. Toncelli, in *Quenched-phosphorescence Detection of Molecular Oxygen: Applications in Life Sciences,* 2018, pp. 19-49. E. Armagan conducted the literature review and took part in writing of this book chapter.

The continuous progress in the synthesis of new organic phosphorescent reporter dyes and nanostructures with sensitivity to molecular oxygen (O_2) has produced a growing toolbox of optical transducers with a variegated response to O_2, brightness, lifetime ranges, photostability, accessible functional groups, sensor material types/formats[1–4]. In liquid media, such long-decay emitting transducers can undergo quenching by triplet-triplet annihilation (once they are at close inter-molecular distances). Their photoluminescence is often affected by other quenchers or environmental parameters, thus preventing the generation of strong optical signals and predictable operation as O_2 sensors. On the other hand, encapsulation of O_2-sensitive phosphors in solid matrices helps to overcome these problems and facilitates sensor handling and reuse, thus providing a convenient solution for the translation of the basic O_2 quenching concept to commercial sensors[1,3–6]. Phosphor type and encapsulation process can be tailored to the required application, with variable sensor shape, fine structure, and size spanning the nano-, micro, and macroscale.

While nanosensors are usually engineered with a sophisticated surface chemistry to interact with a specific interface[3], the development of planar film sensors, sensor dots, optical fibers, or assay vessels compromises the generation of a homogenous sensor material and a cost-efficient fabrication and integration process [1,5,6]. However, trade-offs are usually required between sensor complexity and analytical performance, ease of fabrication, controllability and scaling up capabilities of the sensor fabrication procedure, integration of oxygen sensors in specific applications, and measurement setup, especially for large-scale packaging applications[1,5,6].

Such a need is particularly prominent to control the exposure of O_2-sensitive items and evaluate any packaging failures. Pharmaceutical, electronic, and food industries routinely produce consumer goods that must be protected and maintained in an inert atmosphere[6,7].

Modified atmosphere packaging (MAP) in food is often applied to reduce the O_2 content in packaging, typically below 0.5% [5]. However, fresh red meat is packaged under high O_2 levels (40-60%) to improve its color and appearance. Improper gas flushing, trapped air, poor sealing or permeation of O_2 via the packaging material, or accidental damage can alter O_2 levels and lead to fast product degradation[8]. Integrated O_2 sensors could help to identify packaging failure at any stage, in a non-destructive manner, and in each single packaged product. This application requires low-cost, calibration-free sensors working accurately and robustly on a disposable and continuous basis, and which allow easy integration in various types of packages and products throughout the whole supply chain.

The encapsulation medium regulates O_2 accessibility, enhances and preserves phosphor stability under different physical, mechanical, thermal, or light conditions, does not interfere with luminophore operation while shielding it from external interferences and stabilizing with covalent or non-covalent interactions from leaching, migration, or aggregation[1,4–6,9].

A customized solution, which includes sensor design, fabrication, and integration, is often needed to optimally match the key requirements and operational specifications of each particular application. For example, sensors for trace O_2 detection or near-anoxic conditions[10] use different luminophores and encapsulation media than those utilized in standard industrial process control and packaging[4–6] where a broader O_2 dynamic range is required. In addition, different temperature and humidity operational windows, as well as spatial homogeneity and spatial resolution, are needed. While mapping is not generally required for O_2 sensors in packaging[5–7], it is fundamental for the development of O_2 sensitive paints[1].

Sensors for large-scale applications require continuous, high volume production processes, minimal number of components and fabrication steps, use of environmentally friendly solvents, biocompatible and safe materials, and ingredients, low energy consumption during the entire sensor fabrication cycle, high reproducibility, and uniformity of individual sensors to enable calibration-free (or factory-calibrated) operation, high robustness and

flexibility[1,5,6]. Casting a physical mixture of luminophore and polymer solution (liquid precursor 'mixture') onto a substrate to produce thin-film solid-state sensor coatings can satisfy many of these requirements[1,4–6]. However, the performance of many such sensors, including those produced commercially, is often jeopardized by micro-heterogeneities, cross-sensitivity, drift or instability of calibration, difficulties in process control, and production of standardized and identical batches of sensors[6]. This obviously affects sensor robustness, reproducibility, accuracy, signal intensity, spatial homogeneity, and production costs.

More sophisticated material processing, such as solvent crazing[11,12], encapsulation in mesoporous membranes[13,14], electrospinning[15–18], and wet-spinning[19], despite requiring more complex equipment facilities, have the potential to improve the homogeneity of sensor micro-environment, enlarge the operational range and sensitivity of conventional O_2 sensors. Parallel to this, research in enhancing the matrix/phosphor compatibility by non-covalent interactions between the two components has produced sensibly lower phosphor leaching, formation of mixed polymer phases with support material, higher spatial and in-depth homogeneity of the resulting O_2 sensors[20].

1.1 Brief History of O_2 Sensing

1.1.1 Electrochemical Oxygen Sensor

In the last decades, continuous monitoring of oxygen (O_2) concentration gained a lot of interest in a wide variety of research areas, such as biomedical applications, food packaging industry, and aerospace industry[21,22]. One of the most extensively used O_2 sensors was invented by Leland Clark in 1962, the so-called "Clark Electrode" (Figure 1.1). This technique is based on an electrochemical reaction between anode and O_2 molecules reaching the cathode through an oxygen-permeable membrane. Subsequently, the oxygen is reduced at the cathode of the sensor and creates a measurable electric signal. The O_2 concentration is then measured by detecting the variation in electrical currents at different O_2 concentrations. The advantage of the Clark electrode is good sensitivity towards O_2 molecules, which can detect O_2 concentration value up to 0.5 ppm. That makes Clark electrode as the gold standard for oxygen sensing[23]. However, many drawbacks of Clark-type electrochemical oxygen sensor limit the use of this electrode: i) destructive technique (consumption of the analyte) ii) high cross-sensitivity of interfering molecules (chlorine, carbon dioxide, ozone, or nitric oxides) iii) low shelf-life (up to 6 months)[23]. Long-emitting optical probes, by

contrast, could provide a valuable alternative as O_2 sensors for the reversible and non-destructive measurement of O_2 concentration[24].
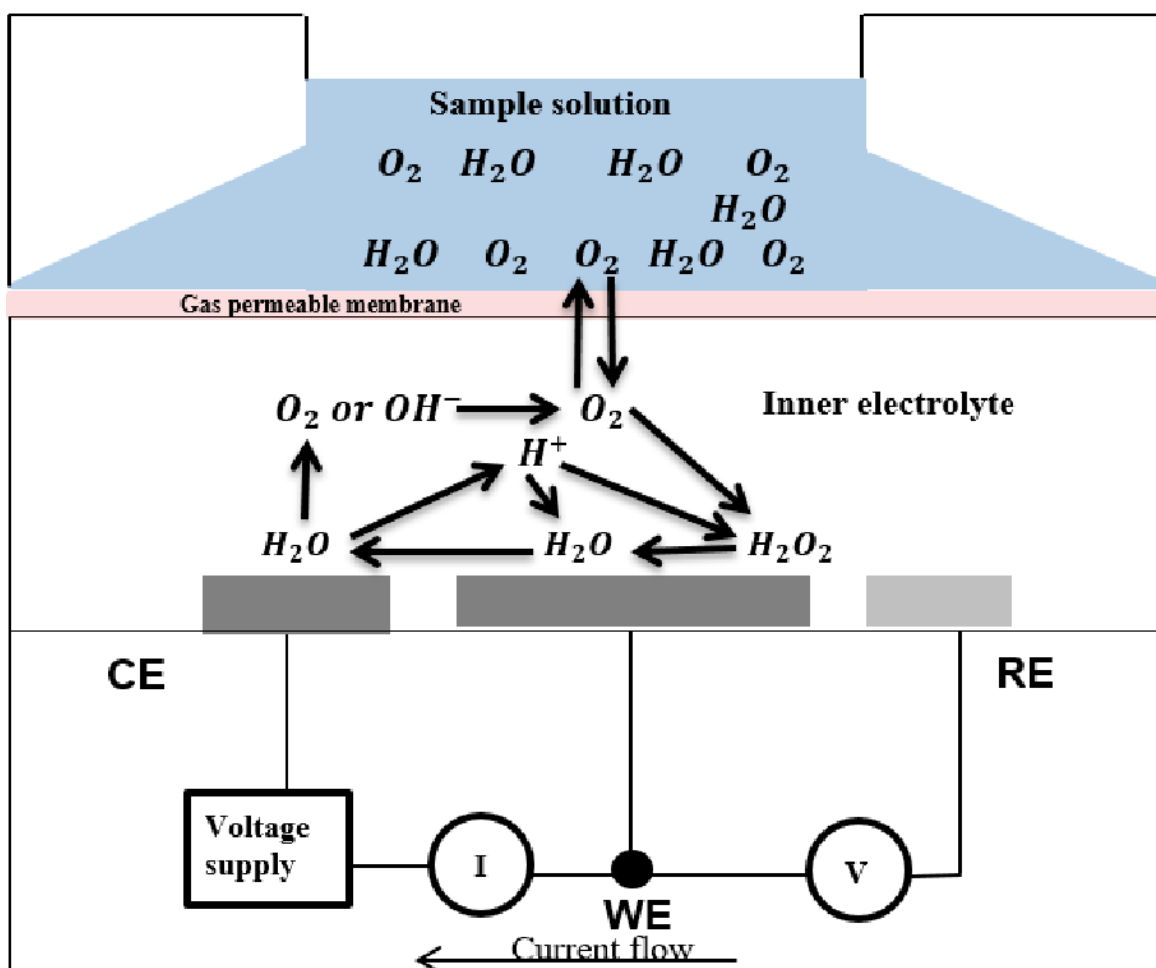
Figure. 1.1 Schematic Illustration of Clark-type electrochemical O_2 sensor[236].

1.1.2 Optical Oxygen Sensors

An optical oxygen sensor is a type of oxygen sensor which measures the oxygen concentration by the change of optical properties with respect to the analyte concentration. The working principle of the optical oxygen sensor is based on the change of luminescence intensity or lifetime at varying O_2 concentrations. There are two types of luminescence in nature: Fluorescence and Phosphorescence. Fluorescence is one of the luminescence phenomena, which is the emission of light by the radiative relaxation between a singlet excited state and a singlet ground state (Figure 1.2). The other type of luminescence is phosphorescence, where emission occurs by the radiative relaxation between the triplet excited state and the singlet ground state (Figure 1.2). However, the electron should change its spin be-

fore it jumps from the singlet excited state to the triplet excited state, known as an intersystem crossing. This process involves spin-forbidden transitions; therefore, there must be an efficient spin-orbit coupling (SOC) in the luminophore that makes intersystem crossing energetically more favorable. In the presence of quencher molecules (e.g., oxygen), the analyte starts to collide with luminophores, and subsequently, there is an energy transfer between the excited luminophore's triplet state and the excited singlet state of quenchers by dynamic collision[2] (Figure 1.2). This process is called "Luminescence quenching." The luminescence intensity is maximum under anoxic conditions.
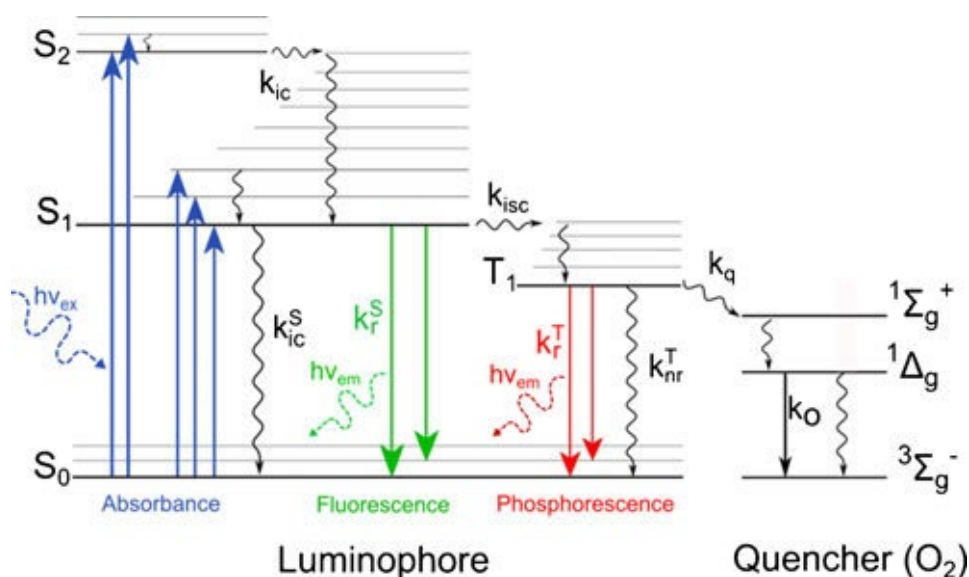
Figure. 1.2 Perrin-Jablonski Diagram which illustrates the fluorescence and phosphorescence emission, intersystem crossing between singlet excited state and triplet excited state, and quenching process in the presence of quencher molecules[25].

The luminescence signal mostly shows non-linear behavior with respect to oxygen concentration. These probes exhibit higher sensitivity at hypoxia conditions; vice versa, the sensor sensitivity decreases as the analyte concentration increases. This can be further explained by the Stern-Volmer relationship, which clarifies the photophysical kinetics of the quenching process between excited luminophore and analyte molecules. The energy transfer between two species can be represented by a reaction mechanism below;

$$A^* + Q \longrightarrow A + Q^*$$

where A is luminescent species, Q is quencher molecules, and * denotes an excited state.

The Stern-Volmer quenching constant, which determines the limit of detection of an optical sensor, was calculated in accordance with the Stern-Volmer Equation.

$$I_0/I = 1 + K_{sv} \cdot [O_2] \tag{1}$$

where I_0 and I represent the luminescence intensities in the absence and presence of O_2, respectively. K_{sv} is the Stern-Volmer quenching constant, and $[O_2]$ is the oxygen concentration in the environment. This equation can be fitted with respect to the intensity or lifetime values of the luminophores (Figure 1.3). The fitted curve can be used as the calibration curve of the optical oxygen sensor.
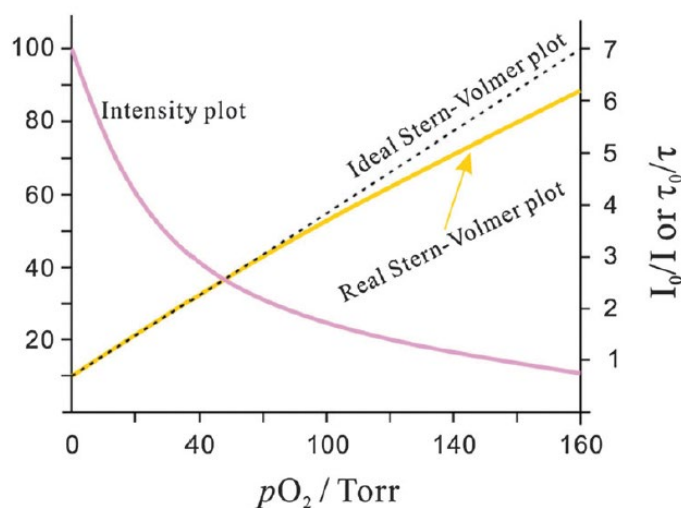
Figure. 1.3 Intensity curve of luminophores with respect to O_2 concentration and respective Stern-Volmer curves[25].

Generally, organometallic compounds containing heavy-metal ions are utilized as commercial probes for optical oxygen detection. The presence of the heavy metal ion allows an efficient spin-orbit coupling related to the energy transfer to the excited triplet states of the luminophore, thereby leading to long-lived emission features. Herein, the critical problem is the dispersion of these luminophores into a matrix without incurring any self-quenching processes[9]. In recent years, several processing technologies have been used to tackle this issue, such as printing of polymeric mixture in the organic solvent, adsorption, polymerization/curing, sol−gel method, nano and microprecipitation, solvent crazing, and coextrusion[25].

Unfortunately, these sensors are not viable for application in the life sciences as well as in food packaging due to: i) high sensor cost[9] (10-50 € per sensor), ii) high level of toxicity (dark-toxicity)[24] and iii) lack of photostability[25].

The presence of heavy-metal ions in the organometallic complex is the main reason for the problem, which leads to the commercial viability; on the other hand, the development of room temperature phosphorescent probes by solely utilizing organic emitters is a challenging task. Hence, in the last decades, many studies have been done to develop metal-ion-free long-emitting optical probes, such as phosphorescent carbon nanodots (PCNDs) and low-molecular organic emitters[26]. Organic compounds are used in both approaches that show low band gap and efficient energy transfer between the excited singlet state and the excited triplet state of these luminophores[26]. Therefore, many different organic moieties, such as aromatic carbonyls[27–34], aromatic amines[35–37], N-aromatic heterocycles (e.g., phenazine[38,39], carbazole[40–42], quinoline[43]), β-diketonate boron complexes[43], aromatic di-acids and di-esters[44], persulfurated benzene cores with tolyl substitutents[45], have been utilized as building blocks to synthesize organic phosphorescent oxygen sensors. On the other hand, these organic photoemitters must be embedded into a rigid matrix to eliminate the vibrational modes (rotational or translational vibration) by forming either covalent cross-linking[46] or non-covalent interactions[47,48] that enhance the degree of crystallinity and encapsulation within the rigid framework[49].

1.2 Purely Organic Luminophores

To have non-toxic, cost-effective, and photostable luminescence, purely organic luminophores have been widely studied since 2004 as a promising alternative to traditional luminescent nanostructures (i.e semiconductor quantum dots, metal nanoclusters, inorganic nanocomposites, and metal-doped nanomaterials) in various technical applications, such as bioimaging, food packaging, and drug delivery[50,51]. In recent years, a wide variety of bio and chemo-sensors have been designed by utilizing these luminophores as optical probes. Thanks to their low in-vitro[52] and in-vivo toxicity[53], these nanomaterials are particularly suitable in sensing for biomedical or food-related applications. In addition, they can be used as a promising alternative in bio- or chemo-sensors thanks to their superior photostability,

which prevents signal drift and provides a long shelf-life. Furthermore, cost-efficient precursors and synthesis make them a good candidate in the fabrication of various types of sensors.

Traditionally, common organic luminophores are described as a 3-D core-shell nanocomposite with a partly crystalline carbon frame surrounded by a wide variety of functional groups (e.g. amine, carboxyl, hydroxyl, or thiol) according to the carbogenic precursor. Interestingly, variation in the surface functional groups alters the nature of the surface defects, in turn related to the optical properties of the network. Thanks to their versatility in surface chemistry, these materials can also be utilized by cross-linking them via covalent or non-covalent interactions. Self-quenching phenomena induced by cross-linking are relatively low, whereas, in conventional planar aromatic dyes, π-π stackings and other non-covalent interactions strongly reduce their quantum yields.

1.2.1 *Synthesis of Luminescent Organic Materials*

In recent years, purely organic luminophores have been extensively studied as a promising alternative to luminescent nanostructures[50]. The synthesis method of organic luminophores is divided into two categories: i) Top-Down Approach and ii) Bottom-Up Approach. In the top-down approach, luminophores are obtained from big sp^2 carbon structures, such as graphene, graphite, carbon nanotubes, or fullerenes through different processes such as laser ablation, chemical ablation, or microwave irradiation[54,55]. However, the low quantum yield and harsh synthesis conditions make these luminophores impractical for various applications. For example, Sun et al. synthesized carbon nanodots (CNDs) using laser ablation of graphite with a quantum yield between 4%-10% [56]. In contrast, CNDs are synthesized by the carbonization of low-molecular-weight precursors through hydrothermal or solvothermal reactions[57,58].

Hydrothermal synthesis is one of the most facile methods for producing water-soluble organic luminophores. With this technique, the small precursors are undergoing condensation reactions in solution at high temperatures (150-200 °C) and high vapor pressures. Citric acid is one of the commonly used precursors for the synthesis of luminophores[59]. For example, Qu et al. hydrothermally synthesized CNDs using citric acid in the presence of NaOH, and the so-formed CNDs showed a quantum yield of 22%[60]. However, the carbonization of citric acid yields low quantum efficiencies, usually below 25%. Hence, numerous studies have been carried out to improve the brightness of organic luminophores. A good strategy

to enhance the luminescence of these materials is increasing the reaction temperature, which stabilizes larger clusters[61]. Nevertheless, carbonization at temperatures higher than 230 °C enables the synthesis of graphitic carbon structures at the expense of unsaturated clusters, decreasing the overall luminescence.

On the other hand, in recent years, it has been found that when N-passivating groups are being utilized as co-precursors during the organic luminophore synthesis, the resulting structures show higher quantum yields. Indeed, Zhou et al. improved the quantum efficiency of citric acid-based CNDs by adding triethanolamine precursors, which resulted in a quantum yield of 52%[62]. Recently, urea has also been suggested as a carbon source for this scope with the presence of pyrrolic nitrogen stemming from amide bond formations and dehydration reactions[63,64]. In addition, aromatic precursors alone, such as aromatic diamines, have displayed multi-color emission. For example, Yuan et al. synthesized multi-emissive CNDs (blue, green, and orange) by using various naphthalene derivatives as carbon sources[65]. Besides, phenylenediamines are among the most commonly used aromatic precursors to synthesize multi-emissive organic luminophores. It was shown that orange and red emissive luminophores could be prepared from heating p-phenylenediamine with formamide and phosphorus acid solution[66,67]. To investigate the importance of chemical isomerism on the optical properties of luminophores, Jiang et al. studied that CNDs prepared by different isomers of phenylenediamine (meta, ortho or para) have a different color of emission[68]. Recently, there was one study that combined urea and p-phenylenediamine to produce multi-emissive CNDs. In their study, they indicated that different optical properties are seen with respect to the degree of surface oxidation state. Indeed, by increasing it, the band gap of CNDs reduces, which results in a red shifting of the fluorescence emission spectra[69].

1.2.2 Organic Carbon Nanodots with Long-lived Emission

While low-molecular emitters generally display challenging synthetic routes and low chemical inertness, phosphorescent carbon dots have been used as promising candidates for the development of photostable[70] and bio-inert[71] optical probes. Many studies in the last few years have produced phosphorescent CNDs by utilizing moieties that display an efficient SOC and having rigid structures for the suppression of vibrational modes. For the requirement of having an efficient SOC, the precursors which contain aromatic carbonyls[72] or nitrogen-rich amine/diamine moieties[73] have been utilized as an alternative to heavy metal ions.

For example, Li et al.[47] synthesized phosphorescent CNDs using a nitrogen-rich precursor which reacts with urea/biuret moieties to form the PCNDs matrix. Furthermore, Jiang et al.[73] reported that CNDs synthesized from diamines (m-phenylenediamine) showed a triple mode emission (photoluminescence, up-conversion photoluminescence, and phosphorescence) after being inserted into a poly vinylalcohol matrix (Figure 1.4)
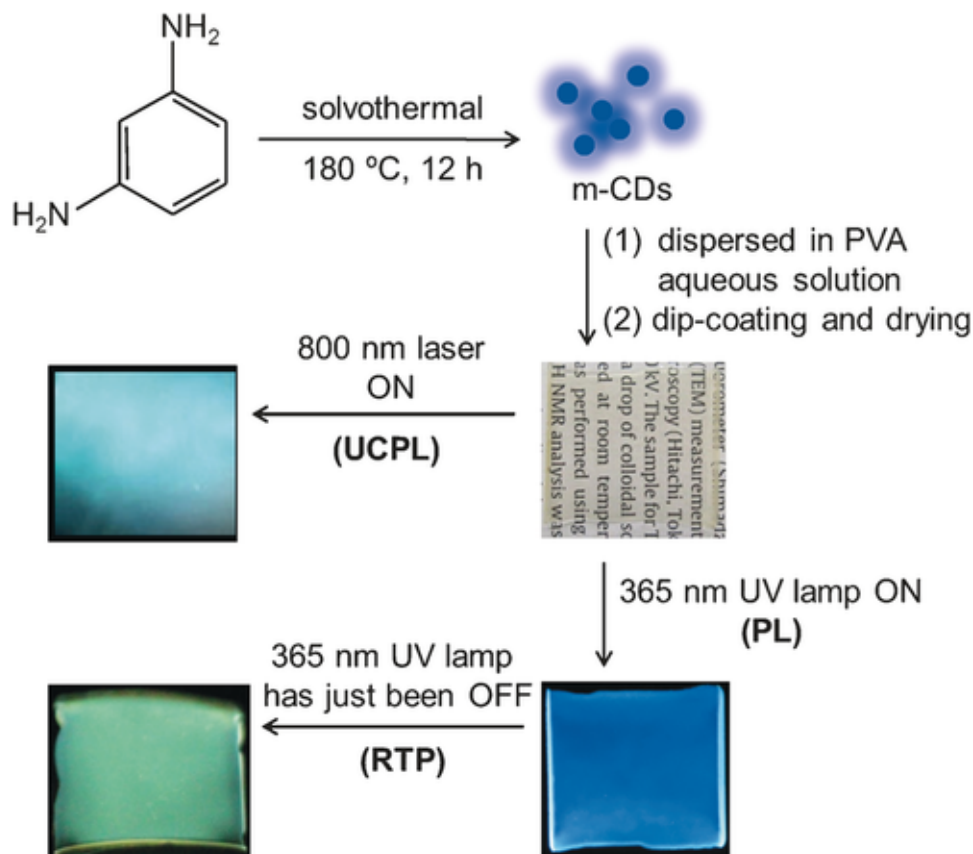
Figure. 1.4 Intensity curve of luminophores with respect to the O_2 concentration, and the respective Stern-Volmer curves[73].

To avoid non-radiative pathways, CNDs are generally embedded into a rigid inorganic or organic matrix (for more detailed information see chapter 1.3). As an example of an inorganic matrix, Wang et al.[74] synthesized phosphorescent CNDs and encapsulated the as-prepared CNDs within mesoporous silica microspheres. As such, they fabricated an intensity-based optical oxygen sensor which unfortunately responds only to low O_2 concentrations. It was also shown that phosphorescent CNDs could be obtained by dispersing CNDs into potash alum matrix, which lead to phosphorescent CNDs with a millisecond phosphorescence lifetime[49]. On the other hand, the organic matrix, such as urea/biuret[47], polyurethane[46] and poly vinyl alcohol matrix[74,75], have been used to embed CNDs with similar results in the phosphorescence lifetime (millisecond-second).

However, for most applications, it is actually needed to monitor oxygen concentrations up to 21% O_2. As the extent of oxygen quenching is related to the luminescence lifetime (longer lifetime translates in a higher number of collisions with oxygen molecules), it would be very appealing to reduce the lifetime to values similar to the commercial optical oxygen sensors (i.e.~μs)

1.3 Physical Entrapment of Luminophores within Organic Matrices

Note: This sub-chapter has been adapted from "CHAPTER 2:New Polymer-based Sensor Materials and Fabrication Technologies for Large-scale Applications" , E. Armagan, D.B Papkovsky, C. Toncelli, in *Quenched-phosphorescence Detection of Molecular Oxygen: Applications in Life Sciences,* 2018, pp. 19-49. E. Armagan conducted the literature review and took part in writing of this book chapter.

The concept of physical entrapment of luminophores within a matrix is generally simpler and more cost-efficient than systems involving a covalent or coordinative bridging between the luminophore and the matrix[1,2,76–78].

Traditionally, sensor coatings were fabricated by casting a liquid mixture containing a hydrophobic luminophore, hydrophobic polymer, or its organo-silica precursor in a non-polar organic solvent onto a suitable substrate, such as the surface of the glass slide, a tip of optical fiber or a polyester film[2]. After solvent evaporation, the luminophore becomes efficiently entrapped within the polymer, which forms a thin O_2 -permeable film on the corresponding substrate. Recently, the addition of water-soluble components within the sensor formulation has enabled the simultaneous formation of mesoporous O_2 sensing coatings[79].

A modification of this approach is when a luminophore dissolved in organic solvent (i.e., without matrix polymer) is applied directly on a micro-structured solid polymeric matrix (e.g., mesoporous microparticles[80] or membranes[81]) and let the luminophore molecules diffuse into its depth. The process, which can be facilitated by solvent optimization to enhance polymer swelling and/or by high temperature accelerating luminophore diffusion, should be designed such that it does not alter the final mechanical integrity and properties of the matrix (solvent compatibility) and provides uniform dyeing of the matrix. Such microporous[82], microfibrous[18], and microparticle[83] materials acting as both sensor substrate and encapsulation matrix, on the one hand help to match the mechanical properties of the coating with the

substrate, therefore providing higher adhesion at the interface, whereas on the other hand provide homogeneous micro-environment and/or dispersibility (powder form) of the luminophore emitter.

Indeed, often the mechanical and adhesion properties of the preferred type of sensor coating do not match the ones required by the application, as well as O_2 permeability, sensitivity, etc. Then it is necessary to add an intermediate step where the sensor material is produced in a micro-encapsulated form (e.g., phosphorescent microparticle powder) and then dispersed in a carrier media such as silicone rubber[84]. The latter provides the sensor coating with good O_2 permeability, mechanical and chemical stability, adhesion to the support material.

High-density networks of nanocavities can also be formed *in-situ* by stretching a semi-crystalline polymer film or fiber in a physically active liquid environment (PALE), the so-called solvent crazing[85]. By dispersing the luminophore in the PALE, efficient encapsulation of the luminophore and staining of the host polymer can be achieved by simple means, driven by diffusive processes.

The luminophore can also be entrapped in a matrix via layer-by-layer assembly of oppositely charged polymeric layers doped by luminophore molecules (LbL method)[86]. Furthermore, sensors with high O_2 accessibility, high sensitivity, and fast response were produced by electrically-induced adhesion to charged substrates via electrophoretic deposition[87] and electrospinning of fibers [88] under the applied external electric field.

A number of O_2-sensitive nanostructures were recently described[89]. Their integration in the sensor material usually proceeds by one of the above methods; however, since often these sensors do not exhibit phosphorescence before matrix integration, the reactivity of the functional moieties while anchoring them to the matrix and luminophore's surface chemistry should be taken into account. Spatial resolution in sensor fabrication and patterning of individual sensors (e.g., via photolithography processes) is a crucial requirement for their integration in microfluidic devices[90–92].

1.3.1 Casting of Polymer Mixture

The casting of polymer/luminophore mixture represents a proper fabrication method, and it is still the most widely used route to produce large quantities of sensor films and

coatings on planar supports or partly on optical fibers[93–96]. The latter is utilized when there is a need to detect O_2 in cumbersome regions or where the use of conventional planar sensors is precluded [97]. Coating of curved surfaces is more complex than the planar counterparts; therefore, it requires tighter control of the mechanical properties of the matrix (i.e., adhesion, flexibility, to name a few). Different casting techniques are employed in the fabrication of conventional O_2 sensors, including drop coating, knife casting, dip coating, and spin coating. Drop coating involves the deposition of mixture aliquots on clean substrate surfaces with subsequent spreading and passive drying by solvent evaporation. The sensor quality and thickness, in this case, will be mainly determined by the mixture viscosity, polymer concentration, solvent polarity, the support surface chemistry, the volume of mixture applied and environmental parameters (temperature, humidity, convection, etc.).

O_2 sensors in packaging applications have some add-on requirements, such as the production of discrete, small-size sensors in specific locations of the substrate (to reduce sensor price and facilitate its visualization and access for the measurement), correct integration within packaging multi-layer laminates, without any negative impact on sensor performance [98]. This imposes stricter guidelines on sensor materials and manufacturing processes and significant restrictions on price (cent per sensor range). As a result, many polymeric materials have been utilized as matrices for O_2-sensitive luminophore, the most common being polystyrene, ethyl cellulose, polysulfone, and fluorinated polymers (Figure 1.5).
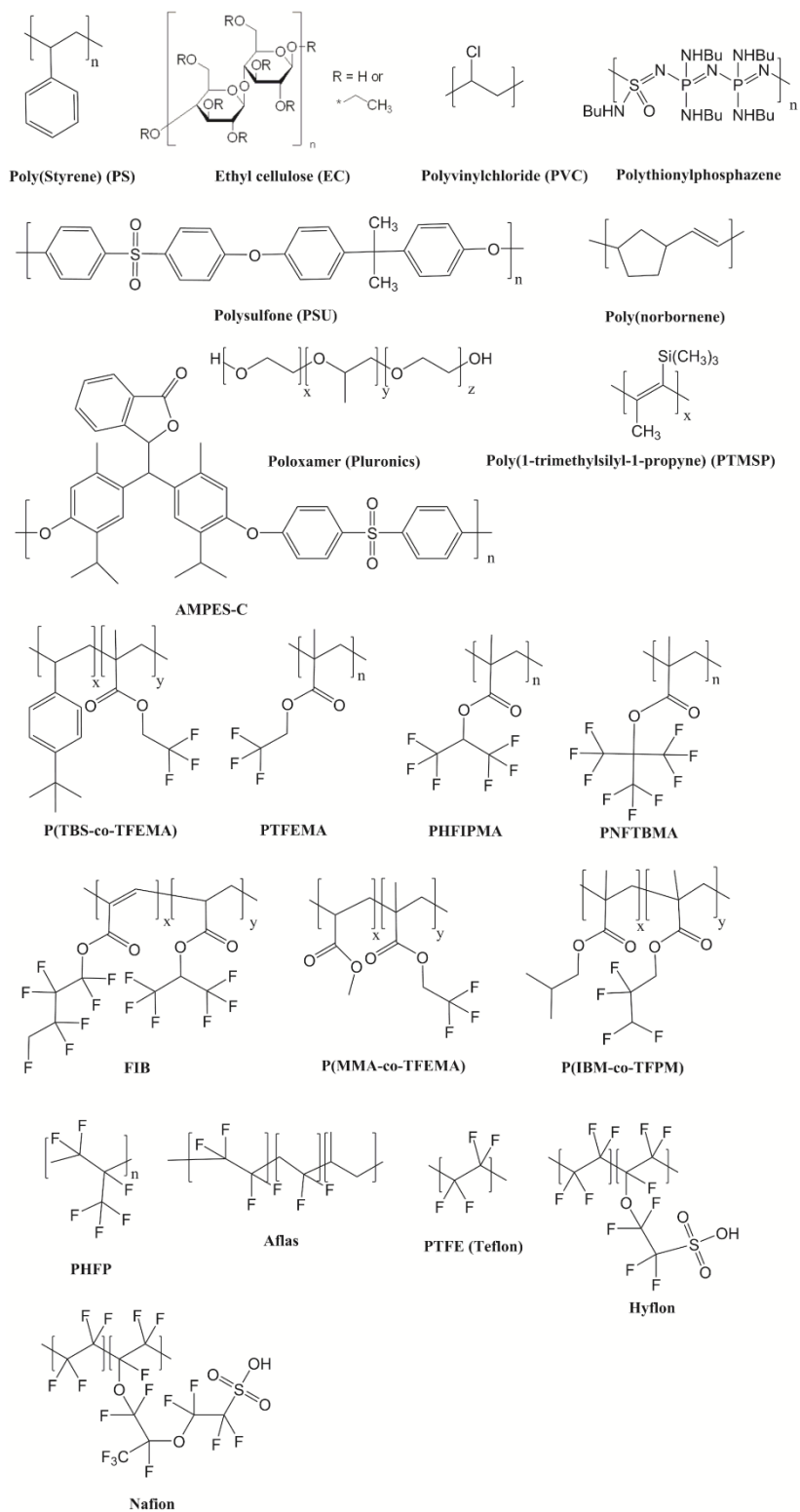
Figure. 1.5 Chemical structures of common polymer matrices utilized for luminophore encapsulation[158]

Researchers often use this matrix to test new luminophores [99–106], as polystyrene is soluble in a wide range of organic solvents (i.e. tetrahydrofuran [103,107,108], toluene [100,109], chloroform [99,101,102,104–106,110,111], butyl acetate [112]). Polystyrene can be utilized with mixtures

of different emitters or coupled with organic photodetectors [109], systems operating in ratiometric mode [110], additives (singlet oxygen scavengers) which reduce signal drift [107], or integrated into a multi-sensing device [112]. Sensor sensitivity can be tuned by changing the substituent in the para position of the phenyl ring or introducing fluorine atoms in both *o*-positions [113]. Thus, polystyrene modified with *t*-butyl groups showed approximately 4-fold higher sensitivity than unsubstituted polystyrene. The presence of fluorine atoms significantly increased sensor photostability, which is already high for fluorinated luminophores [114]. Due to the easiness of functionalization of phenyl halogens on the polymer skeleton, referenced dyes can be coupled to the backbone to obtain Förster resonance energy transfer pairs between the embedded temperature-sensitive and oxygen-sensitive phosphors, respectively [115].

Ethyl cellulose (EC) is another promising material with high optical transparency, solubility in many organic solvents, and O_2 permeability similar to polystyrene [116–122]. However, this hydrophilic polymer shows strong cross-sensitivity to humidity, with O_2 sensitivity reduced by 50 % at 85 % relative humidity (RH) compared to 0 % RH. Indeed, EC varies its O_2 permeability upon the entrapment of water molecules within the matrix [123]. Also, cross-sensitivity to temperature is more pronounced than Ormosils-based coatings[58].

Polysulfones (PSU) are also a promising alternative to PS and EC as this polymer matrix shows high optical clarity (though only when the membranes are not produced in the air) [124], chemical stability, moderate O_2 permeability, and low cross-sensitivity to humidity [125]. It has been shown [124,126–128] that polysulfone membranes can be utilized to determine the thermodynamic parameters of the oxygen quenching process and model sensor calibration. Polysulfone-based coatings with high mechanical and thermal stability can withstand sterilization by autoclaving [129], without changing their O_2 sensing properties.

Plasticized poly(vinyl chloride) membranes were employed to develop a dual analyte dissolved O_2/pH sensor based on one phosphorescent porphyrin luminophores with multi-receptor functionalities. In this case, the proton permeability of the membrane was enhanced by adding a borate salt within the formulation [130]. However, plasticizers and other additives make the sensor structure more complex and difficult to reproduce and stabilize (batch to batch variability and signal drifting by leaching of low-molecular-weight compounds).

Other polymers, namely poly(norbornene) [131], poly(thionylphosphazene) [132], cellulose acetate butyrate [133], AMPES-C [134], and poly(1-trimethylsily-1-propyne) [135,136], offer a possibility to change O_2 permeability and allow O_2 sensing in different dynamic ranges. In particular, poly(1-trimethylsilyl-1-propyne) (PTMSP) have shown ten-fold higher O_2 permeability than conventional gas permeable poly(dimethyl siloxane) (PDMS) films [135]. Non-functionalized poly(norbornene) has similar O_2 permeability to PS, which can be tuned by varying the steric hindrance of the side groups [131].

Fluorinated methacrylates [76,137–141] and other fluoropolymers such as poly(hexafluoropropylene) [78], poly(tetrafluoroethylene) (PTFE) [142], Aflas [79,80], Hyflon [81,142] and Nafion [80] have remarkably enhanced the sensitivity to O_2 for a given luminophore and led to solid sensors with better photostability. Indeed, they display extremely high O_2 permeability, thanks to the limited inter-molecular interactions due to shorter C-F bond lengths compared to C-H ones. Increasing the content of fluorinated methylene side groups of polymethacrylates further enhances their sensitivity to O_2 and reduces cross-sensitivity to temperature [140]. Since fluoropolymers show high chemical inertness, they are particularly useful for the detection of O_2 in chemically aggressive environments [79]. For example, combining an aluminum chelate with a PTFE matrix has recently achieved the highest sensitivity to O_2 with a limit of detection of 5 ppb in the gas phase or 7 pM in solution [142].

As a general remark, even though the casting of a physical mixture of polymer and luminophore permits an easy upscaling, simple and cost-efficient processing, and a variegated response to O_2, accuracy, robustness, and reproducibility of the resulting sensors are quite average, and it is not easy to generate factory-calibrated sensors by this technique. Indeed, variations in sensor morphology and micro-environment, interactions between the sensor and support materials (mixed polymer phases), significant volume contraction and associated mechanical stress upon drying of the polymeric mixture, non-uniformity of coatings, and other factors lead to pronounced heterogeneity, complex sensor behavior (non-linear Stern-Volmer plots and O_2 calibration), variable read-out of O_2 concentration, and possible delamination.

1.3.2 Spinning for fiber optic oxygen sensors

Conventional fiber spinning is a fabrication technique where polymer fibers can be produced with the diameters down to nanometer range via wet-spinning, dry-spinning, melt

spinning or gel spinning. In recent years, conventional fiber spinning techniques have been utilized for the physical entrapment of O_2-sensitive luminophores within polymer matrices. Nano- and micro- O_2-sensitive fibers produced by this technique display high O_2 sensitivity and short response time due to their large surface area-to-volume ratio and nanoporous scaffold architecture [143].

O_2 sensors were first produced by using the electrospinning technique, where an electric field between the sample dispenser and collector was used to draw charged threads of a polymer solution. In one of the pioneer studies, a mixture of polystyrene and a Eu(III) complex as feeding electrospinning solution were used to fabricate fiber-based optical O_2 sensor[144]. High sensitivity (I_0/I_{100} = 15.56), good linear Stern–Volmer characteristics, and short response/recovery time (t↓ of 7 s and t↑ (s) of 14 s) were obtained. Sensible improvement of the response time and sensitivity to $O_{2\ was}$ later confirmed for Cu(I) [145], Ir(III) [16,146], or Eu(III) [144,147,148] complexes. Comparison with conventional casted films of polystyrene/fluorinated Pd(II)-porphyrins revealed that the response time was decreased by two orders of magnitude (from several seconds to less than 40 ms) while sensor sensitivity and signal intensity were unaltered [149]. Two complexes of Re(I) were integrated into poly(vinylpyrrolidone) electrospun fibers, albeit due to the water solubility of the polymer, the sensors were strongly affected by humidity [150,151]. Additives, such as plasticizers, water-miscible and immiscible ionic liquids, and perfluorinated compounds, which enhance O_2 solubility in the matrix, allowed the electrospinning of ethyl cellulose and poly(methylmethacrylate) formulations [152]. The resulting sensors showed high stability over three years, probably due to stabilizing the ruthenium oxidation state by the perfluorinated compound. Encapsulation of a referencing dye for ratiometric intensity sensing mode is also compatible with the electrospinning technique [153].

Co-axial electrospinning was performed to obtain a fiber with a poly(dimethyl siloxane) (PDMS) core in which the luminophore was encapsulated and a poly(caprolactone) (PCL) shell, which preserved the mechanical integrity of PDMS during the curing process and also enhanced biocompatibility of the fiber [154]. Core-shell fibers can also be used to encapsulate different layers of up-converting nanoparticles and O_2-sensitive dye in an electro-optical handshake fashion. The use of up-converting nanoparticles minimizes light absorption and scattering effects of biological tissues on the sensor [155]. It is essential to mention that even such high nanostructure complexity can be achieved in a one-step process

by utilizing different electrospinning setups and feeding devices. Nanoporous poly(caprolactone) fibers were impregnated by soaking them in a solution of an O_2-sensitive dye to generate a phosphorescent scaffold suitable for cell growth, contactless monitoring, and live imaging of O_2 [18].

Microfluidic wet-spinning is a wet-spinning process that confines the polymer and coagulant solutions within co-axial laminar flows. This process enables good control of the diffusion interface between two laminar flows, resulting in the solidification of polymer solution in a controlled manner[254]. In addition, microfluidic wet-spinning offers an advantage of a mild spinning environment, compared to the electrospinning technique, which enables the spinning of natural polymer without using any harsh solvents[255]. Various hydrogel fibers, such as alginate, collagen, and chitosan, can be fabricated using microfluidic spinning, resulting from the co-axial laminar flow of core (pre-polymer solution) and sheath fluids (crosslinking agents)[256–259]. Microfluidic wet-spinning offers several morphological advantages, such as high porosity and large pore size, which play a critical role in O_2 diffusion through the polymer matrix[260,261].

Chapter 2
Scope of the Thesis

2.1 Motivation

Oxygen sensing has been a topic of intensive study in many fields, such as food monitoring, cell biology, biomedicine, and environmental monitoring. Particularly, optical O_2 sensors have attracted significant attention from many biological, medical, and packaged food-related applications, where the detection of O_2 changes in a continuous, reversible, non-toxic, and non-destructive manner is in high demand. Organic sensing units have been recently integrated into polymer matrices to have purely organic optical O2 sensors to meet these demands. However, the main limitations of this type of sensor are limited sensing range and unsatisfactory reversibility. In this regard, a few studies have focused on improving the sensing range of organic optical O_2 sensors by synthesizing different organic sensing units. Nevertheless, they could only sense the whole physiological O_2 range (0-21% O_2) with unsatisfactory sensor reversibility.

Synthesizing new diamine-based luminophores with rigid crosslinking chemistry might enhance spin-orbit coupling efficiency and inhibit unwanted non-radiative recombination, leading to efficient room-temperature phosphorescence (RTP). I expect that the efficient RTP mechanism facilitates the energy transfer between my sensing units and oxygen molecules. Understanding the effect of using highly rigid luminophores on the extent of oxygen quenching will help to elucidate the importance of having rigid crosslinkers in these systems.

The type of polymer matrix, where luminophores were integrated, plays an essential role in the O_2 sensing performance. Although many polymer-based optical oxygen sensors have been published in the literature, there have been a few studies on the O_2 sensing performance of the organic luminophores embedded into the hydrogel network. Investigation of the effect of using hydrogel matrix on O_2 sensing performance may open a new pathway for the intelligent food packaging system. Integrated hydrogel optical oxygen sensor could help identify packaging failure at especially high humidity levels where many polymer matrices' structural integrity is significantly affected. Furthermore, the shape of a polymer matrix is critical for oxygen diffusion kinetics due to the change in the surface-to-volume

ratio. Elucidating the effect of surface-to-volume ratio on O_2 diffusion rate may help to fabricate a high-speed O_2 sensor that broadens the application field of purely organic optical O_2 sensors.

2.2 Objective

The thesis aims at fabricating a purely organic optical O_2 sensor with broad-range and reversible oxygen sensing. For this purpose, approaches will be developed to synthesize new diamine-based sensing units with rigid crosslinking chemistry and embed these luminophores into polymer matrices. With these methods in place, the influence of rigidity on the O_2 sensing performance will be investigated. Furthermore, the O_2 sensitivity of synthesized luminophores embedded into conventional polymer and hydrogel will be compared to understand the effect of the type of polymer matrices. Finally, the correlation between the surface-to-volume ratio and O_2 sensing performance will be analyzed by fabricating hydrogel fibers with different diameters. This work will provide a better understanding of the effect of luminophore rigidity on the O_2 quenching mechanism and the importance of the selection of polymer matrices and the shape of sensors on O_2 sensing performance.

Chapter 3: Synthesizing a new diamine-based luminophores from urea and p-phenylenediamine via hydrothermal synthesis technique to have purely organic optical O_2 sensing.

The synthesis parameters of the new luminophore system will be established to optimize the optical properties. Subsequently, the origin of luminescence and ensemble of hydrothermal products will be investigated using mass distribution analysis. The chemical analysis will be performed on luminophores to understand the evolution of nanostructures. The optical properties will be investigated to have a correlation between the kinetic of hydrothermal synthesis and emission behavior. Finally, the O_2 sensing performance of each luminophore will be investigated in terms of O_2 sensitivity, reversibility, and response time. These investigations will give insights into the effect of using urea-based crosslinker between diamine units on O_2 sensing performance.

Chapter 4: Investigating the effect of using rigid polyimide linkers between diamine-based sensing units on the improvement of O_2 sensitivity.

This chapter aims at synthesizing a rigid sensing unit utilizing polyimide chemistry to enable the efficient RTP mechanism. Therefore, the imidization process will be investigated using chemical characterization. Chemical analysis will be combined with optical characterization to understand the effect of the polyimide network on emission behavior. The O_2 sensor test will be performed on optimized polyimide-based nanoparticles to elucidate the impact of structural rigidity on the O_2 sensitivity range. Finally, the best performing nanoparticles will be selected for further O_2 sensing performance tests. These investigations will highlight the importance of using a highly rigid network to fabricate organic optical O2 sensors for further studies.

Chapter 5: Investigating the effect of polymer matrix selection and sensor shape on O_2 sensing performance.

This chapter aims to fabricate hydrogel-based organic optical O_2 sensors to investigate the effect of polymer matrix selection on the O_2 sensitivity range. Furthermore, the microfluidic wet-spun hydrogel fiber containing polyimide-based luminophores will be produced with different diameters to understand the correlation between surface-to-volume ratio and sensor response rate. These investigations will help to fabricate a new hydrogel-based O_2 sensors with a broad-range and fast O_2 sensing.

Chapter 6: Conclusion and outlook

The conclusion will comprise a short summary of my findings and the outcome of the thesis. The future research strategies for purely organic optical O_2 sensors will also be discussed in this chapter.

Chapter 3
Reversible oxygen sensing based on multi-emission fluorescence quenching

Note: This chapter has been published in "Reversible oxygen sensing based on multi-emission fluorescence quenching", E. Armagan, S. Thiyagarajan, K. Wei, A. Gursoy, G. Fortunato, E. Amstad, R.M. Rossi, C. Toncelli, Sensors 20, 477 (2020). E. Armagan performed the fluorophores synthesis and its chemical, optical and sensor characterization by ESI-QTOF, Maldi-TOF, LC-MS, Fluorescence spectraphotometer, lifetime analysis, UV-Vis, AFM as well as sensor performance test. E. Armagan also analysed all the data and wrote the manuscript with the input from all authors.

3.1 Abstract

Oxygen is ubiquitous in nature, and it plays a key role in several biological processes, such as cellular respiration and food deterioration, to name a few. Currently, reversible and non-destructive oxygen sensing is usually performed with sensors produced by photosensitization of phosphorescent organometallic complexes. In this chapter, I propose a novel route of optical oxygen sensing by fluorescence-based quenching of oxygen. This system involves a set of multi-emissive purely organic emitters. These were produced through a one-pot hydrothermal synthesis using p-phenylenediamine (PPD) and urea as starting materials. The origin of the multi-emission has been ascribed to the diversity of chemical structures produced as a result of oxidative oligomerization of PPD. A Bandrowski's base (BB) (i.e., trimer of PPD) is reported as the main component at reaction times higher than 8 hrs. This indication was confirmed by electrospray-ionization quadrupole time-of-flight (ESI-QTOF) and liquid chromatography-mass spectrometry (LC-MS) analysis. Once the emitters are embedded within a high molecular weight poly(vinyl alcohol) matrix, the intensities of all three emission centers exhibit a non-linear quenching provoked by oxygen within the range of 0-8 % O_2. The detection limit of the emission centers are 0.89 %, 0.67 % and 0.75 % O_2, respectively. This oxygen-dependent change in fluorescence emission is reproducible with negligible cross-interference to humidity; however, it has unsatisfactory reversibility (up to three tested 0-21 % O_2 cycles). The cost-effectiveness, metal-free formulation, cross-referencing between each single emission center, and the relevant oxygen range are all appealing features, making these sensors promising for the detection of oxygen, e.g., in packaged food products.

3.2 Introduction

Oxygen participates in several biological processes, including food spoilage or in the plant, animal, and human metabolism[156,157]. It is, therefore, crucial to develop a simple sensing method to detect local changes in oxygen concentration in a reversible and non-destructive fashion (e.g., without consuming the analyte during the measurement).

In this respect, optical sensing is the most appealing system for oxygen monitoring since it can be reversible and miniaturized for detecting local concentration shifts. Photoemitters exhibiting oxygen sensitivity mostly undergo quenching of long-lived emissive states, such as phosphorescence and delayed fluorescence, provoked by energy transfer with oxygen[158]. These emission modes can only be triggered by a strong spin-orbit coupling (SOC) to enable the otherwise quantum-mechanically forbidden transition from the excited singlet to the excited triplet state[159]. As for now, specific organic ligands coordinated to heavy metal ions, such as Pd(II), Pt(II), or Ru(II), represent the exclusive commercial solution to trigger oxygen sensitivity[160-163]. On the other hand, several applications, such as food quality assessment, require the use of disposable oxygen sensors that have to be mass-produced with alternatives that are more cost-effective.

The development of metal-free oxygen sensors with relevant detection windows for monitoring oxygen in a physiological oxygen range is still an unmet challenge. Purely organic emitters can display room-temperature phosphorescence (RTP) when directly connecting heteroatoms to aromatic moieties (bromo-aldehydes[164], di-ketones[165,166], di-acids and di-esters [167]) and at the same time inhibiting their internal molecular motions. This can be induced, for example, by crystallization-enhanced RTP [166,167], aggregation-induced intersystem crossing [168], encapsulation within rigid cages [169], or the rigidification of the emission centers by non-covalent[164] and covalent [170] interactions with a matrix. However, the complexity of the synthetic pathways to achieve the desired oxygen sensitivity precludes the viability of these emitters in terms of commercial exploitation.

An interesting twist of this strategy is offered by embedding bottom-up assembled carbon nanostructures (e.g., carbon nanodots, CND) in hydrogen bonding matrices, such as poly(vinyl alcohol) (PVA) [171,172], polyurethane [173], and potash alum [174], by establishing covalent cross-linking with the matrix [175,176] or by encapsulating the optical probes within rigid mesoporous cages [177,178]. In particular, red-emissive RTP CNDs can be obtained by hydrothermal synthesis of aromatic di-amines [179,180] and encapsulation within a poly(vinyl alcohol) (PVA) matrix [181]. However, their phosphorescence is rather long, in the order of several

milliseconds, which translates into highly sensitive oxygen sensors, only applicable for extremely hypoxic environments.

Alternatively, fluorescence-based quenching using aromatic amines, such as β-carbolines [182] and acridines [183] has been demonstrated as a promising strategy for oxygen sensing. This peculiar sensing mechanism is related to the formation of charge-transfer complexes between the contact radical ion pair state $^3(^2M^{\bullet+},2O^{2\bullet-})$ when mixed with the locally excited (LE) states [184]. However, fluorescence-based quenching is still not well understood and remains unexplored in the literature.

Hereby, it has been demonstrated that an ensemble of hydrothermal products from urea and p-phenylenediamine gives rise to multi-emissive oxygen sensors once integrated into a poly(vinyl alcohol) (PVA) matrix. Moreover, these sensors can achieve oxygen sensing in a reversible manner, quenching the fluorescence intensity in the range of 0-8 % O_2.

Despite the complexity of the reaction pathways during the hydrothermal synthesis, it has been identified by electrospray ionization coupled with quadrupole time of flight (ESI-QTOF) and liquid chromatography coupled with mass spectrometry (LC-MS) Bandrowski's base as the main component at 16 hrs reaction times. This chapter represents the first example of a multi-emissive oxygen probe with a fluorescence-based oxygen-quenching mechanism. This work has the potential to set an industrially-viable approach for the development of purely organic fluorescence-based reversible oxygen sensors.

3.3 Experimental Section

3.3.1 Materials

P-phenylenediamine (PPD) (Sigma-Aldrich, ≥99%) and urea (Sigma-Aldrich, ≥99%) were used as received. Potassium Bromide (KBr) of analytical grade (≥99%) was purchased from Merck for the FT-IR studies. HPLC graded acetonitrile (ACN) (Sigma-Aldrich, ≥99.9 %) and ultra-pure water (milli-Q) have been used as eluent for both LC-MS and flash chromatography. Mowiol 40-88 (Mw ~205000 Da) was purchased from Sigma-Aldrich for the embedment of the optical sensor. Oxygen (99.99 % purity, H_2O< 2 ppm) and nitrogen (99.8 %, H_2O< 40 ppm) tanks were purchased from Carbagas.

3.3.2 Synthesis of the Fluorophores

100 mg of PPD and 100 mg of urea were placed in a round-bottom flask in the presence of 25 mL of water. Subsequently, the solution was vigorously mixed by sonicating for 30 min

at RT, either in air or nitrogen atmosphere. Afterward, the solution was transferred to a pol-ytetrafluoroethylene (PTFE) lined synthesis autoclave reactor (Parr Instrument, Acid Diges-tion Vessel) with a volume of 50 mL. For the de-oxygenated conditions, the solution was degassed by bubbling nitrogen under sonication, and the Teflon chamber was flushed with nitrogen before transferring the solution. The PTFE lined autoclave reactor was then placed in an oven and maintained at 160 °C for different reaction times (Table 3.1). The products were then freeze-dried for 24 hours. Accordingly, the products are named as U-PPDx, Uy, PPDz, D-Um, D-PPDn, and D-U-PPDo, respectively, where x, y, z, m, n, and o represent the reaction time, U-PPD represents the used reactants for the synthesis (U: urea and PPD: p-phenylenediamine. To synthesize U16 and PPD16, I have utilized the same procedure but with a concentration of the single precursor equal to 8 mg /mL.

Sample Name	Reaction Atmosphere	Reaction Time (hrs)	Precursors	Final/Initial Mass (%)
U-PPD2	Air	2	Urea-PPD	71.2
U-PPD4	Air	4	Urea-PPD	56.6
U-PPD6	Air	6	Urea-PPD	53.8
U-PPD8	Air	8	Urea-PPD	56.8
U-PPD16	Air	16	Urea-PPD	57.5
U16	Air	16	Urea	32.7
PPD16	Air	16	PPD	51.8
D-U16	Nitrogen	16	Urea	N.D.[a]
D-PPD16	Nitrogen	16	PPD	N.D.[a]
D-U-PPD16	Nitrogen	16	Urea-PPD	N.D.[a]

Table 3.1. Hydrothermal reaction condition for producing urea and PPD derived fluorophores. 100 mg urea and 100 mg PPD in 25 mL water were placed in an autoclave reactor. The reaction time was kept between 2 hrs and 16 hrs. The final mass was divided by the initial total mass of precursors to calculate the percentage of obtained mass. [a] Not determined

3.3.3 Characterization of the Fluorophores

Molecular weight analysis of U-PPD16 and its isolated compounds were performed with ESI-QTOF, MALDI-TOF, and LC-MS. A mid-mass positive method ESI-QTOF was combined with mass spectroscopy for U-PPD2, U-PPD4, U-PPD6, U-PPD8, and U-PPD16 samples within the range from 100 m/z to 1000 m/z. For MALDI-TOF experiments, MALDI-

TOF UltraFlex LP 5-20 kDa using a 10/1 trans-2-[3-(4-tert-Butylphenyl)-2-methyl-2-pro-penylidene] malononitrile (DCTB): Na matrix for U-PPD2 and U-PPD8 samples. LC-MS measurements, a mid-mass polar method coupled with UV-Vis detector was chosen to study the mass separation range between 200-1000 m/z for U-PPD2, U-PPD8, U-PPD16, and isolated compounds of U-PPD16.

Compounds corresponding to different emission centers were isolated from multi-emissive fluorophores by flash chromatography using a three-way pump (Buchi Sepacore, C-601) connected to a pump controller module (Buchi, C-610) coupled to an Ultrapure Silica Reverse Phase column (Buchi Cartridge, RP18ec). 500 mL solutions of ACN/water in different percentages (5%, 15%, 30%, 50%, 90% and 100%) were used as mobile phase/eluent. A sample containing 4% w/v U-PPD16 in 50/50 ACN: water was injected by a valve into the reverse phase column. FT-IR spectrum was recorded with Varian- 640-IR (Portmann Instruments GmbH). The conventional KBr pellet procedure (0.05% w/w of samples in KBr) was used for all samples. The FT-IR absorbance spectrum was recorded at a frequency range of 400-4000 cm^{-1} with 4 cm^{-1} resolution.

The chemical composition of the fluorophores was characterized using X-ray photoelectron spectroscopy (XPS, Physical Electronics, PHI VersaProbe II). The energy resolution and pass energy were 0.8 eV/step and 187.85 eV for survey scans and 0.125 eV/step and 29.35 eV for high-resolution scans, respectively. Carbon 1s at 284.5 eV was used as a reference to correct for charge effects. Samples were pressed onto Indium foil (Alfa Aesar, 99.99% purity).

AFM images were obtained with Nanosurf Ambient AFM variant (Flex-AFM) by utilizing AFM probe of SHR150 (BudgetSensors) with spring constants of 5 N/m and resonant frequency of 150 kHz. Aqueous solutions of U-PPD2, U-PPD4, U-PPD6, U-PPD8, and U-PPD16 with con-centration 0.005% and volume of 50 µL were drop-cast onto mica sheets (Science Services, 15x15 mm and 0.2 mm thickness) and completely dried for 2 hours at room temperature before starting the AFM measurement.

The UV-Vis absorption spectra for all samples were measured at room temperature with SynergyMx, Biotek Instruments GmbH in the wavelength range 250 nm – 800 nm with 2 nm increments.

Fluorescence measurements were performed by Horiba Jobin Yvon FluoroMax-4 for all samples. A concentration of 0.005% w/v was utilized for all samples since it gives the highest fluorescence emission. A range of excitation and emission wavelengths of 300-600 nm and

300-800 nm were used, respectively. A slit width of 5 nm was used for all samples for both excitation and emission wavelengths. Lifetime measurements for all samples were performed by Horiba DeltaPro for U-PPD2 and U-PPD16 at excitation wavelengths of 366 nm. LUDOX solution was used to calculate the instrument response factor (IRF). The quantum yield of U-PPD16 was measured directly with a spectrofluorometer (JASCO FP-8500) equipped with a 100 mm-diameter integrating sphere.

3.3.4 *Preparation of Polyvinyl Alcohol (PVA)/U-PPD16 Film*

A solution of 0.005% w/v of U-PPD16 containing 5% w/v Mowiol 40-88 in water was prepared and vigorously stirred at 60 °C for 12 hours. 1.5 mL of this solution was drop-casted on a polystyrene petri dish (d= 14 cm) and dried at 50 °C for 24 hours to let the water evaporate. The resulting films had a thickness of 200±20 μm.

3.3.5 *Oxygen Sensor Performance Test of Polyvinyl Alcohol (PVA)/U-PPD16 Film*

To measure the oxygen response, oxygen/nitrogen ratios of 0%, 1%, 2%, 4%, 8%, and 21% were purged within the spectrofluorometer chamber by mixing pure N_2 and O_2 gas with a flow-mixer setup (OxiQuant S, Envitec). Before each measurement, the sample was equilibrated at 100% N_2 for 30 minutes before it was purged with the targeted O_2/N_2 ratio for another 30 minutes.

Fluorescence measurements of U-PPD16 embedded in PVA films were performed within excitation wavelengths and emission wavelengths of 300-600 nm and 300-800 nm, respectively. A slit width of 5 nm was used for all samples for both excitation and emission wavelengths.

3.4   Results and Discussion

3.4.1 *Chemical characterization of the multi-emissive optical probes*

To investigate the mass distribution and relative concentrations of the individual fluorophores in the hydrothermal products synthesized with urea and PPD, I have used multiple mass spectroscopic techniques, namely MALDI-TOF, ESI-QTOF, and LC-MS. MALDI-TOF of U-PPD2 and U-PPD8 did not show any compound with m/z higher than 1000 Da, as

shown in Figure 3.1. This size corresponds to globular particles with a diameter of approximately 0.66 nm [185].
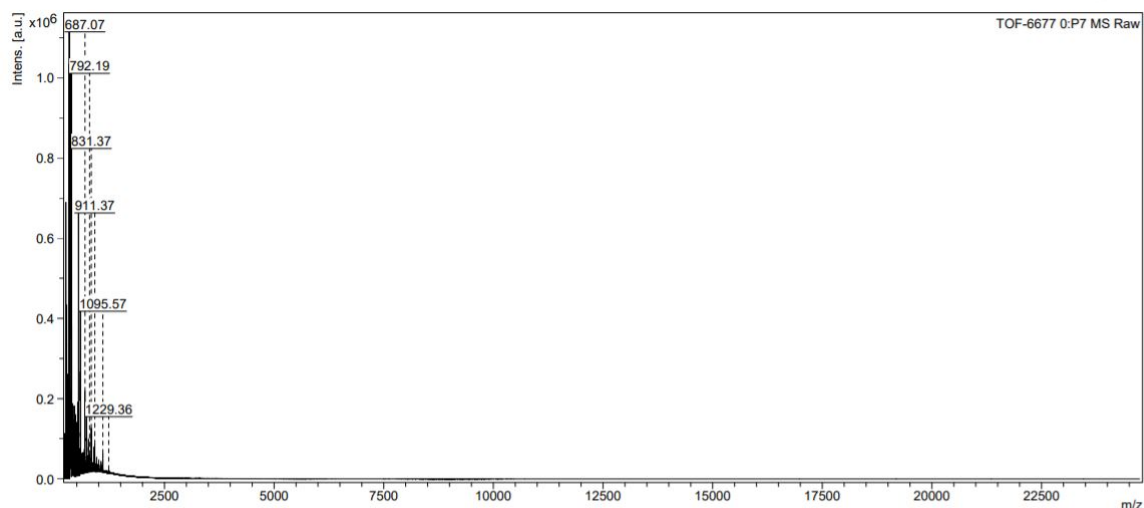
(a)
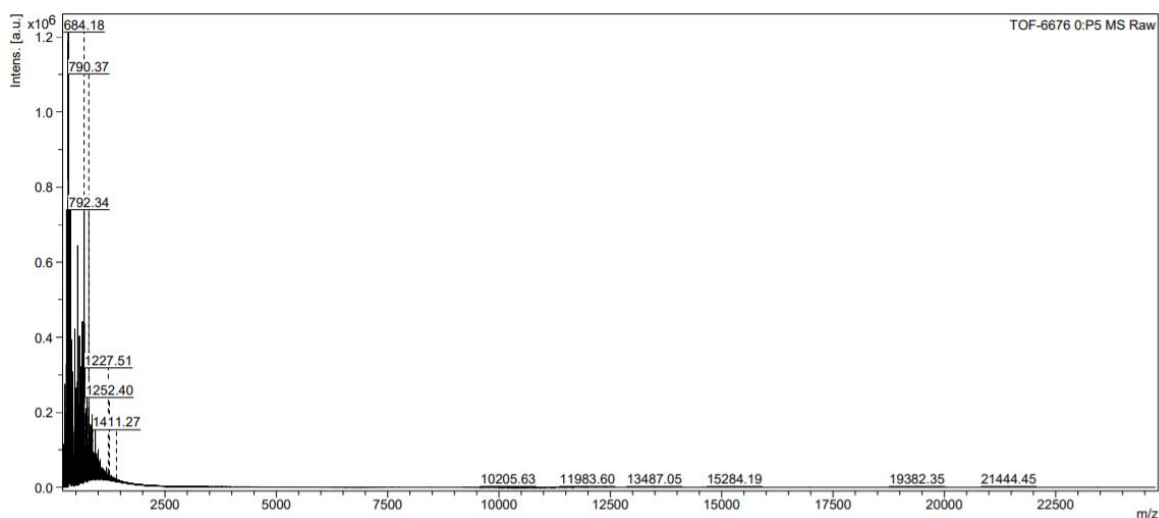
(b)

Figure 3.1 MALDI-TOF analysis of U-PPD2 (a) and U-PPD8 (b)

In addition, three main reaction products were indicated by ESI-QTOF in the lower molecular weight region (100-1000 m/z), namely compound A (560.985 m/z), B (426.946 m/z), and C (319.166 m/z), as shown in Figure 3.2a. Remarkably, the three components persist during the entire analyzed time range, although their relative intensity varied.

If the reaction time is increased above 8 hrs, compound C (319.166 m/z) constitutes the main product. This mass is consistent with the molecular weight of Bandrowski's base, a trimeric stable PPD oligomer produced by the self-polymerization of PPD with oxidizing agents under alkaline conditions (Figure 3.2b) [186]. Indeed, the relative intensity of the peak attributed to Bandrowski's base was only ~8% for U-PPD2, whereas it reached up to 50% for U-PPD16 (Figure 3.2a). The presence of Bandrowski's base as the main product at higher reaction times was also confirmed with LC-MS (Table 3.2 a-b). Combining these findings, we assume that the formation of the Bandrowski's base predominantly occurs as the reaction proceeds.
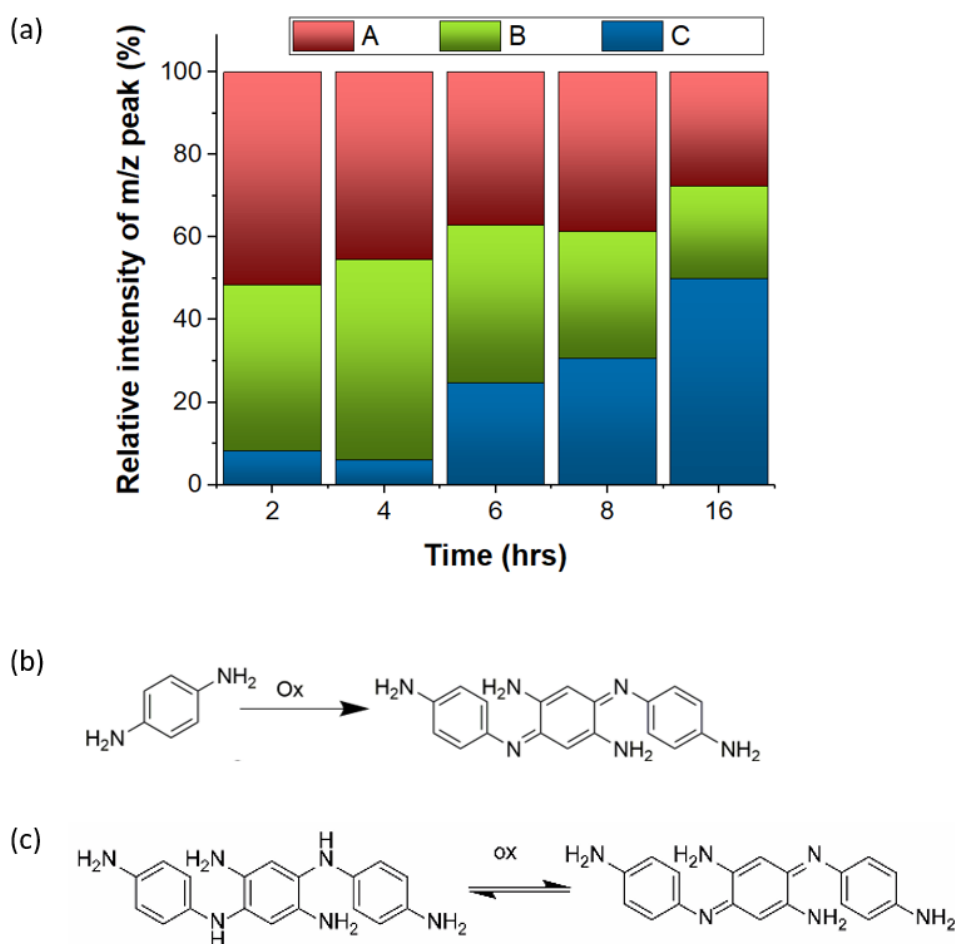
Figure 3.2. (a) Relative chemical composition (%) of products obtained during the hydrothermal synthesis with urea and PPD at different reaction times as determined by ESI-QTOF, namely compound A (560.985 m/z), B (426.946 m/z) and C (319.166 m/z) (b) Oxidative oligomerization of PPD to Bandrowski's base, (c) different oxidative states of Bandrowski's base.

Peak Number	Dominant Molecular Weight (Da)	Retention Time (min)	Area % Total
#1	319.3	1.49	1.13
#2	138.9	1.94	11.14
#3	138.9	2.05	19.98
#4	213.1	2.22	10.69
#5	213.1	2.31	19.17
#6	Multiple	2.45	6.82
#7	586.5	2.53	6.45
#8	543.5	2.71	14.59
#9	Multiple	4.79	8.39
#10	131.6	5.94	1.62

(a)

Peak Number	Dominant Molecular Weight (Da)	Retention Time (min)	Area % Total
#1	Multiple	0.57	7.73
#2	319.3	1.65	39.21
#3	214.1	1.81	2.54
#4	410.3	2.10	5.83
#5	410.3	2.15	6.51
#6	205.2	2.19	10.38
#7	408.1	2.27	3.00
#8	213.2	2.41	14.99
#9	340.5	2.52	5.48
#10	340.5	2.75	4.32

(b)

Table 3.2 LC-MS peak analysis of U-PPD2 (a) and U-PPD8 (b) with the molecular weight, retention time, and area % of each peak among all peaks.

The measured particle size determined by AFM decreases as a function of the reaction time (d_{U-PPD2} = 4.3±0.2 nm, d_{U-PPD6} = 3.4±0.2 nm, d_{U-PPD8} = 3.0±0.3 nm) up to 16 hrs where no particle could be observed anymore, as shown in Figure 3.3.

These results indicate that multi-emissivity might be related to the presence of low molecular weight fluorophores. A possible reason for the formation of such particles is the

non-covalent self-assembly of fluorophores bearing different chemical structures in this study by AFM for reaction times < 8 hrs.
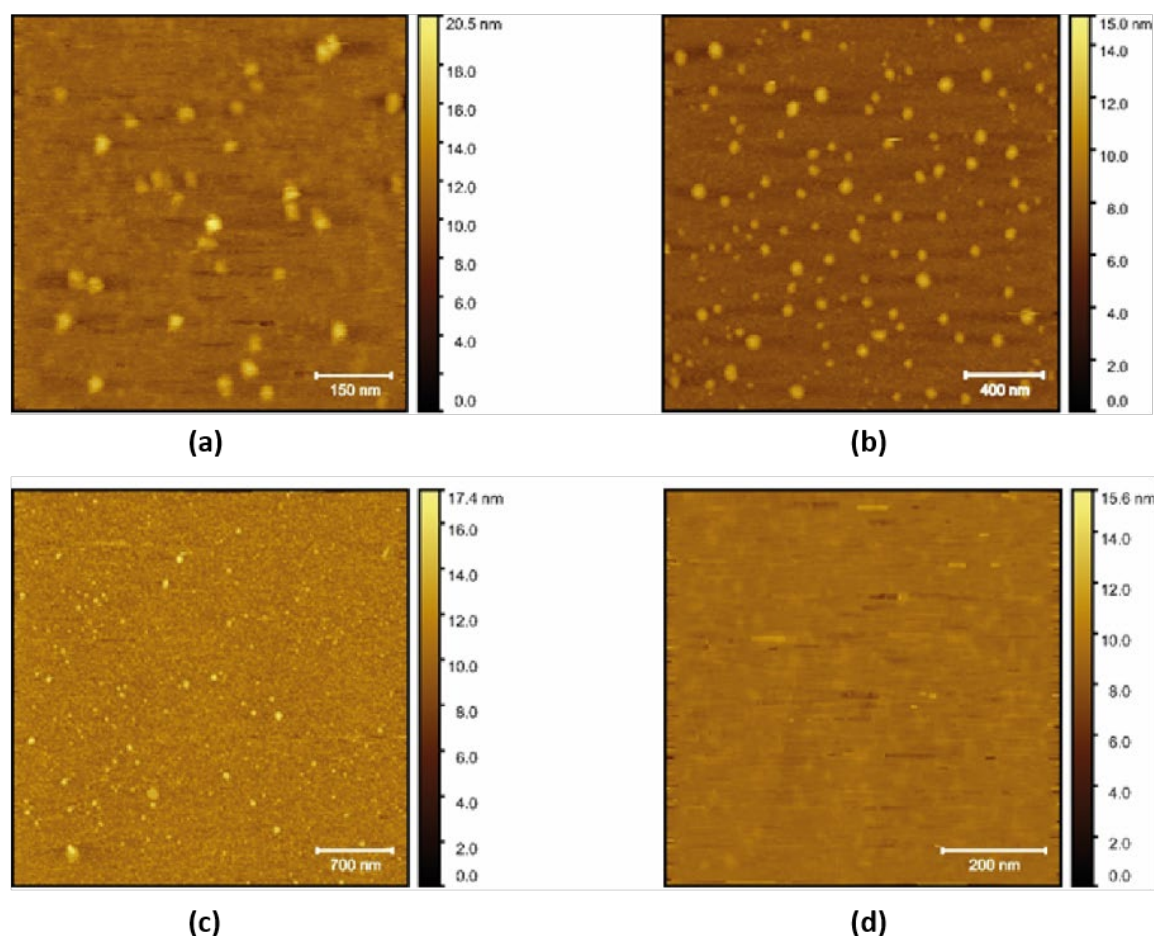
Figure 3.3 Dynamic mode AFM images of U-PPD2 (a), U-PPD6 (b), U-PPD8 (c) and U-PPD16 (d).

To understand which other molecules are synthesized at shorter reaction times and partially retained even after 16 h, I characterized U-PPD samples collected at different reaction times (from 2h to 16h) with FT-IR (Figure 3.4). FT-IR results showed that the symmetric -(C=O)NH stretching vibrations (amide I) of the urea bond[187] at 1594 cm^{-1} almost disappeared at the reaction times between 2h and 4h. Simultaneously, the intensities of the peak corresponding to C=O stretching vibrations of the carbonyl group of urea at 1675 cm^{-1} decreased as the reaction proceeded. By contrast, peaks corresponding to symmetric and asymmetric NH$_2$ stretching vibrations of primary amines of PPD located at 3328 cm^{-1} and 3372 cm^{-1} [188] increased in intensity as the reaction proceeded. A simultaneous decrease of urea functional units accompanied by an increase of amine units may suggest that polyaromatic ureas were synthesized at shorter reaction times (U-PPD2), then converted back to PPD (U-PPD4, U-

PPD6, and U-PPD8), which subsequently formed oligomers of aromatic di-amines at longer reaction times (U-PPD16). This finding is also in agreement with previously reported reaction pathways involved in high-temperature reactions of the single components or their mixtures [189]
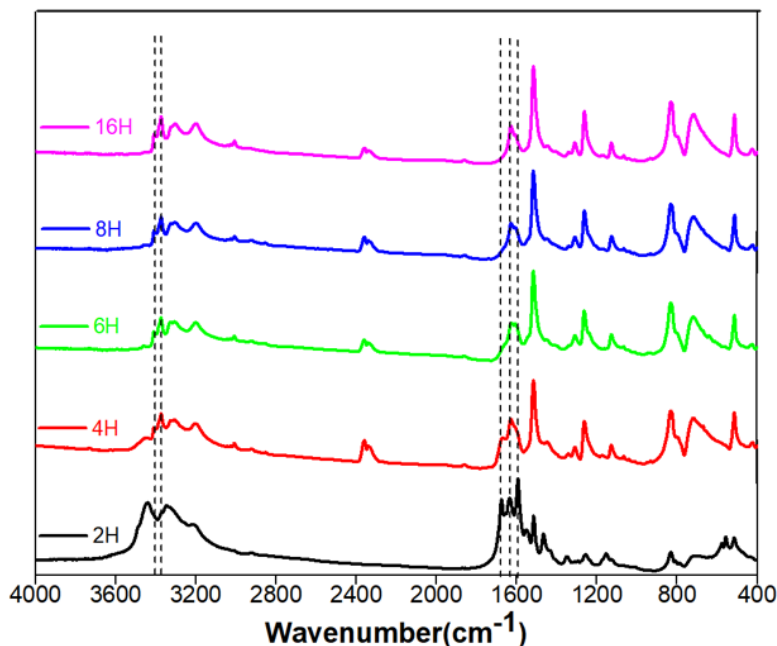
Figure 3.4. FT-IR spectra of U-PPD at 2, 4, 6, 8 and 16 h reaction time.

To get information on elemental composition and relative abundancy of functional groups for each hydrothermal product, I performed XPS on the U-PPD samples collected at different reaction times from 2 h to 16 h. XPS high-resolution region scans confirmed the set of structures of the fluorescent products suggested by ESI-QTOF, namely urea precursors, poly-aromatic urea units, unreacted and oligomerized PPD. Four different C1s signals located at 284.5 eV, 285.5 eV, 286.6 eV, and 288.5 eV were fitted and ascribed to C-C/ C-H, C-N, C=N, and N-C=O in agreement with previous literature [190-192] (Figure 3.5). The relative atomic concentration of carbon (C1s) remained constant (~71%) over the entire synthesis, whereas nitrogen (N1s) concentration decreased by 7% as the reaction proceeded from 2 to 16 hrs, suggesting the elimination of nitrogen-rich volatile products, such as ammonia (Table 3.2). This may indicate the release of nitrogen-rich volatile products due to the decomposition of polyaromatic urea units.
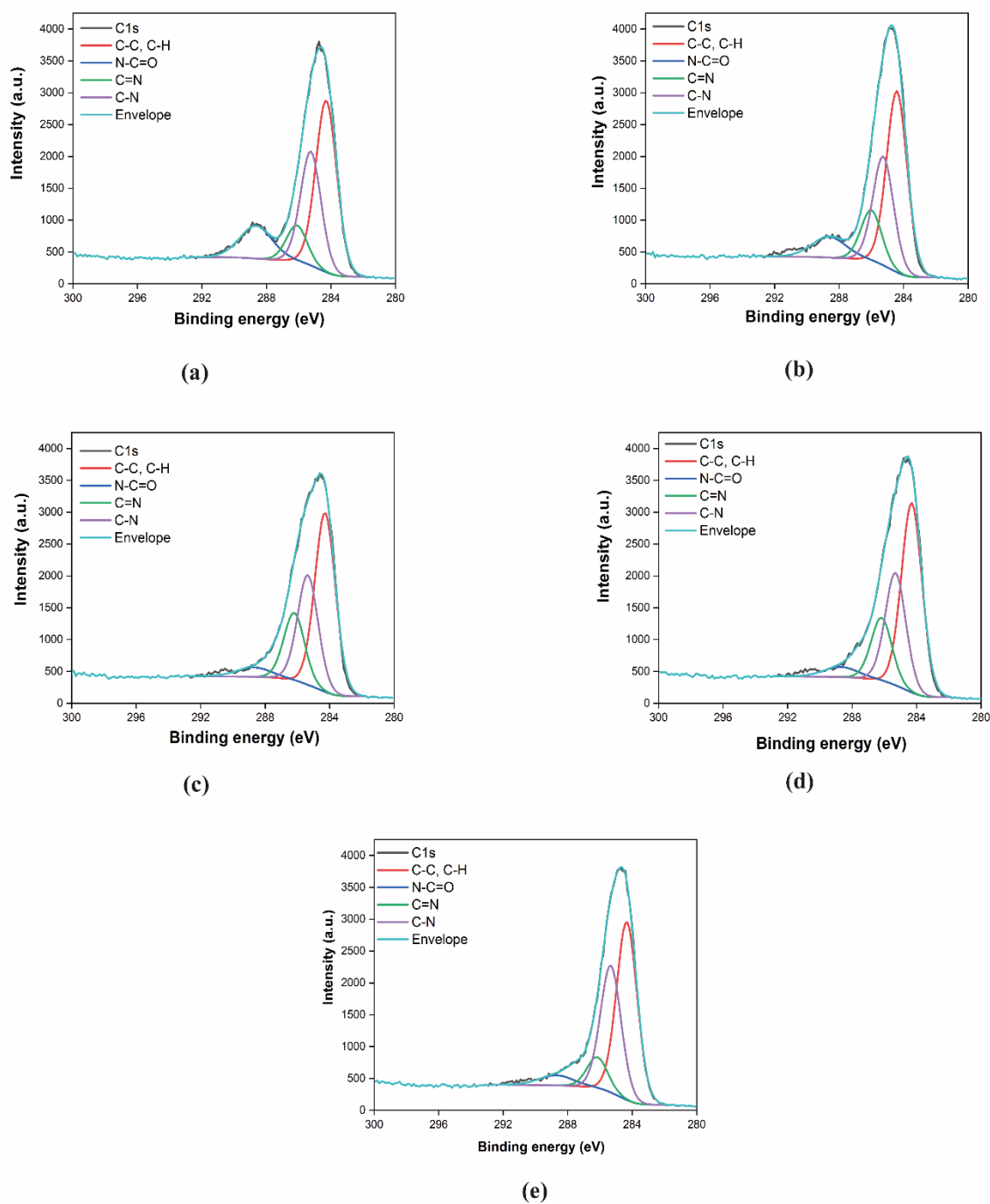
Figure 3.5 High resolution XPS spectra of C1s for U-PPD2 (a), U-PPD4 (b), U-PPD6 (c), U-PPD8 (d) and U-PPD16 (e).

Sample Name	C%	O%	N%
U-PPD2	69.11	7.64	23.24
U-PPD4	69.86	7.7	22.44
U-PPD6	71.54	11.76	16.7
U-PPD8	71.45	10.65	17.9
U-PPD16	71.76	10.52	17.72

Table 3.2. Elemental composition of U-PPD2, U-PPD4, U-PPD6, U-PPD8 and U-PPD16 by XPS.

In addition, the N1s peak can be fitted with two main peaks, ascribed to amino (-NH$_2$) (398.9 eV) and amide (-CONH$_2$/-CONHR/-CONR) (399.9 eV) functionalities [193,194] (Figure 3.6a-e). Interestingly, by monitoring their relative concentration change as a function of time, I could observe that the amide bond ratio among N-rich moieties decreases up to a reaction time of 6 hrs and stabilizes thereafter (Figure 3.6f). This may indicate that the predominant urea-bonds formed between aromatic moieties are partly decomposed, resulting in PPD mono-mers that can subsequently form PPD trimers, thereby displaying different oxidative states for the nitrogen.
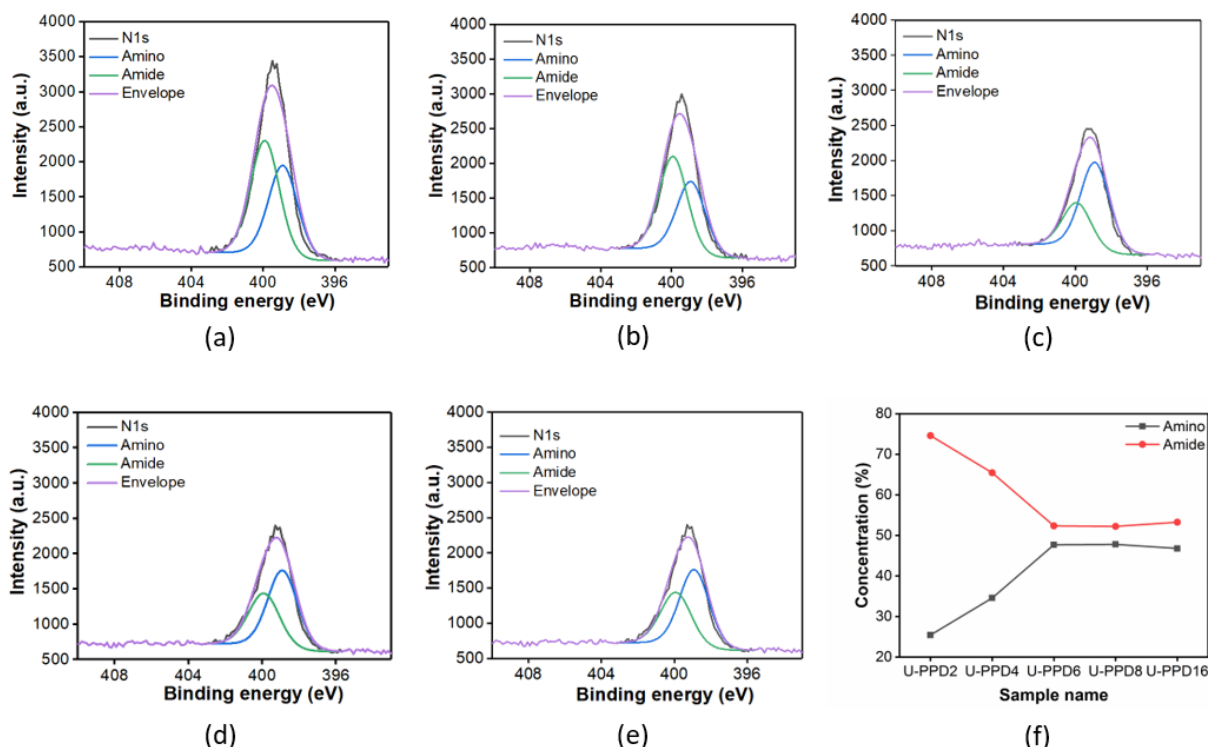
Figure 3.6 High resolution XPS spectra of N1s for U-PPD2 (a), U-PPD4 (b), U-PPD6 (c), U-PPD8 (d) and U-PPD16 (e). XPS analysis of U-PPD samples from 2 h to 16 h indicating the the change of N fraction from amino (black) and amide (red) groups with respect to the reaction time (f).

3.4.2 Optical characterization of the multi-emissive fluorophores

To investigate the relationship between chemical structures and optical properties of the fluorophores, I monitored the evolution of each emission center by recording multi-emission fluorescence patterns for U-PPD at reaction times of 2, 4, 6, 8, and 16h. Four emissive states were measured at a reaction time of 16 h (λ_{exc1} =303 nm, λ_{em1} =358 nm, λ_{exc2} =320 nm, λ_{em2} =390 nm, λ_{exc3} =360 nm, λ_{em3} =516 nm, λ_{exc4} =480 nm, λ_{em4} =618 nm) (Figure 3.7a). A quantum yield of 25.1 % was determined for U-PPD16, consistent with the literature where 24% was reported [195].
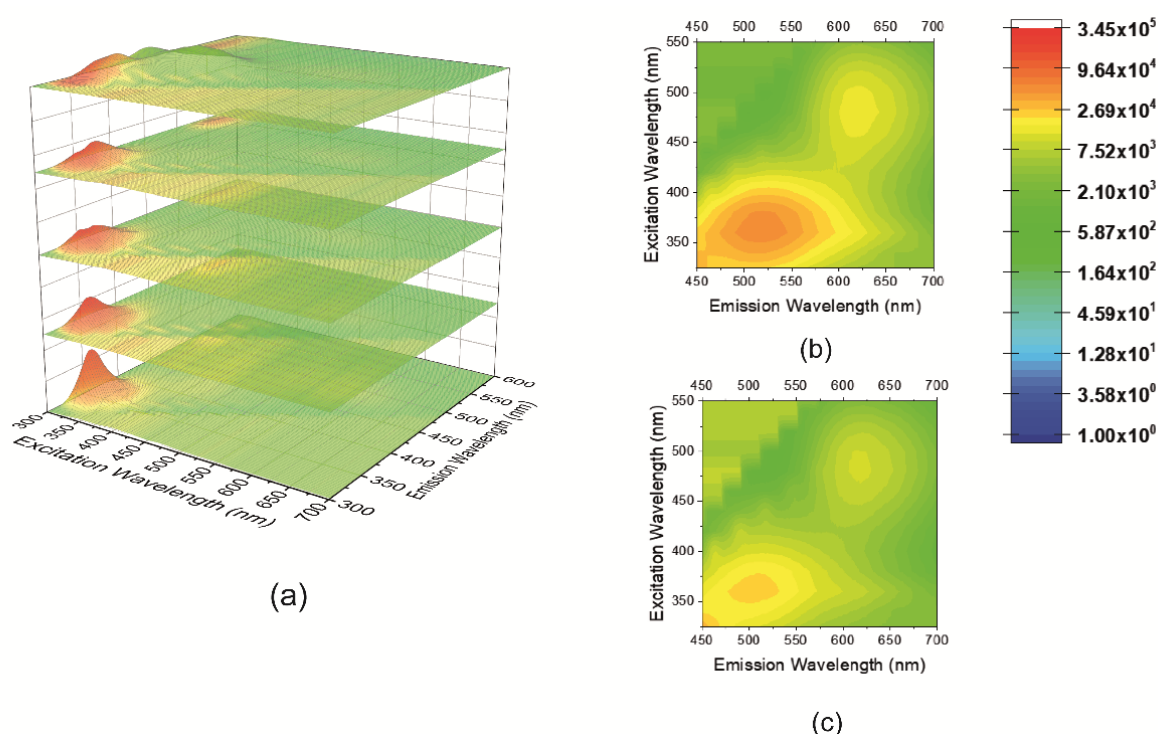
Figure 3.7 (a) 2D fluorescence surface color map of kinetic samples for U-PPD at reaction times of 2, 4, 6, 8 and 16 hrs (from bottom to top), 2D contour color map of U-PPD16 (b) and U-PPD8 (c) highlighting the third (λ_{exc3} =360 nm, λ_{em3} =516 nm) and the fourth (λ_{exc4} =480 nm, λ_{em4} =618 nm) emission center.

Bandrowski's base has been identified as the major component of samples collected at a reaction time of 16 hrs. Therefore, this compound was synthesized according to a previous protocol, and I recorded its fluorescence spectrum [196] (λ_{exc}= 580 nm, λ_{em}= 610 nm) (Figure 3.8). While the fluorescence emission of U-PPD16's fourth emission center is similar to that of Bandrowski's base, its excitation is blue-shifted by 100 nm in the present hydrothermal reaction (Figure 3.7b-c). This blue shift indicates an increase in the optical bandgap, which

might be related to energy transfer processes that occur with the other fluorophores present in the reaction medium.
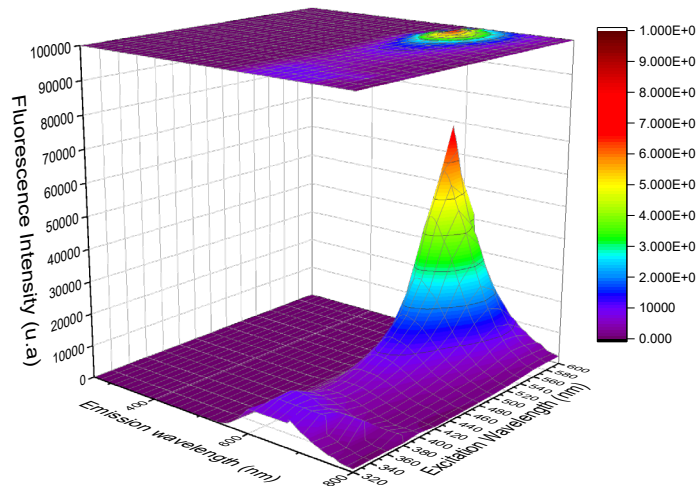
Figure 3.8 2D fluorescence color map of Bandrowski's base synthesized according to a previous literature method.

To investigate the chemical structures of the fluorophores corresponding to the other three emission centers (λ_{exc1} =303 nm, λ_{em1} =358 nm, λ_{exc2} =320 nm, λ_{em2} =390 nm, λ_{exc3} =360 nm, λ_{em3} =516 nm), I characterized the fluorescence emission of hydrothermal products from the individual precursors as well as from the mixture. The samples for spectrum recording were collected at a reaction time of 16 hrs from the hydrothermal vessel, where either air or oxygen-free headspaces were used (Figure 3.9). For pure D-PPD16 synthesized under an oxygen-free atmosphere, I observed an excitation peak at λ_{exc} =360 nm and an emission peak at λ_{em} =520 nm (Figure 3.9a). The emission peak was red-shifted if the reaction atmosphere was air (PPD16 (λ_{exc} =360 nm and λ_{em} =540 nm)) (Figure 3.9b). This may indicate that oxidative oligomerization of PPD is predominantly occurring under air conditions, resulting in red-shifting of the emission peak due to the increased π conjugation. The emission pattern of D-PPD16 and PPD16 strongly resembles the third emission peak of U-PPD16 located at λ_{exc3} =360 nm, λ_{em3} =516 nm, which suggests that oligomeric forms of PPD might be responsible for this emission center.
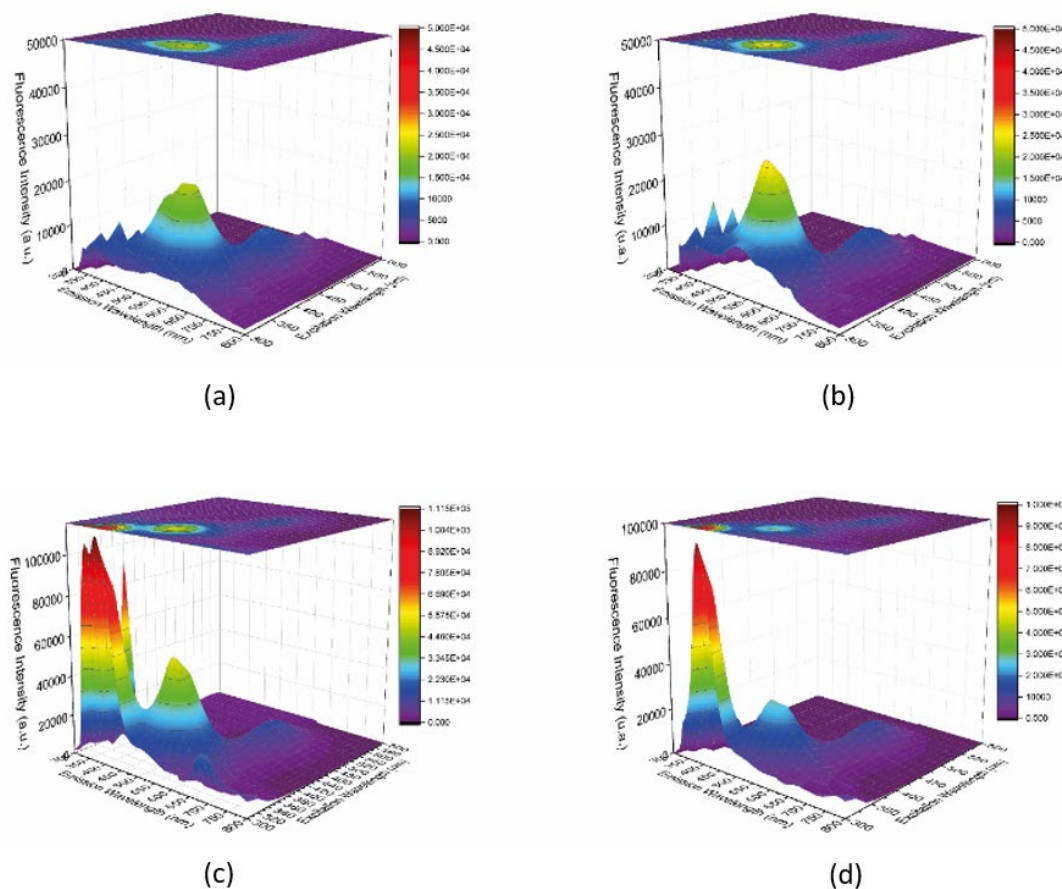
Figure 3.9 2D fluorescence color map of PPD16 (a), D-PPD16 (b), U-PPD16 (c) and D-U-PPD16 (d).

The coexistence of two emissive states within different oligomeric forms of PPD can be related to the redox equilibrium between PPD and benzoquinone di-amines moieties. This is further confirmed by the increased fluorescence intensity of U-PPD (by 76%) at λ_{em3} = 516 nm, compared to D-U-PPD16 (Figure 3.9c,d). Absorption studies further confirmed the presence of both benzenoid rings of the oligomeric derivatives of PPD [197] with π–π* transitions at 292 nm and 312 nm and quinoid rings in p-phenylene quinone diimine (PPQD) [198] with π–π* transition at 415 nm. Furthermore, at higher reaction times, oligomerization of PPQD is observed by the occurrence of broader adsorption located at 485 nm (t = 16 h). Indeed, this absorption band at 485 nm is consistent with the absorption of Bandrowski's base (i.e., 480 nm at a pH value of 7.5) [199] (Figure 3.10). This finding is also consistent with the 2D contour color maps of U-PPD16 and U-PPD8, showing the evolution of the fourth emission center (λ_{exc4} = 480 nm, λ_{em4} = 618 nm) as the reaction proceeds, as shown in Figure 3.7b,c.
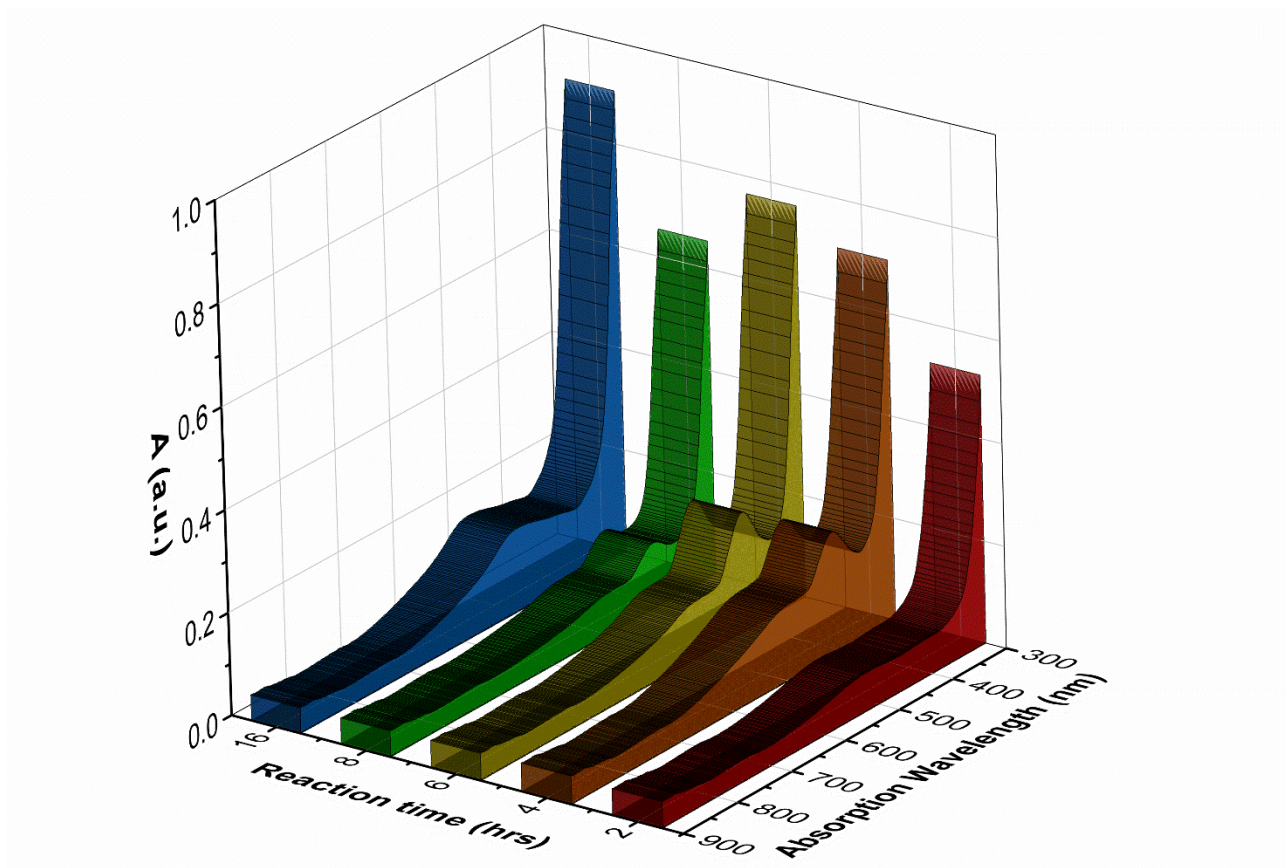
Figure 3.10 UV-Vis spectra of U-PPD at 2, 4, 6, 8 and 16 hrs reaction time.

The fluorescence intensity ratio between the second emission center (λ_{exc2} = 320 nm, λ_{em2} = 390 nm), which appears as early as U-PPD4, and the first emission center (λ_{exc1} = 303 nm, λ_{em1} = 358 nm) strongly increases at longer reaction times, as indicated in the 2D fluorescence contour plots (Figure 3.7). This may suggest that PPD is slowly converted back from aromatic polyurea compounds. Indeed, the PPD precursor (p-phenylenediamine) emission is located at 385 nm (Figure 3.11). Moreover, it is possible to assign the first emission center (λ_{exc1} = 303 nm, λ_{em1} = 358 nm) to aromatic polyurea compounds. Despite their higher conjugation, the relatively high optical bandgap might be due to multiple orbital nodes among their structures.
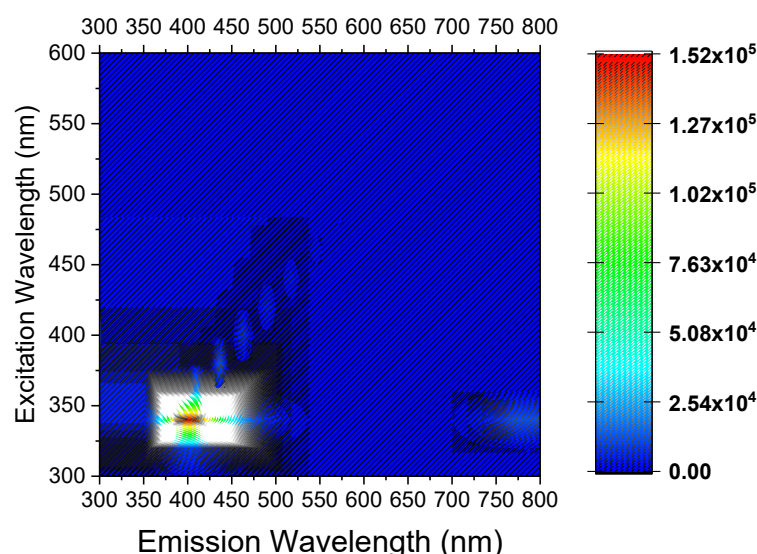
Figure 3.11 2D fluorescence contour plot of p-phenylenediamine.

To investigate the formation of a new energy pathway with respect to the reaction time, lifetime measurements were performed for U-PPD2 and U-PPD16. The lifetime biexponential decay curve for U-PPD2 at an excitation wavelength of 366 nm was bi-exponential (τ_1 = 0.43 ns, τ_2 = 3.27 ns; $\tau_{average}$ = 0.58 ns). Interestingly, I observed an additional component with longer lifetimes for U-PPD16. The average lifetime of U-PPD16 increased approximately six-fold (τ_1 = 0.55 ns, τ_2 = 3.21 ns, τ_3 = 6.15 ns; $\tau_{average}$ = 3.01 ns) (Table 3.3). This could be due to the formation of new oligomeric structures of PPD and its derivatives at increasing reaction times.

The excitation-dependent emission pattern observed for all emission centers is likely due to the broad structural distribution of PPD-derivatives, similar to what has been simulated with low molecular weight polycyclic aromatic moieties for citric acid-based CNDs [200]. Isolation of the compounds corresponding to the three emission centers by flash chromatography further confirmed the different chemical nature of the fluorophore mixture. The oligomeric PPD compounds with an emission center located at 511 nm were extracted by collecting the fractions with 5% *v/v* ACN in water as eluent. The other two compounds with emission centers related to the single PPD precursor (λ_{em2} = 402 nm) and Bandrowski's base (λ_{em2} = 606 nm) nm were eluted with 15% *v/v* of ACN in water (Figure 3.12).

	Lifetime (ns)	Amplitude
T_1	0.43	70.28 %
T_2	3.27	29.72 %
Average	0.585	

(a)

	Lifetime (ns)	Amplitude
T_1	0.55	6.66 %
T_2	3.21	41.37 %
T_3	6.15	51.97 %
Average	3.01	

(b)

Table 3.3 Lifetime measurements of U-PPD2 (a) and U-PPD16 (b)
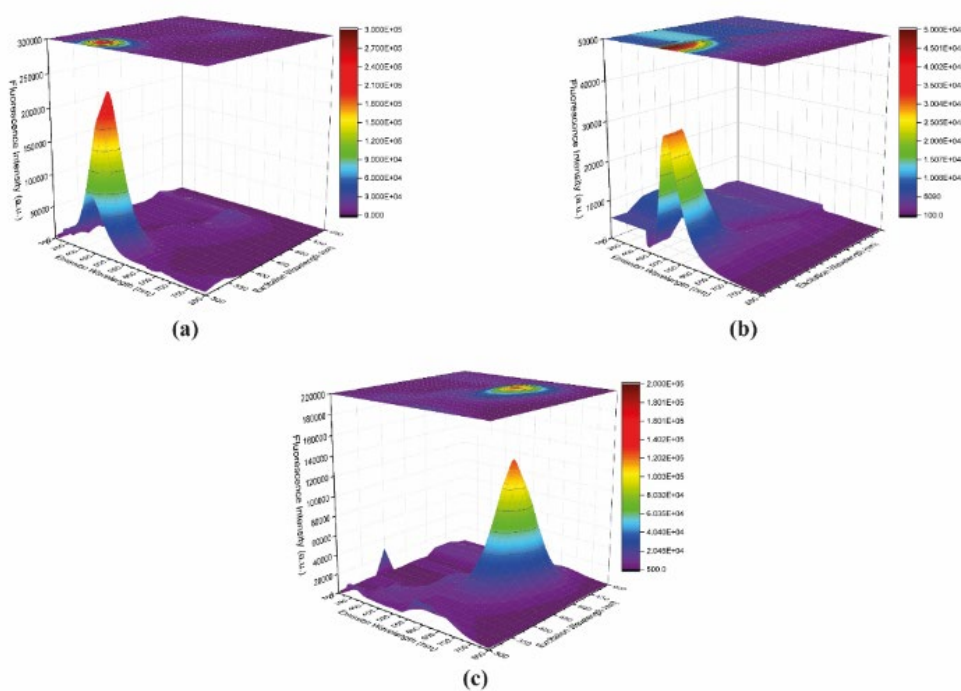
Figure 3.12 2D fluorescence color map of isolated compounds with emission centers located at λ_{exc}= 340 nm, λ_{em} = 402 nm (a), λ_{exc} = 420 nm, λ_{em} = 511 nm (b) and λ_{exc} = 520 nm, λ_{em} = 606 nm (c).

3.4.3 Fluorescent PVA Films and their Multi-Emissive Oxygen Sensing Properties

The previously reported solvothermal synthesis of CNDs from m-phenylenediamine [181], ethylenediaminetetracetic acid [171], and isophorone di-isocyanate [172] resulted in a set of multi-emissive fluorophores. To test whether the fluorophores synthesized here also display RTP emission when embedded into a PVA matrix (Mowiol 40–88), I measured the luminescence emission before and after encapsulating them within the matrix.

The emission centers previously located at λ_{exc2} = 320 nm, λ_{em2} = 390 nm, λ_{exc3} = 360 nm, λ_{em3} = 516 nm, λ_{exc4} = 480 nm, λ_{em4} = 618 nm underwent blue-shifts in the emission by 80 nm, 100 nm and 60 nm, respectively (Figure 3.13). Meanwhile, their intensity increased by 21%, 56%, and 32%, respectively (Figure 3.13 vs. Figure 3.7). Similarly, an increased intensity has been observed for CNDs synthesized from ethanediamine precursors if they were embedded into PVA films and fibers [201]. A blue shift has been observed in a similar system where CNDs synthesized from *m*-phenylenediamine were embedded into a PVA matrix, and the blue shift was ascribed to the absence of any solvent relaxation [181].
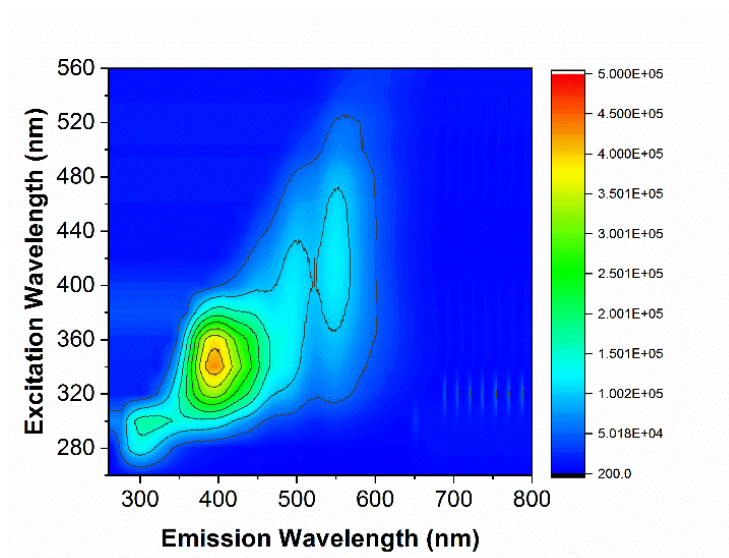
Figure 3.13 2D fluorescence contour plot of the PVA films with U-PPD16 embedded within the polymer matrix.

To investigate the possible oxygen sensing property of these multi-emissive fluorescent PVA films, I recorded their 2D fluorescence contour plots at 0, 1, 2, 4, 8, and 21% O_2 (Figure 3.14a–c). Fluorescence quenching was observed for all three emission centers when the O_2/N_2 ratio increased up to 8% of O_2. The resultant Stern-Volmer plots were fitted to the second-order polynomial function, as shown in Figure 3.14d (R^2 equal to 0.964, 0.928, and 0.941 for 1st, 2nd, and 3rd emission center, respectively). The limit of detection (LOD) was calculated according to the extrapolated concentration at which the signal is three times the

averaged standard deviation (3σ) of the fluorescence intensity. The LOD of each emission center was 0.886%, 0.669% and 0.755% O_2, respectively. The fitting showed a non-linear calibration plot which confirms that the sensor microenvironment plays a role in the collisional quenching between the luminescent dye and oxygen [202]. To exclude any irreversible photo-oxidation processes, I performed up to three 0–21% O_2 cycles (Figure 3.14f). The unsatisfactory reversibility was observed for each emission center due to the ease of photo-oxidation of p-phenylenediamine-based oligomers under oxidative conditions.

To test the sensor cross-interference to ambient relative humidity and CO_2, we recorded the 2D fluorescence contour plots of fluorescent PVA films under ambient air and O_2/N_2 dry gas mixture conditions. The emission wavelength and intensity did not change for all three emission centers when the fluorescent PVA films were exposed to ambient air conditions and subsequently purged with O_2/N_2 dry gas mixture at an oxygen pressure of 21 kPa (Figure S9). The lack of interactions between the emission centers and water/ CO_2 was confirmed by the retention of the fluorescent features.

To investigate the quenching mechanism, I also performed lifetime measurements under air and argon atmosphere upon excitation at 366 nm. The average lifetime of fluorescent PVA films ($\tau_{average}$= 6.6 ns in argon and $\tau_{average}$= 0.4 ns in air) was shorter compared to that of phosphorescence (from µs to s) (Figure 5e). This confirms that fluorescence quenching is triggered by oxygen, although no transition to the triplet state is observed. While the exact nature of this mechanism is still under debate, similar behavior has already been observed in other N-rich aromatic rings such as β-carbolines[182] and acridines[183]. This is reputed to occur as a result of the formation of charge-transfer complexes between the contact radical ion pair state $^3(^2M^{•+},2O^{2•-})$ when mixed with the locally excited (LE) states[184]. These intermediate energy level states possibly enable the energy matching with the triplet ground state and excited singlet state bandgap of molecular oxygen.
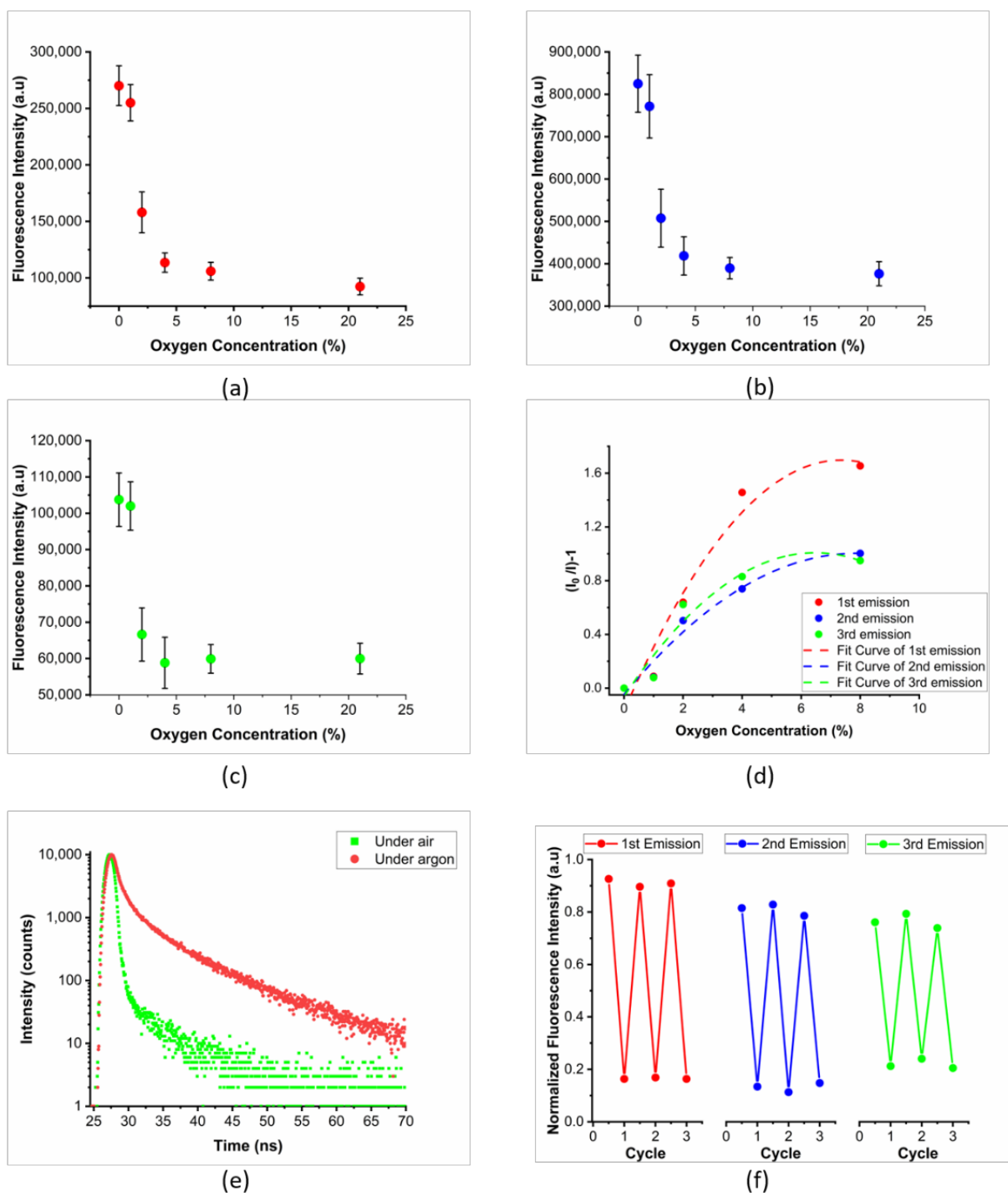
Figure 3.14 Fluorescence intensity of polymer films composed of U-PPD16 embedded in a PVA matrix (Mowiol 40–88) as a function of the oxygen concentrations (%) for the emission centers of 310 nm (**a**), 400 nm (**b**) and 550 nm (**c**). (**d**) Non-linear Stern–Volmer calibration plot of each emission center and 2nd order polynomial fit. (**e**) Fluorescence emission decay curve of the functional PVA film under air and argon. (**f**) Reversibility of oxygen sensing by the functional PVA film for each emission center during three consecutive 0–21% O_2 cycles.

Although the precise underlying mechanism remains unclear, we demonstrate the example of multi-emissive optical oxygen sensing. Such a feature is particularly advantageous for the reversible and non-destructive monitoring of oxygen. Future studies will verge on understanding the exact role of aromatic amines in oxygen quenching once they are embedded within a hydrogen bonding matrix.

3.5 Conclusion

Multi-emissive fluorophores were produced through a hydrothermal synthesis with urea and PPD as starting materials. From ESI-QTOF analysis, I identified three main components whose ratios vary as a function of the reaction time. At longer reaction times (t >8 h), Bandrowski's base, a trimer of PPD, constitutes the main component. Once U-PPD16 is embedded in a PVA matrix, it has been demonstrated that the films undergo oxygen-induced fluorescence quenching at all three emission centers. The quenching follows the non-linear Stern–Volmer plots and gives a LOD of 0.886%, 0.669%, and 0.755% O_2 for each emission center, respectively. However, the oxygen sensor showed unsatisfactory reversibility during only up to three cycles, which could limit the use of the multi-emissive optical oxygen sensor in long-term applications. Thanks to the cost-effective and metal-free formulation, these sensors have the potential to be used in food packaging to monitor the oxygen concentration by cross-referencing each single emission center to the relevant dynamic oxygen range. In addition, this work opens up new perspectives in the development of fluorescence-based optical oxygen sensors

Chapter 4

Reversible and Broad-Range Oxygen Sensing Based on Purely Organic Long-Lived Photoemitters

Note: This chapter has been published in " Reversible and Broad-Range Oxygen Sensing Based on Purely Organic Long-Lived Photoemitters", E. Armagan, K. Wei, G. Fortunato, E. Amstad, R.M. Rossi, ACS App. Poly. Mater., 3, 2480-2488 (2021). E. Armagan performed the fluorophores synthesis and its chemical, optical and sensor characterization by FT-IR, HR-TEM, Fluorescence spectraphotometer, lifetime analysis, as well as all sensor performance test. E. Armagan also analysed all the data and wrote the manuscript with the input from all authors.

4.1 Abstract

Purely organic optical reversible O_2 sensors that can work with a broad O_2 concentration range and robust reversibility are of growing importance for a wide variety of application areas, for example, life sciences and food packaging. In the previous chapter, I developed multi-emissive urea-linked di-amine based luminophores with an O_2 sensitivity range of 0-8% O_2. However, their unsatisfactory sensor reversibility hinders the use of these sensors in long-term applications. Therefore, I hereby developed a purely organic optical O_2 sensor by embedding polyimide-based photoemitters within a poly(vinyl alcohol) (PVA) matrix. The photoemitters are synthesized through one-pot hydrothermal reactions. They have a lifetime of room temperature phosphorescence (RTP) of up to a few microseconds (μs) when they are embedded into the polymer matrix. These results demonstrate that the photoemitters have higher sensitivity and broader sensing range to O_2 if they are synthesized with longer reaction times because they possess a more rigid polyimide structure. The O_2 sensor with such optimized photoemitters embedded in the polymer matrix exhibits continuous and broad-range O_2 sensing in the range of 0-16% O_2. The Stern-Volmer quenching constant (K_{sv}) was calculated to be 0.2351 kPa^{-1} for the linear response range of 0-4% O_2.

Moreover, the O_2 sensor can be repetitively used at least ten times in the linear range (0-4% O_2) or beyond the linear range (up to 21% O_2). The good reversibility was attributed to the photo and chemical stability of polyimide nanoparticles. The metal-free, purely organic sensors that enable continuous and repetitive detection of O_2 within a relevant O_2 sensing range are appealing, especially for monitoring packaged food, biomonitoring, and biosensing.

4.2 Introduction

Purely organic photoemitters with room temperature phosphorescence (RTP) are promising materials for O_2 sensing, thanks to their low cost, ease of production, and efficient recombination pathway at room temperature. RTP has been observed when heteroatoms of purely organic photoemitters are bonded to aromatic compounds such as aromatic di-ke-tones,[203] di-acids, di-esters[204], and di-amines,[205] or functionalized with heavy halogen atoms such as chlorine,[206] bromine[207], and iodine[208]. The quantum yield (QY) of such RTP photo-emitters can be improved by inhibiting their internal molecular motions in various ways, including the development of crystallization-enhanced systems,[204,209] the induction of aggregation-induced intersystem crossings,[210] the encapsulation of organic photoemitters within rigid cages[211] and structural rigidification through covalent[212] or non-covalent interactions[213–215]. Although a wide range of purely organic long-lived photoemitters with RTP has been developed, only a few studies have investigated their O_2 sensing performance.[216-218] For example, various phosphorescence QY was achieved with a difluoroboron dibenzoylme-thane-poly(lactic acid) solid-state sensor where the heavy halogen atom effect was employed, resulting in a linear dependency on the O_2 concentration up to 1% O_2. However, the O_2 calibration curve displays non-linearity beyond 1% O_2 concentration, rendering the broad range calibration within an O_2 concentration of 1-100% difficult[219]. DeRosa et al. developed Difluoroboron β-Diketonate Polylactide photoemitters that display a linear dependency on the O_2 concentration within the full range if functionalized with iodide (I)[220]. However, β-Diketonate based compounds can undergo photodegradation during UV exposure, leading to poor photostability of these luminophores and hence, a poor sensing reversibility[221].

In the previous chapter, I studied purely organic para-phenylenediamine (PPD) based photoemitters embedded in a high molecular weight poly(vinyl alcohol) (PVA) matrix. Their fluorescence is quenched within the range of 0-8% O_2[222]. However, the non-linear calibration curve and unsatisfactory reversibility have hampered their further use. In this study, I introduce a new purely organic solid-state optical O_2 sensor composed of polyimide-based RTP photoemitters, which are embedded in a PVA matrix to repetitively enhance the O_2 response. The photoemitters were synthesized from mellitic acid (MA) and PPD by using polyimide chemistry, thus named MA-PPD. Thanks to the structural rigidity and strong intermolecular interactions, polyimides have an improved RTP quantum yield[223-225]. In particular, I embedded the most efficient RTP photoemitter, MA-PPD6, in a PVA matrix that inhibits the intermolecular motion via the abundance of hydrogen bond donor and acceptor groups, thereby

improving phosphorescence emission. The resulting O_2 sensor can reversibly detect O_2 in the range of 0-16% without significant losses in sensitivity: it has a linear dependence on the O_2 concentration in the range of 0-4% O_2 and a non-linear dependency in the range of 4-16% O_2.

4.3 Experimental Section

4.3.1 Materials

PPD (≥99%) and mellitic acid (MA) (≥99%) were purchased from Sigma-Aldrich (St. Louis, MO, USA) and Tokyo Chemical Industry (Tokyo, Japan), respectively, for the synthesis of luminophores. Ultra-pure water (Milli-Q) was used as a solvent for the reactions. Potassium Bromide (KBr) was obtained from Merck (Darmstad, Germany) for the pellet preparation. PVA polymer (Mowiol 40-88, Mw ~ 205,000 Da) was obtained from Sigma-Aldrich. Oxygen (O_2) (99.99%), nitrogen (N_2) (99.8%), and carbon dioxide (CO_2) (99.99%) were purchased from Carbagas (Zurich, Switzerland) for the sensor performance studies.

4.3.2 Synthesis of the Luminophores

A PPD and MA precursor mixture (1 mg/mL) was prepared in a 3:1 molar ratio in ultra-pure water. The prepared mixture solution was vigorously stirred for 30 minutes at room temperature. Subsequently, the solution was transferred to a polytetrafluoroethylene (PTFE) lined synthesis autoclave reactor (Parr Instrument, Acid Digestion Vessel) with a volume of 50 mL. The autoclave reactor was placed in a pre-heated oven (Series ED Avantgarde Line, BINDER, Spain) at 180 °C for different reaction times. The products, MA-PPDx, were then dried in a freeze-dryer (Alpha 3-4 LSC basic, Martin Christ, Germany) for 24 hours, resulting in MA-PPDx, where MA, PPD, and x represent mellitic acid, para-phenylenediamine, and reaction time (in hours), respectively.

4.3.3 Characterization Techniques

Fourier Transform Infrared (FT-IR) spectra were obtained with a Varian-640-IR (Portmann Instruments GmbH, Biel-Banken, Switzerland) operated in the wavenumber range of 400-4000 cm^{-1} with 2 cm^{-1} spectral resolution. The pellets were prepared by mixing 0.05% w/w KBr into MA-PPDx powder for the quantitative FT-IR analysis.

The relative imide/amide content obtained from quantitative FT-IR analysis was calculated as follows: C-N peak of amide and imide group was deconvoluted in the wavenumber range of 1350-1450 cm^{-1} using Gaussian fitting with a multi-curve peak analyzer in OriginLab. Afterward, the area under each deconvoluted peak was calculated with the integration tool in OriginLab to obtain the relative imide/amide content.[226]

X-Ray Photoelectron Spectroscopy (XPS) was performed on a PHI VersaProbe II (Physical Electronics, Chanhassen, MN, USA) to investigate the chemical composition of the luminophores. The spectra were recorded with the energy resolution of 0.8 eV/step and pass energy of 187.85 eV for survey scan, and the energy resolution of 0.125 eV/step and pass energy of 29.35 eV for high-resolution scans. Carbon 1s at 284.5 eV was used as a reference to correct the charge effects. The samples were prepared by pressing MA-PPDx powders onto Indium foil (Alfa Aesar, 99.99% purity, Kandel, Germany).

The relative imide/amide content obtained from quantitative XPS analysis was calculated as follows: The data were analyzed using the CasaXPS (Casa Software Ltd, UK). The N1s peaks were deconvoluted into three main peaks, corresponding to amide, imide, and protonated N functionalities.[227,228] The area under each deconvoluted peak was calculated to determine the relative imide/amide abundance.

Prior to the High-Resolution Transmission Electron Microscopy (HR-TEM) measurement, 0.05% (w:v) of a MA-PPDx solution was drop-casted on TEM grids (Carbon film-coated, 400 mesh, Cu) (Electron Microscopy Sciences, PA, USA). The HR-TEM images were obtained with a JEOL JEM-1400 Plus (JEOL Ltd., Tokyo, Japan) operated at an acceleration voltage of 120 kV with the detector of JEOL CCD camera Ruby.

The photoluminescence (PL) of MA-PPDx luminophores in an aqueous medium or a polymer matrix were measured with a Horiba Jobin Yvon FluoroMax-4 (Horiba Jobin Yvon GmbH, Bensheim, Germany). To determine the concentration for the highest PL intensity, a concentration series of 0.005%, 0.01%, 0.02%, 0.03%, 0.05%, 0.1%, 0.2% and 0.5% (w:v) was used for all MA-PPDx. The excitation range of 280-600 nm and emission range of 300-800 nm were used with the slit width of 3 nm.

The lifetime of all MA-PPDx was quantified with a Horiba DeltaPro (Horiba Jobin Yvon GmbH, Bensheim, Germany) at the excitation wavelength of 510 nm. LUDOX solution was used to calculate the instrument response factor (IRF).

4.3.4 Fabrication of PVA/MA-PPDx Films

The solution was prepared by adding 0.05% (w:v) of MA-PPDx and 5% PVA powder (Mowiol 40-88) to ultra-pure water. Subsequently, the mixture was vigorously stirred at 60 °C for 12 h. 1 mL of the solution was dropped on a polystyrene Petri dish and dried at 50 °C for 24 h to evaporate the water.

4.3.5 O_2 Sensor Performance Test of PVA/MA-PPDx Films

To test the oxygen sensitivity, a custom-built environmental chamber located in the spectrofluorometer chamber was purged with an O_2/N_2 gas mixture containing 0%, 1%, 2%, 4%, 8%, 12%, 16% and 21% O_2. The gas fluxes were controlled with a flow-mixer setup (OxiQuant S, Envitec GmbH, Wismar, Germany). Specifically, before each measurement, the film was kept at 100% N_2 flow for 20 minutes. Subsequently, it was purged with the targeted O_2/N_2 mixture for another 20 minutes. Photoluminescence measurements were obtained at the desired O_2/N_2 ratio by exciting the sensors in a range of 280-600 nm and recording an emission spectrum in the range of 300-800 nm.

The lifetime analysis was performed with a Horiba DeltaPro (Horiba Jobin Yvon GmbH, Bensheim, Germany) for all PVA/MA-PPDx films at the excitation wavelength of 510 nm under standard air and anoxic environment (100% N_2).

To test the sensor reversibility, the O_2 concentration in the custom-built chamber was switched between 0 and 4% O_2 or between 0 and 21% O_2 for 10 times. The measurement chamber was purged with a mixture of N_2/CO_2 at the ratio of 60:40 or N_2/CO_2 at the ratio of 100:0 to investigate the sensor cross-sensitivity towards CO_2. Similarly, the chamber was respectively kept under 80% and 20% relative humidity level at room temperature while purging with constant N_2/O_2 flow at the ratio of 79:21 to test the cross-interference of humidity.

4.4 Results and Discussion

4.4.1 Chemical Characterization of MA-PPD photoemitters

MA-PPD photoemitters were synthesized for different durations as described in the method and according to the literature[227]. The photoemitters synthesized with different reaction times, named MA-PPDx with x indicating the reaction time in hours, were evaluated based on chemical and optical characterization. Nanometer-sized particles with diameters of 3 nm were synthesized at a constant precursor concentration of 1 mg/mL,[226] as shown in the HR-

TEM images in Figure 4.1 and summarized in Table 4.1. Note that the reaction time does not affect the average size of the photoemitters, indicating that the nanoparticles reach the final size in the first two hours.
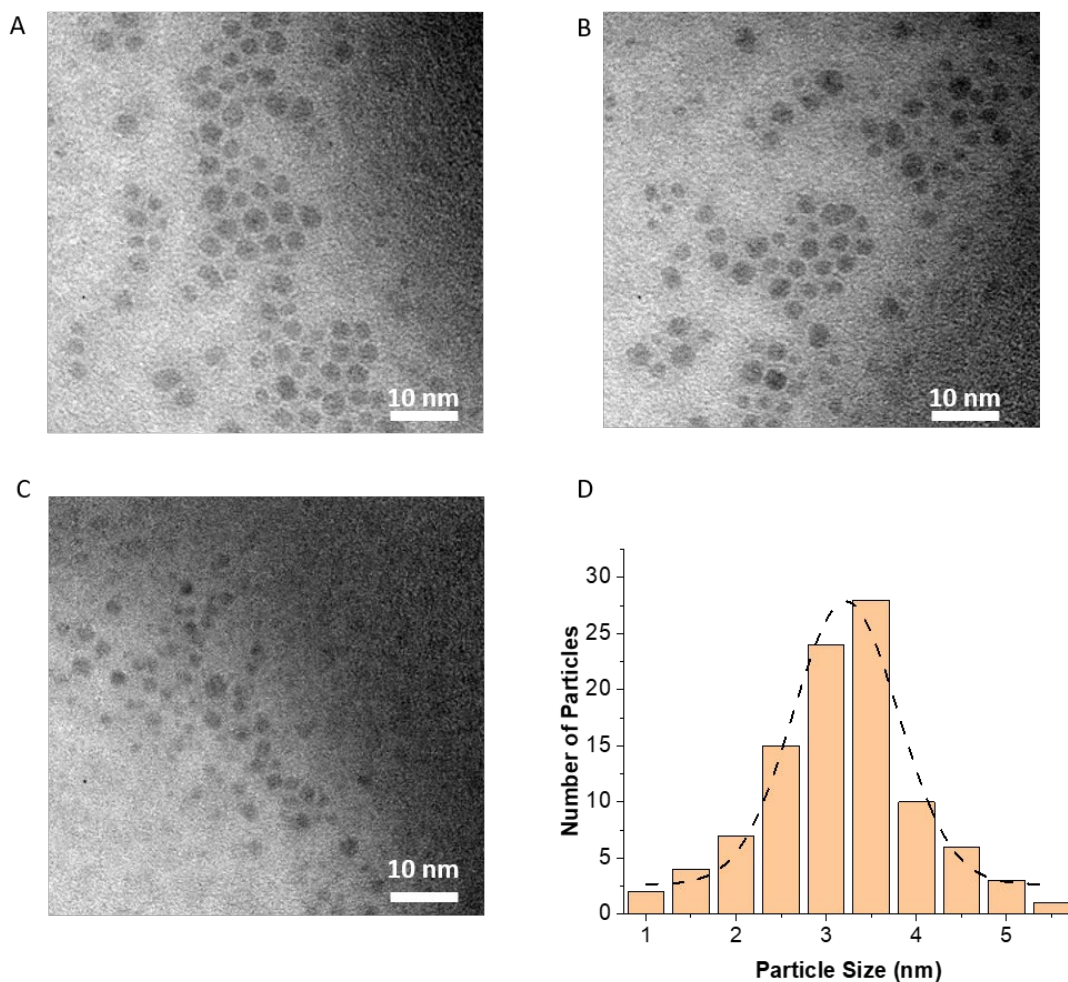
Figure 4.1 High resolution transmission electron microscopy images. (A) MA-PPD2, (B) MA-PPD4, (C) MA-PPD8 and (D) the size distribution of one hundred MA-PPD6 nanoparticles.

Sample Name	Average Nanoparticle Size (nm)
MA-PPD2	3.22±0.57
MA-PPD4	3.16±0.68
MA-PPD6	3.29±0.51
MA-PPD8	3.09±0.93

Table 4.1 Average nanoparticle size obtained by HR-TEM for all MA-PPDx samples
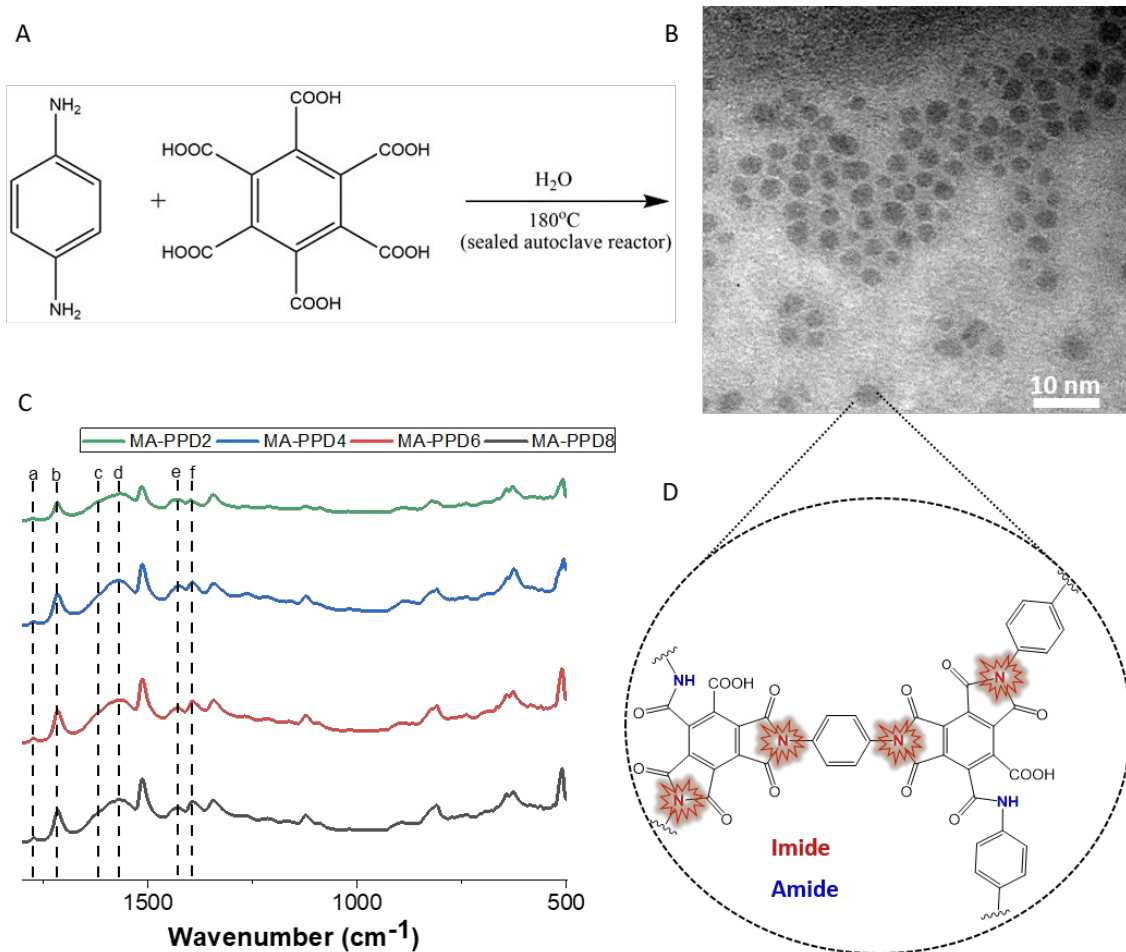
Figure 4.2 Synthesis and characterization of MA-PPD luminophores. (A) Reaction scheme between PPD and mellitic acid; (B) TEM image of MA-PDD6; (C) FT-IR spectra of MA-PPDx; (D) The chemical structure of the MA-PPD luminophores.

Sample Name	Reaction Time (h)	Imide/Amide Relative Content		Lifetime (μs)^a	
		FT-IR	XPS	[O$_2$]= 0%	[O$_2$]= 21%
MA-PPD2	2	0.73±0.04	1.19±0.16	4.506 ± 0.217	2.832 ± 0.081
MA-PPD4	4	1.17±0.08	2.69±0.23	5,812 ± 0,456	3.215 ± 0.412
MA-PPD6	6	1.39±0.09	10.13±0.18	17.067 ± 0.72	5.611 ± 0.289
MA-PPD8	8	1.38±0.05	10.02±0.29	16.379 ± 0.545	5.581 ± 0.447

Table 4.2 Imide/amide relative content and PL lifetime of MA-PPDx luminophores.

To understand the evolution of the functional groups and investigate the time-dependent polyimide formation, I performed FT-IR on my photoemitters. All the peaks observed in MA-PPD2 were preserved as the reaction proceeded up to 8 hours, as shown in Figure 4.2c and summarized in Table 4.2. This result indicates that all types of functional groups are formed within the first two hours. The peak at 1775 cm^{-1} (a) and 1718 cm^{-1} (b), attributed to the symmetric and asymmetric carbonyl (C=O) stretching, showed the successful imide formation. The presence of the peaks corresponding to the C=O stretching of the amide bond and N-H in-plane bending of amide at 1627 cm^{-1} (c) and 1556 cm^{-1} (d) indicates that the final structure is composed of a mixture of imide and amide bonds (Figure 4.2d). To quantify the ratio of imide and amide bonds, I analyze the intensities of the C-N stretching vibrations located at 1422 cm^{-1} (e) and 1385 cm^{-1} (f). The intensities of the C-N stretching vibration peak, characteristic for imides, increased, whereas that of the C-N stretching vibration peak of amides decreased until the reaction time reached 6 hours. Indeed, the relative imide/amide content increased by 90.4% when the reaction time was prolonged from 2 to 6 hours and plateaued thereafter, as shown in Table 4.2 and Table 4.4. This result indicates that the imide formation within MA-PPD nanoparticles is terminated within 6 hours.

Type of the bonds	Mode	MA-PPD2	MA-PPD4	MA-PPD6	MA-PPD8
C=O (amide)	Stretching	1623 cm^{-1}	1625 cm^{-1}	1627 cm^{-1}	1627 cm^{-1}
C-N (imide)	Stretching	1382 cm^{-1}	1384 cm^{-1}	1385 cm^{-1}	1385 cm^{-1}
C-N (amide)	Stretching	1421 cm^{-1}	1423 cm^{-1}	1422 cm^{-1}	1421 cm^{-1}
C=O (imide)	Symmetric stretching	1718 cm^{-1}	1719 cm^{-1}	1718 cm^{-1}	1718 cm^{-1}
C=O (imide)	Asymmetric Stretching	1774 cm^{-1}	1774 cm^{-1}	1775 cm^{-1}	1775 cm^{-1}
N-H (amide)	In-plane bending	1557 cm^{-1}	1558 cm^{-1}	1560 cm^{-1}	1560 cm^{-1}

Table 4.3 Type of the bonds for each MA-PPDx samples obtained by FT-IR

Sample Name	Imide/Amide Ratio				
	Sample 1	Sample 2	Sample 3	Average	Standart Deviation
MA-PPD2	0.69	0.77	0.73	0.73	±0.04
MA-PPD4	1.24	1.19	1.08	1.17	±0.08
MA-PPD6	1.31	1.37	1.49	1.39	±0.09
MA-PPD8	1.39	1.33	1.42	1.38	±0.05

Table 4.4 Imide/Amide relative ratio of MA-PPD2, MA-PPD5, MA-PPD6 and MA-PPD8 obtained by FT-IR (n=3)

To investigate the evolution of the elemental composition of the functional groups in the MA-PPDx samples, I quantified the concentration of each chemical element with XPS. The elemental analysis shows no significant change in the carbon concentration. By contrast, the nitrogen concentration increases from 5.5 % to 11.1%, whereas the oxygen concentration decreases from 31.6% to 25.6% as the reaction proceeds from 2h to 6h (Table 4.5). No significant change was observed at longer reaction times (8h), well in agreement with my FT-IR analysis. The decrease in the elemental oxygen concentration might be due to the loss of hydroxyl (–OH) groups during the imide formation (Figure 4.2d). To combine the elemental composition analysis with the deconvoluted high-resolution XPS, I decomposed the C1s peak into four peaks at 284.4 eV, 285.4 eV, 287.3 eV, and 288.2 eV that I attributed to the sp^2 carbon, C-N group, carbon (amide), and carbon (imide) respectively.[229] To quantify the evolution of imide groups, the N1s peaks were deconvoluted into three main peaks, corresponding to amide (-CONH$_2$/-CONHR/-CONR) (398.9 eV), imide (399.8 eV), and protonated N (401.3 eV) functionalities[227,228]. This analysis reveals an increase in the relative imide/amide ratio from 1.19 to 10.13 as the reaction proceeds from 2 to 6 hours and plateaued thereafter (Table 4.6). These results are in excellent agreement with my FTIR results.

Sample Name	C%	O%	N%
MA-PPD2	62.92	31.63	5.45
MA-PPD4	63.07	29.3	7.62
MA-PPD6	63.14	25.58	11.09
MA-PPD8	63.09	25.67	11.04

Table 4.5 Type of the elements for each MA-PPDx samples obtained by XPS

Sample Name	Imide/Amide Ratio				
	Sample 1	Sample 2	Sample 3	Average	Standart Deviation
MA-PPD2	1.37	1.12	1.08	1.19	±0.16
MA-PPD4	2.55	2.95	2.57	2.69	±0.23
MA-PPD6	10.09	9.97	10.33	10.13	±0.18
MA-PPD8	10.35	9.81	9.9	10.02	±0.29

Table 4.6 Imide/Amide relative ratio of MA-PPD2, MA-PPD4, MA-PPD6 and MA-PPD8 obtained by XPS (n=3)

4.4.2 *Optical Characterization of MA-PPD photoemitters*

To investigate the effect of imide formation on the photoluminescence behavior, I recorded the photoluminescence spectra of MA-PPDx samples dispersed in aqueous solutions. I limited my characterization to samples synthesized during 2-6 hours because I did not observe any significant difference in their composition thereafter any more. I did not observe any significant positional change in the photoluminescence spectra (λ_{exc}= 585 nm, λ_{em}= 609 nm) when samples were excited between 280-600 nm, as shown in Figure 4.3a-c. If excited at the wavelength of λ_{ex}= 585 nm, the spectra of aqueous solutions displayed a red emissive behavior, consistent with other polyimide luminophores[224,230]. The charge-transfer (CT) interaction between electron-donating amines and electron-accepting carboxyl has been re-

ported to lower the energy gap between the excited and ground state, resulting in red photoemission. It is noteworthy that, while the position of the emission peak is preserved, the photoluminescence (PL) intensity increased from 332,311 (u.a) to 1,002,938 (u.a) as the reaction proceeds from 2 h to 6 h. This result suggests that the increase in PL intensity of MA-PPD is related to the new imide groups that form at longer reaction times.
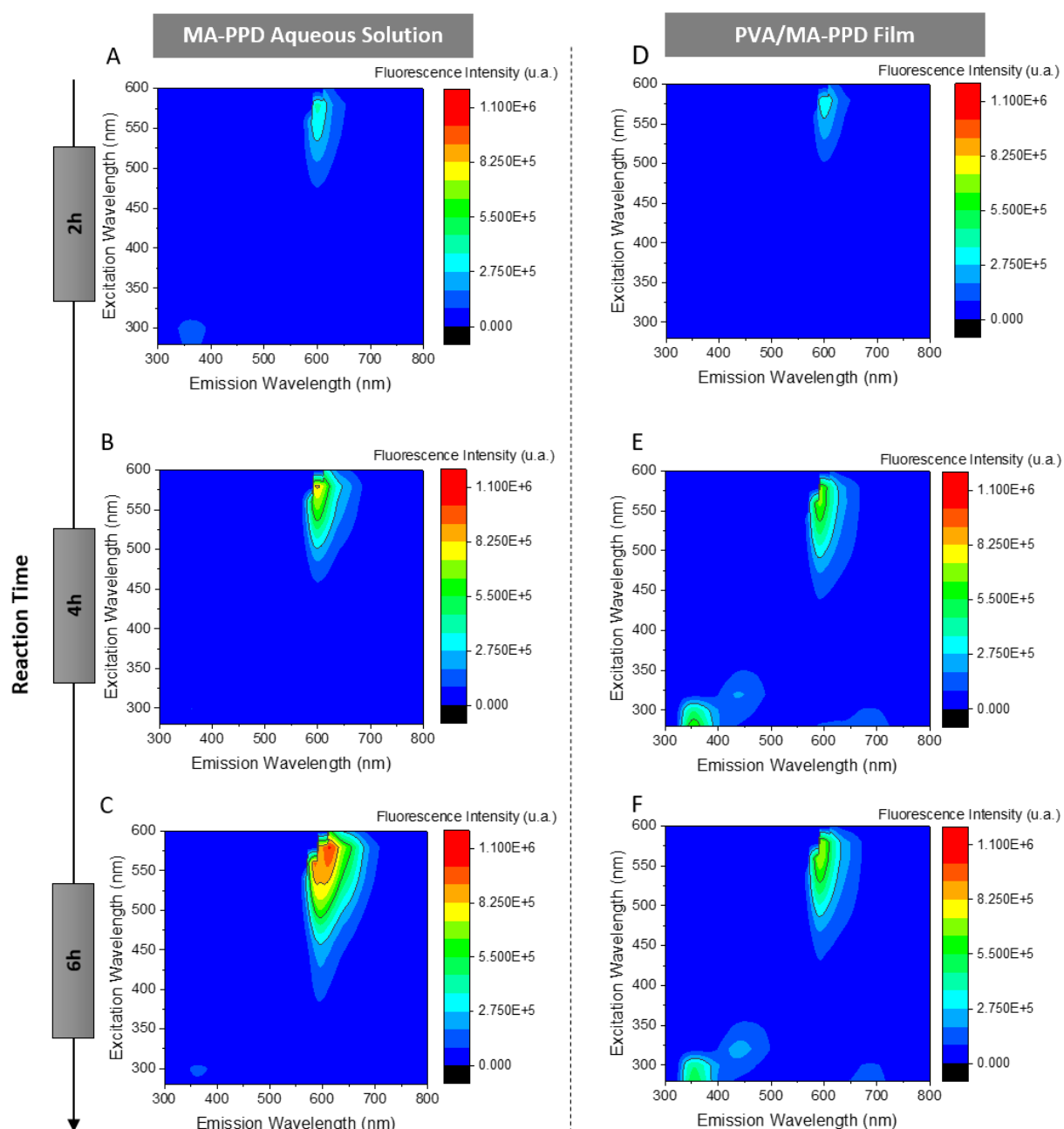
Figure 4.3 Photoluminescence contour plots of MA-PPDx as a function of their synthesis time (x = 2, 4, or 6 h). (A-C) MA-PPDx in aqueous solutions. (D-F) MA-PPDx embedded in PVA films.

To understand the effect of the microenvironment on the optical properties of MA-PPD, I recorded the photoluminescence spectra of MA-PPD nanoparticles embedded within a high molecular weight PVA matrix (Figure 4.3 d-f). Compared to MA-PPD in aqueous solutions (λ_{em}= 609 nm), slightly blue-shifted emissive states (λ_{em}= 597 nm) were observed when excited at 570 nm. The blue shift has been observed in a similar system where luminophores synthesized by phenylenediamine were encapsulated within a PVA matrix. This behavior was ascribed to the absence of the solvent-relaxation effect[231]. Similar to MA-PPD dispersed in aqueous solutions, I did not identify any significant positional shift of the emissive peaks from MA-PPDx (x = 2, 4, or 6) nanoparticles if embedded in PVA films (Figure 4.3 d-f). This result demonstrates that the interaction between the polyimide groups of MA-PPD photoemitters with water and the PVA matrix has negligible effects on the intrinsic optical properties and chemical structure of MA-PPD nanoparticles.

4.4.3 O_2 Sensing Performance

The key characteristic of O_2 sensors is their O_2-dependent photoluminescence. To quantify this parameter, I dispersed MA-PPD in an aqueous solution or embedded them in a PVA film and recorded their photoluminescence spectra at oxygen concentrations of 0% and 21%. Aqueous solutions of MA-PPD nanoparticles did not show any O_2 concentration-dependent photoluminescence, as shown in Figure 4.4. By contrast, MA-PPD nanoparticles embedded in a PVA film displayed a strongly increased PL intensity with decreasing oxygen concentration. To quantify this increase, I determined the ratio between the PL intensity at 0% and 21% O_2 concentration as $I_{0\%}/I_{21\%}$. For PVA/MA-PPD2, PVA/MA-PPD4, PVA/MA-PPD6 and PVA/MA-PPD8 samples, $I_{0\%}/I_{21\%}$ was 1.84, 2.37, 3.39 and 3.27 respectively (Figure 4.5a). Such a clear O_2 dependent photoluminescence might be due to the strong intermolecular interactions between embedded nanoparticles and the polymer matrix, which barely affects the MA-PPD chemical structure but eliminates the non-radiative triplet-singlet ground state recombination. These results demonstrate the advantage of embedding MA-PPD nanoparticles in a PVA matrix if they are used as O_2 sensors.
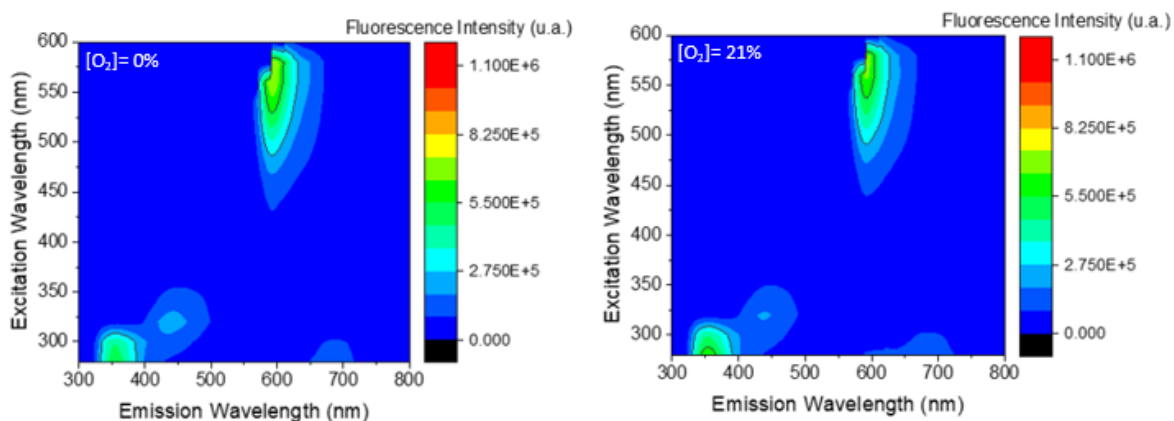
Figure 4.4 Fluorescence contour plot of MA-PPD6 nanoparticles in aqueous solution at $[O_2]$= 0% and $[O_2]$= 21%.

My results indicate that MA-PPD-containing PVA matrices are excellent O_2 sensors. To understand the O_2 sensing mechanism, I quantify the PL lifetime as a function of the O_2 concentration within a range of 0-21% O_2, as summarized in Table 4.2. At 21% O_2, all samples exhibit room-temperature phosphorescence (RTP) with a lifetime value (τ) of a few microseconds. The short phosphorescence lifetime indicates the presence of an efficient RTP mechanism, as previously shown.[221] Based on these results, I quantified the PL lifetime ratio $\tau_{0\%}/\tau_{21\%}$, where $\tau_{0\%}$ and $\tau_{21\%}$ indicate the PL lifetime measured at 0% and 21% O_2, respectively. This ratio was 1.59, 1.81, 3.04, and 2.93 for PVA/MA-PPD2, PVA/MA-PPD4, PVA/MA-PPD6, and PVA/MA-PPD8 sensors, respectively. Note that the lifetime ratios of the last two samples are very similar, in good agreement with my FTIR results, confirming that the composition of MA-PPD remains unchanged when the synthesis time exceeds 6h. Combining this result with those of the FT-IR and XPS analysis, I note that within the first 6 hours of reaction time, the O_2 response of MA-PPD increases with its formation time and plateaus thereafter. This increased efficiency can be attributed to the increased conformational rigidity of MA-PPD nanoparticles that eliminates non-radiative recombinations, thereby enabling efficient O_2 RTP quenching.
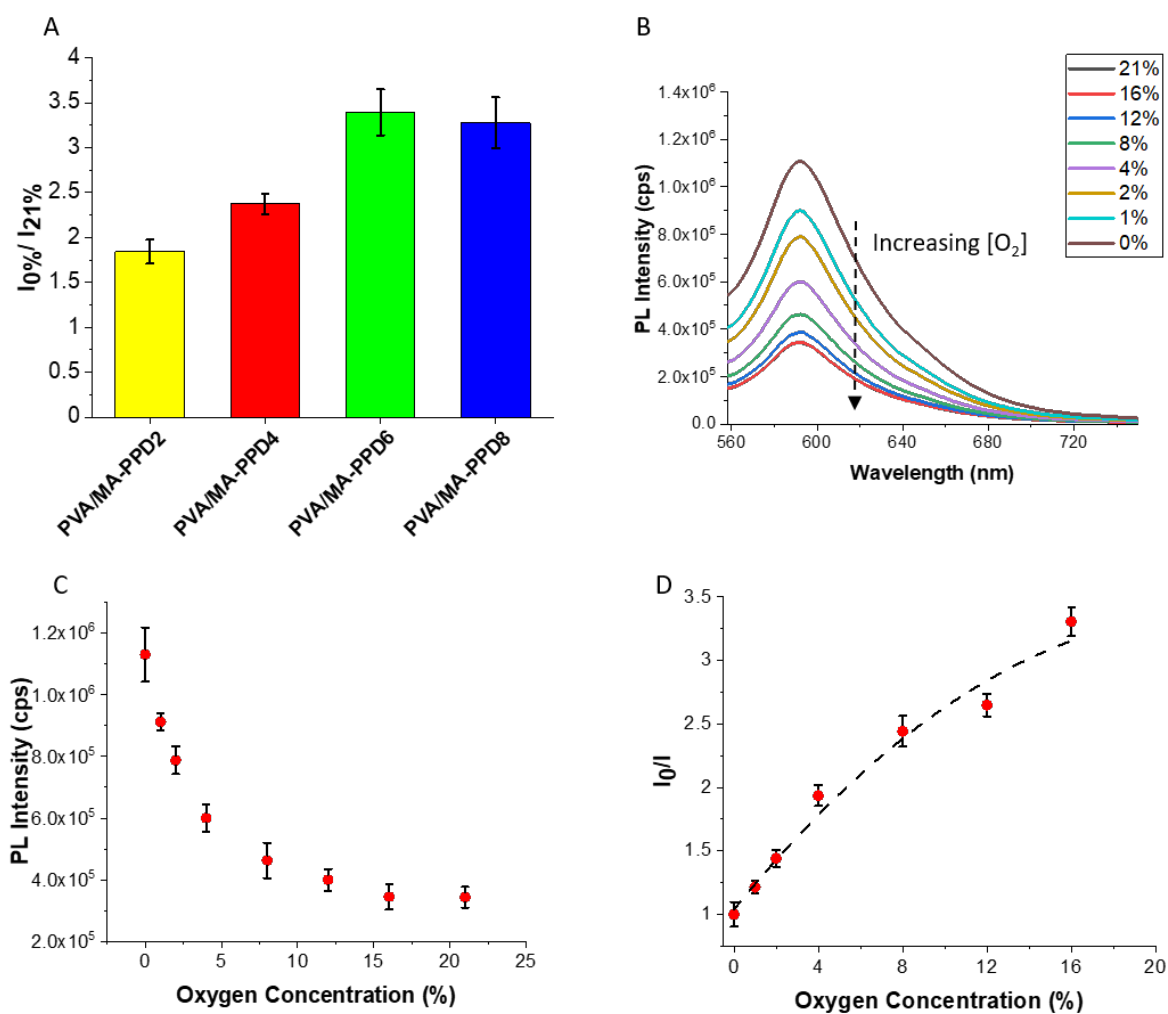
Figure 4.5 Oxygen sensing performance of PVA/MA-PPD sensors. (A) Relative PL intensity of PVA/MA-PPDx sensors between 0% and 21% O_2; (B) PL spectra of PVA/MA-PPD6 sensor at different O_2 concentrations; (C) Maximum PL intensity of PVA/MA-PPD6 sensor at different O_2 concentrations; (D) Stern-Volmer Plot of PVA/MA-PPD6 sensor.

Oxygen Conc (%)	Maximum PL intensity (cps)				
	Sample 1	Sample 2	Sample 3	Average	Standart Deviation
0	1030334	1199532	1162084	1130650	±88871.05
1	903942	944562	886410	911638,66	±29830.1
2	779423	748328	835427	787726,33	±44139.14
4	576473	650432	574619	600508,33	±43245.39
8	479923	502822	406231	462992	±50472.26
12	362232	431222	407359	400271	±35036.91
16	372832	365437	297769	345346,33	±41368.46
21	381232	332942	316410	343528	±33682.64

Table 4.7 Maximum PL intensity (cps) of three different MA-PPD6/PVA films and its standard deviation
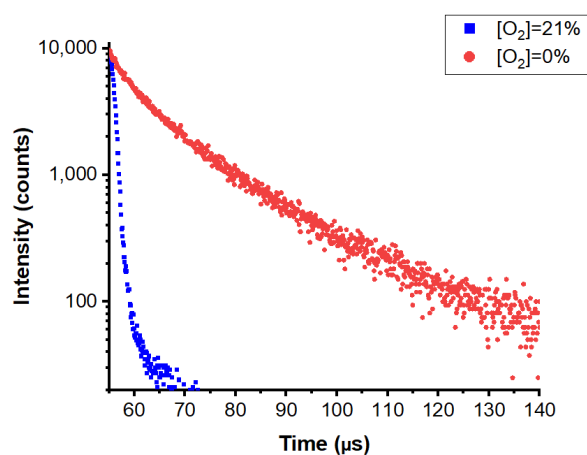
Figure 4.6 Lifetime decay curve of MA-PPD6 nanoparticles embedded in PVA film at $[O_2]$= 0% and $[O_2]$= 21%.

To quantify the O_2 sensing performance, I analyzed the chemically most stable and performing sample, namely PVA/MA-PPD6. I measured the emission spectra within an O_2 concentration range of 0-21%, as shown in Figure 4.5b. The emissive state of MA-PPD6 was quenched until the O_2 concentration reached 16%, as shown in Figure 4.5c, indicating

that my sensors can be used within this O_2 range. Note that the O_2 sensing range has previously been much narrower: similar systems could only detect O_2 in the range of 0-8%[222]. I assign my sensor's broader O2 sensing range (0-16%) to the efficient RTP mechanism that shortens the phosphorescence lifetime, thereby enabling O_2 quenching at higher O_2 concentrations[220].

To quantify the sensitivity, I fitted the Stern-Volmer plot to a first-order polynomial function between 0-4% O_2 (R^2 = 0.998, Figure 4.7b). The excellent quality of the fits indicates that my sensors display a linear response to the O_2 concentration up to 4%. It has been previously discussed that the linear calibration curve is desirable for simple one-point instrument calibrations that enable the use of the standard calibration cards for the sensors.[232] The Stern-Volmer quenching constant was calculated in accordance with the Stern-Volmer Equation.

$$I_0/I = 1 + K_{sv}.[O_2]$$

Where I_0 and I represent the luminescence intensities in the absence and presence of O_2, respectively. K_{sv} is the Stern-Volmer quenching constant, and $[O_2]$ is the oxygen concentration in the environment. The Stern-Volmer constant (K_{sv}) was calculated to be 0.2351 kPa^{-1} for the linear response range of 0-4% O_2. It is also noteworthy that, within a broader range of O_2 concentration (0-21%), instead of linear fitting, the second-order polynomial function fits the data well (R^2 = 0.986, Figure 4.7a), indicating a non-linear response above 4% O_2. This behavior could be attributed to the inhomogeneity of the microenvironment in the polymer film.[233]
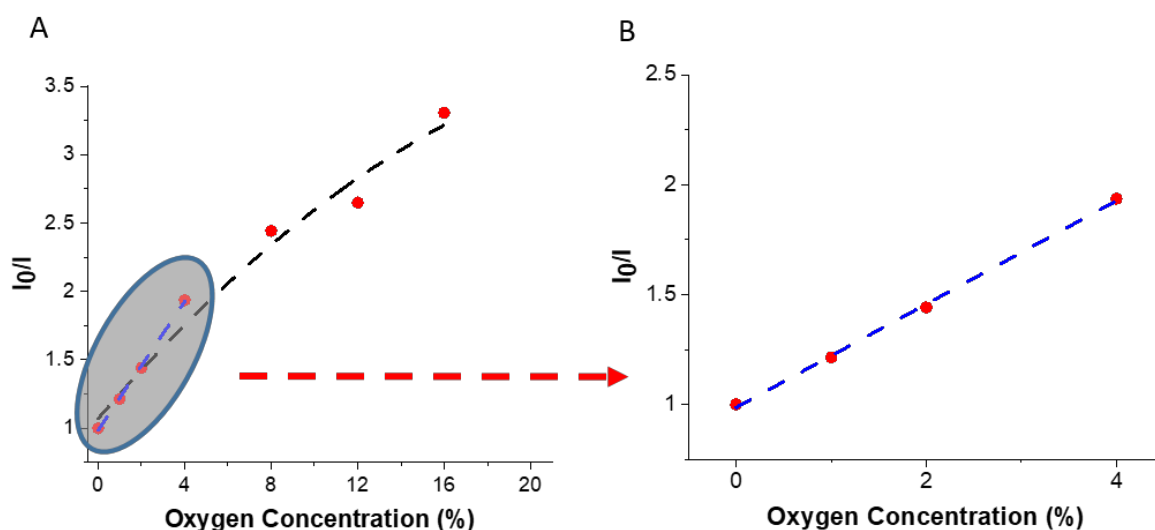
Figure 4.7. Stern-Volmer fitting of RTP quenching. (A) Fitting in the linear quenching region (0-4% O_2) and non-linear quenching region (4-16% O_2); (B) Zoomed in version of linear quenching region (0-4% O_2).

Figure 4.7-Note

Second-order Polynomial Fitting with Equation 1 was used for the range of 0-21% O_2, and the fitting result is given in the table.

$$f(x) = Ax^2 + Bx + C \quad \text{(Equation 1)}$$

	Value	Standart Error
Intercept (C)	1.07	0.119
A	0.183	0.054
B	-0.003	0.003
R-square	0.986	

First-order Polynomial Fitting with Equation 2 was used for the range of 0-4% O_2, and the fitting result is given in the table:

$$f(x) = Ax + B \quad \text{(Equation 2)}$$

	Value	Standart Error
Intercept (B)	0.986	0.013
Slope (A)	0.235	0.005
R-square		0.998

The usefulness of O_2 sensors strongly depends on their ability to repetitively sense O_2 without significant losses in sensitivity. To assess the reversibility of my O_2 sensors, I cycled the O_2 concentration between 0% and 4% for 10 times, as shown in Figure 4.8a, and similarly between 0% and 21% also for 10 times, as shown in Figure 4.8b. I did not observe any significant decay in the sensitivity, indicating that no noticeable photo-oxidation processes occur within 10 cycles due to the great photo and chemical stability of the polyimide network.
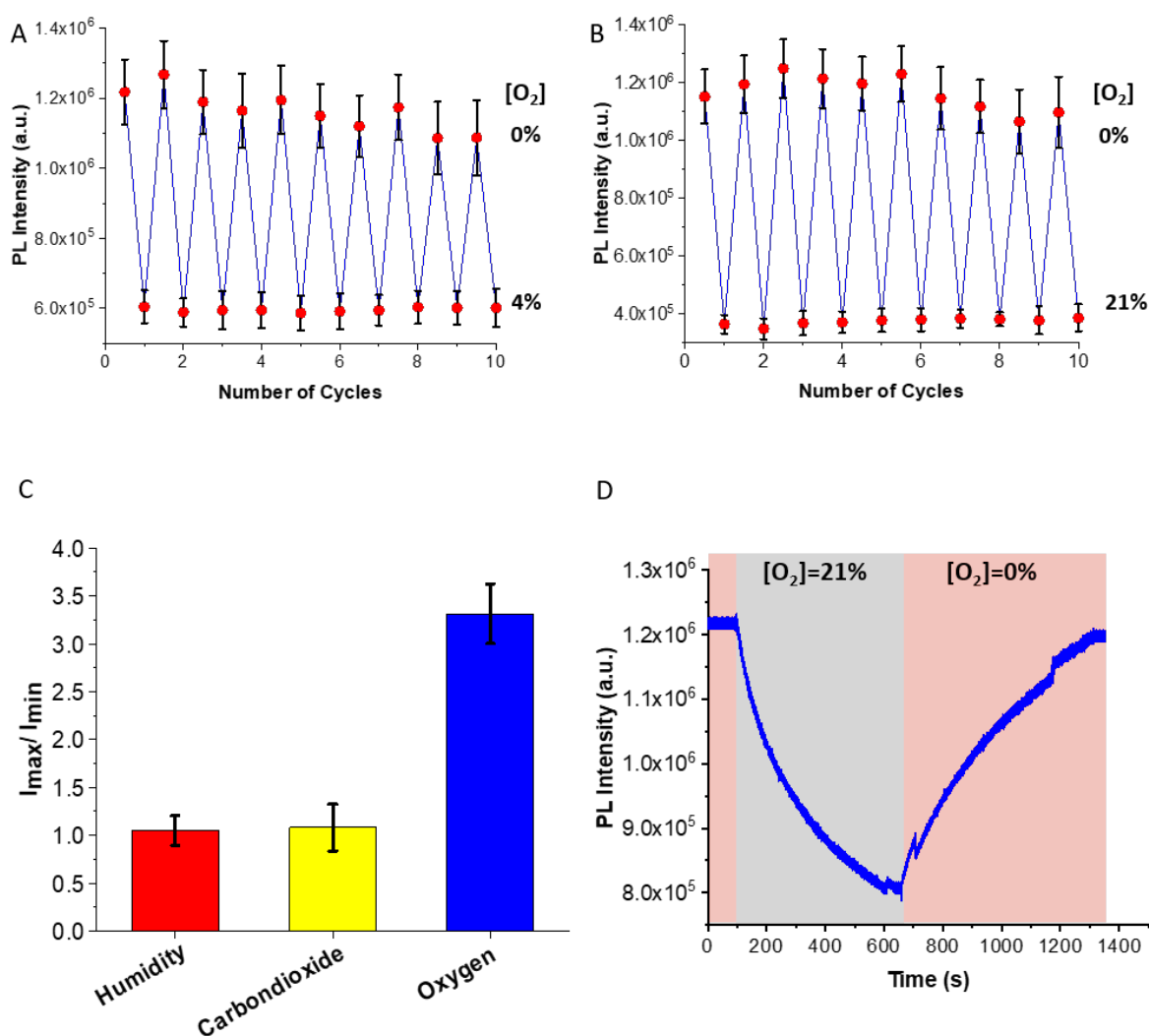
Figure 4.8 O$_2$ sensing features of PVA/MA-PPD6 sensor. (A-B) Sensing reversibility of PVA/MA-PPD6 sensor exposed to 10 concentration cycles of 0 - 4% or 0 - 21% O$_2$; (C) Sensing cross-interference of humidity and CO$_2$ towards O$_2$; (D) time-dependent sensing response to a 0-21-0% O$_2$ cycle.
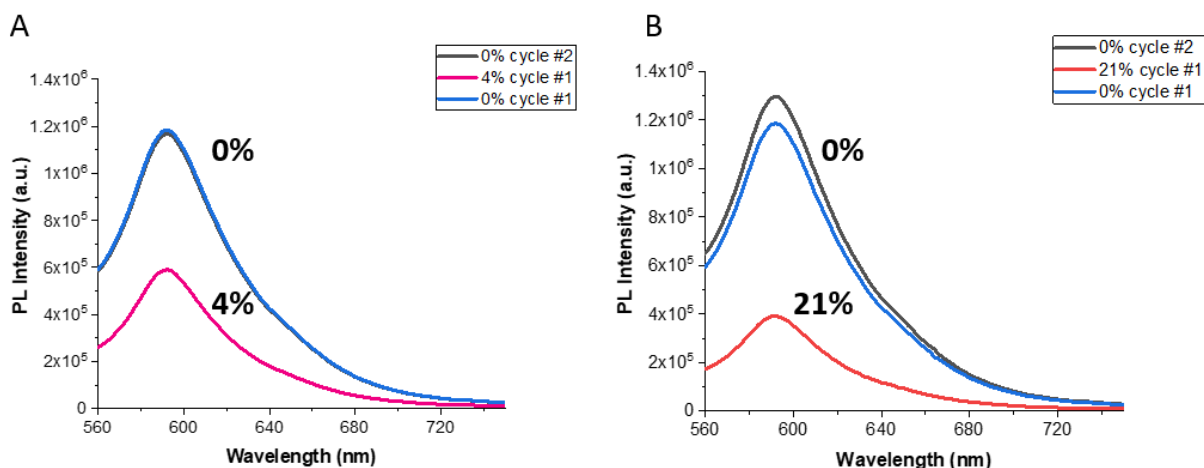
Figure 4.9 Representative PL spectra for reversibility test within the range of (A) 0-4 O$_2$ and (B) 0-21% O$_2$.

The reliability of the O$_2$ sensors is crucial for developing marketable sensors. To assess the reproducibility of our O$_2$ sensors, we measured the sensor-to-sensor reproducibility with five different sensors fabricated under the same experimental conditions. The variation of $I_{0\%}/I_{21\%}$ of fabricated sensors was less than 2% (Figure 4.10a). Indeed, this variation of the PL intensity is statistically insignificant. Batch-to-batch reproducibility was assessed by characterizing five batches containing five different sensors for each batch. The maximum deviation of $I_{0\%}/I_{21\%}$ between different batches was 9.8% (Figure 4.10b). These results indicate that the PVA/MA-PPD6 sensor possesses the best sensor-to-sensor reproducibility, shown in Figure S10A. This good reproducibility enables the operation of our sensors in batch calibration mode.
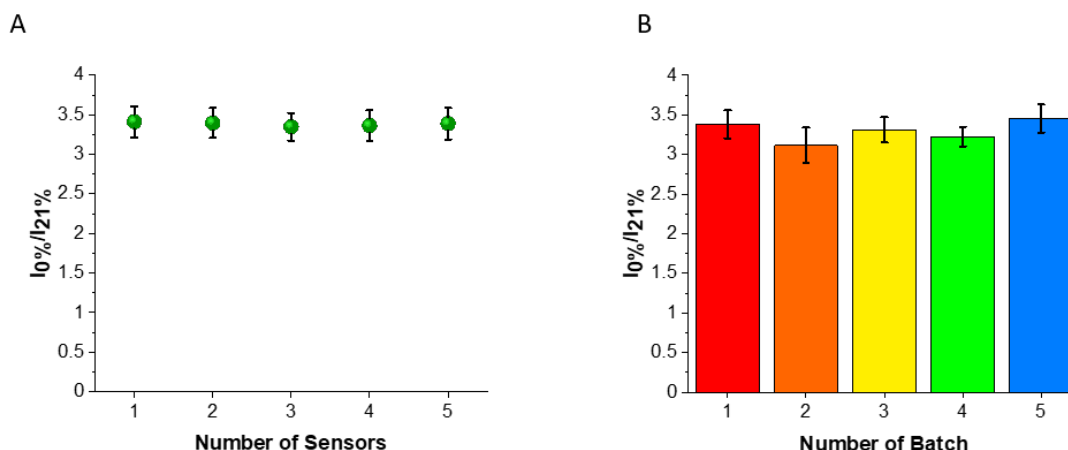
Figure 4.10 Sensor Reproducibility of the PVA/MA-PPD6 sensor. (A) Sensor to sensor reproducibility of 5 sensors fabricated under the same experimental condition; (B) Batch to batch Reproducibility of 5 batches obtained from the average PL intensity change ($I_{0\%}/I_{21\%}$) of 5 different sensors.

O_2 sensors are only truly useful if they also operate in the presence of other types of gases. To test the influence of other atmospheric parameters such as humidity and CO_2, we quantify the sensing performance of our sensors in the presence of 20% and 80% relative humidity, or in the presence of 0% and 60% CO_2, as shown in Figure 4.8c. We did not observe any significant PL response of the MA-PPD6 sensor to humidity or CO_2, as revealed by the ratio between the maximum and minimum PL intensity ($I_{max}/I_{min}\sim1$) when changing the humidity or CO_2 within the range of 20-80% relative humidity and 0-60% CO_2, respectively. This result indicates that cross-interferences between O_2 and humidity or CO_2 can be neglected in our PVA/MA-PPD6 sensors.

The temperature dependence of my O_2 sensor shows a slight positive slope as temperature increases (Figure 4.11a). For the linear response range (0-4% O_2), the temperature-dependent Stern-Volmer constant change ($\Delta K_{sv}/\Delta T$) was found to be 0.0077 kPa^{-1} °C^{-1} for the temperature range of 5-30°C (Figure 4.11b). The constant value enables the simple correction for the sensor calibration at different temperatures. The increase in O_2 sensitivity with respect to temperature can be attributed to several reasons, including 1) the solubility of oxygen in the PVA matrix, 2) the diffusion rate of oxygen into the PVA matrix, and 3) the dynamic quenching constant.[234]
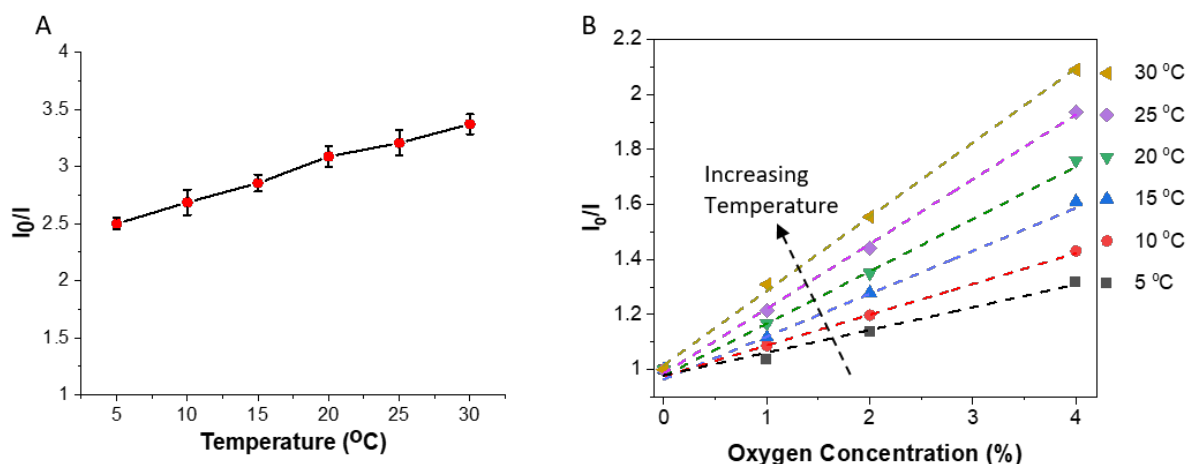
Figure 4.11 Temperature dependence of O$_2$ sensitivity of MA-PPD6/PVA at the range of (A) 0-4 O$_2$ and (B) 0-21% O$_2$.

To test the speed of the sensor to O$_2$ concentration change, the response time of the PVA/MA-PPD6 sensors was measured within one cycle of 0%-21%-0% O$_2$. Upon exposure to 20% O$_2$, the time required to reduce the PL intensity by 95% (Δt_{95min}) was 427 seconds, as shown in Figure 4.8d. The long response time is due to the low oxygen permeability of the PVA matrix and significant film thickness (~100 μm) that hinders O$_2$ molecules from reaching the photoemitters.[235] Although the long response time limits the application area of my sensors, I believe that the continuous, broad-range and reversible sensing make the purely organic O$_2$ sensors promising for the detection of O$_2$, for example, in packaged food where fast response times are not critical.

4.5   Conclusion

A purely organic rigid optical O_2 sensor was developed by embedding polyimide-based nanoparticles within a high-molecular-weight PVA matrix. My results indicate that the sensitivity of the composite strongly depends on the concentration of the imides present in the photoemitters and increases with increasing reaction time. If the photoemitters are embedded in a PVA matrix, they strongly interact with it, thereby limiting the non-radiative recombination, such that their photoluminescence is efficiently RTP quenched by O_2 molecules. The PVA/MA-PPD6 sensors can monitor O_2 in a broad range up to concentrations of 16% with a linear response between 0% and 4% O_2 and non-linear response between 4% and 16% O_2. Moreover, such sensors are resistant to photobleaching and atmospheric inference, making them promising materials for detecting O_2 in the field of food packaging.

Chapter 5

Hydrogel Based Optical Oxygen Fiber Sensor via Phosphorescence Quenching by O_2 molecules

5.1 Abstract

The continuous, non-destructive and fast monitoring of O_2 molecules has become of increasing interest in a wide variety of application areas, for example, packaged food monitoring, biosensing, biomonitoring, and environmental studies. However, a high level of toxicity of conventional optical O_2 sensors creates a need for replacing their sensing unit with organic components. In the previous chapter, I found out that integrating the organic sensing materials into thick and oxygen impermeable polymer film hinders the O_2 diffusion through the center of the matrix, however, resulting in a limited O_2 sensitivity range (0-16% O_2) and slow response rate of the O_2 sensor. Therefore, I hereby developed new organic optical O_2 sensors by embedding polyimide-based photoemitters within a wet-spun PVA hydrogel fiber. The PVA hydrogels show no significant change in gel strength after the photoemitters are embedded into the gel network. The PVA hydrogel fibers have been fabricated with various fiber diameters by the microfluidic wet-spinning technique. Each PVA hydrogel fiber has been tested with regard to different oxygen concentrations (0-21% O_2). The O_2 sensor with polyimide-based photoemitters embedded in the hydrogel fiber exhibits continuous and broad-range O_2 sensing in the range of 0-21% O_2 due to the high oxygen permeability of PVA hydrogel. The O_2 sensitivity strongly depends on the fiber diameter, decreasing with increasing PVA hydrogel fiber diameter.

Moreover, the response time of each hydrogel fiber was investigated to understand the effect of the surface-to-volume ratio on the O_2 diffusion rate. I reduced the response time by half (Δt=89s to Δt=41s) simply decreasing the hydrogel fiber diameter (d_{fiber}=605µm to d_{fiber}=243µm). In this chapter, to my best knowledge, the impact of surface-to-volume ratio and O_2 permeability of hydrogel matrix on O_2 sensing performance of purely optical oxygen fiber has been investigated for the first time in the literature. The metal-free formulation, physiological O_2 sensitivity range (0-21% O_2), and relatively fast response time are appealing features, especially for integrated biomonitoring or biosensing applications.

5.2 Introduction

The ubiquitous oxygen molecule plays a critical role in most biological activities, such as cell respiration and food deterioration, to name a few[237-240]. Different techniques have been developed for the sensing of oxygen molecules in a gas or liquid medium[240,241]. The optical oxygen sensor is one of these techniques based on fluorescence or phosphorescence quenching by oxygen molecules. Optical oxygen sensors offer many advantages over the other types of oxygen sensors, such as i) no consumption of analytes, ii) real-time monitoring, iii) low signal drift, iv) high reversibility, and v) long shelf-life [241]. Optical oxygen sensors have been developed to overcome the limitations of the electrochemical oxygen sensor, destructive monitoring, and consumption of analytes, and are widely used, for example, as chemical[241-243], biological[244,245], and environmental[246] sensors.

Optical oxygen sensors consist of two main components in the fabricated sensors: An analyte sensitive sensing unit and an organic/inorganic support matrix. For the luminescence quenching caused by oxygen, the emission intensity or lifetime decay of the sensing unit is a function of the oxygen concentration. The dynamic quenching between luminophores and oxygen molecules was first explained by Stern and Volmer in 1919[247]. The Stern-Volmer quenching constant, which determines the limit of detection of an optical sensor, was calculated following the Stern-Volmer Equation;

$$I_0/I = 1 + K_{sv}.[O_2] \tag{1}$$

where I_0 and I represent the luminescence intensities in the absence and presence of O_2, respectively. K_{sv} is the Stern-Volmer quenching constant, and $[O_2]$ is the oxygen concentration in the environment. This equation can be fitted to the intensity or lifetime values of the luminophores. The fitted curve can be used as the calibration curve of the optical oxygen sensor.

The response rate of optical oxygen sensors strongly correlates with the diffusion kinetics of oxygen molecules between the environment and the support matrix. Traditionally, the optical oxygen sensors are prepared by casting solution mixture onto a carrier medium, resulting in a polymer film. The diffusion kinetics highly depends on the thickness of the polymer film. Because the O_2 diffusion within the polymer films is slower than in air, thicker

polymer films lead to a slower response rate of the O_2 sensor[248]. The response rate can only be increased by decreasing the thickness of the polymer matrix, however, at the expense of the signal-to-noise ratio. Thus, the optimized polymer film thickness is determined by the trade-off between the luminescence intensity and sensitivity of the sensor such that the response time of optical oxygen sensors is typically below a few minutes. Optic fibers have emerged as optical oxygen sensors in the last decade to enhance the O_2 sensitivity and sensor response time due to their higher surface-to-volume ratio[249]. O_2 fiber sensors were first produced by using a mixture of polystyrene and an Eu(III) complex as feeding electrospinning solution[250]. High sensitivity (I_0/I_{100} = 15.56), promising linear Stern–Volmer characteristics, and short response/recovery times ($t\downarrow$ of 7 s and $t\uparrow$ (s) of 14 s) were obtained. A noteworthy improvement of the response time and sensitivity to O_2 was later achieved for Cu(I)[251], Ir(III)[252], or Eu(III)[251,253] complexes due to the efficient SOC of a heavy metal ion. However, the high-level toxicity of such metal ions hampers the use of these sensors in a wide variety of application areas. Therefore, organic sensor materials have been integrated into polymer fibers to overcome the toxicity issue. To my best knowledge, no study investigates the full O_2 sensing performance of purely organic luminophores integrated into polymeric optical fibers.

Microfluidic wet-spinning is a wet-spinning process that confines the polymer and coagulant solutions within co-axial laminar flows. This process enables reasonable control of the diffusion interface between two laminar flows, resulting in the solidification of polymer solution in a controlled manner[254]. In addition, microfluidic wet-spinning offers an advantage of a mild spinning condition that enables the spinning of natural polymer without using any harsh solvents[255]. Various hydrogel fibers, such as alginate, collagen, and chitosan, can be fabricated using microfluidic spinning, resulting from the co-axial laminar flow of core (pre-polymer solution) and sheath fluids (crosslinking agents)[256–259]. Microfluidic wet-spinning offers several morphological advantages, such as high porosity and large pore size, which play a critical role in O_2 diffusion through the polymer matrix[260,261]

In the previous chapter, I showed the polyimide-based photoemitters embedded in a high molecular weight poly(vinyl alcohol) (PVA) matrix that quenches their fluorescence within the range of 0-16% O_2[262]. However, the long response time (~7.5 min) has hampered their further use. The long response time is due to the low oxygen permeability of the PVA matrix and significant film thickness (~100 µm) that hinders O_2 molecules from

quickly reaching the photoemitters. To address this limitation, in this chapter, I embedded polyimide-based photoemitters into PVA hydrogels using the microfluidic wet-spinning technique. The resulting O_2 sensor can reversibly detect O_2 molecules in the range of 0-21% O_2 with a linear calibration curve. Notably, the response time was significantly enhanced by embedding the photoemitters into polymer hydrogel fibers (t= 41s) due to high O_2 permeability and surface-to-volume ratio.

5.3 Experimental

5.3.1 Materials

P-phenylenediamine (PPD) (≥99%) and mellitic acid (MA) (≥99%) were purchased from Sigma-Aldrich (St. Louis, MO, USA) and Tokyo Chemical Industry (Tokyo, Japan), respectively, for the synthesis of luminophores. Ultra-pure water (Milli-Q) was used as a solvent for the reactions. Potassium Bromide (KBr) was obtained from Merck (Darmstad, Germany) for the pellet preparation. Norbornene-functionalized polyvinyl alcohol (nPVA) was synthesized as previously reported[263]. 1,4-Dithiothretiol (≥97%) and α-Hydroxy-4-(2-hydroxyethoxy)-α-methylpropiophenon (Irgacure 2959) (98%) were purchased from Sigma-Aldrich (St. Louis, MO, USA). Oxygen (O_2) (99.99%), nitrogen (N_2) (99.8%), and carbon dioxide (CO_2) (99.99%) were purchased from Carbagas (Zurich, Switzerland) for the sensor performance studies.

5.3.2 Synthesis of the Luminophore

A PPD and MA precursor mixture (1 mg/mL) was prepared in a 3:1 molar ratio in ultra-pure water. The prepared mixture solution was vigorously stirred for 30 minutes at room temperature. Subsequently, the solution was transferred to a polytetrafluoroethylene (PTFE) lined synthesis autoclave reactor (Parr Instrument, Acid Digestion Vessel) with a volume of 50 mL. The autoclave reactor was placed in a pre-heated oven (Series ED Avantgarde Line, BINDER, Spain) at 180 °C for different reaction times. The products, MA-PPDx, were then dried in a freeze-dryer (Alpha 3-4 LSC basic, Martin Christ, Germany) for 24 hours, resulting in MA-PPDx, where MA, PPD, and x represent mellitic acid, para-phenylenediamine, and reaction time (in hours), respectively.

5.3.3 Preparation of Pre-Polymer Solution

Gel precursors were prepared by dissolving 10% nPVA precursor in 0.005% Irgacure 2959 and various MA-PPD luminophore concentrations (0.01%, 0.05%, and 0.1%), subsequently adding DTT crosslinker solution until a thiol-to-ene stoichiometric ratio reaches 4:10 in distilled water. Then, the as-prepared solution was kept in the dark environment to protect from light irradiation.

5.3.4 Characterization of the Luminophore and Hydrogel

Fourier Transform Infrared (FT-IR) spectra were obtained with a Varian-640-IR (Portmann Instruments GmbH, Biel-Banken, Switzerland) operated in the wavenumber range of 400-4000 cm^{-1} with 2 cm^{-1} spectral resolution. The pellets were prepared by mixing 0.05% w/w KBr into MA-PPDx powder for the quantitative FT-IR analysis.

The photoluminescence (PL) of MA-PPDx luminophores in an aqueous medium or a polymer matrix were measured with a Horiba Jobin Yvon FluoroMax-4 (Horiba Jobin Yvon GmbH, Bensheim, Germany). To determine the concentration for the highest PL intensity, a concentration series of 0.005%, 0.01%, 0.02%, 0.03%, 0.05%, 0.1%, 0.2% and 0.5% (w:v) was used for all MA-PPDx. The excitation range of 280-600 nm and emission range of 300-800 nm were used with the slit width of 3 nm.

The lifetime of all MA-PPDx was quantified with a Horiba DeltaPro (Horiba Jobin Yvon GmbH, Bensheim, Germany) at the excitation wavelength of 510 nm. LUDOX solution was used to calculate the instrument response factor (IRF).

For the mechanical analysis of hydrogels, in-situ photo-rheometry (Anton-Paar, MCR 301) was used to monitor the hydrogel formation after UV radiation (10 mW/cm^2) at 25 $^\circ$C, gap thickness of 500 µm, a shear strain of 1% and frequency of 1Hz. Time-sweep of storage modulus (G$'$) and loss modulus (G$''$) were collected until G$'$ reaches a plateau. For the amplitude sweep test, the gap thickness and frequency were kept at 500 µm and 1 Hz, respectively. The shear strain increased from 0.1% to 100%. For the frequency sweep test, the gap thickness and shear strain were kept constant at 500 µm and 1%, whereas the frequency changed from 0.05 Hz to 100 Hz. AFM studies were performed with Nanosurf Ambient AFM variant (Flex-AFM) by utilizing AFM probe of Olympus cantilever (OMCL-TR400PSA-3) with spring constants of 0.08 N/m, resonant frequency of 34 kHz, and tip radius of 15 nm.

5.3.5 Microfluidic Wet-Spinning of nPVA/MA-PPD6 fibers

For the microfluidic spinning process, as-prepared gel precursors containing nPVA, Irgacure2959, DTT, and MA-PPD6, were used as core flow. The 2 wt% alginate solution was prepared for the sheath flow as a protection layer. The core and sheath fluids were loaded into 2 mL syringes (Injekt Bbraun). Subsequently, loaded syringes were connected to three microfluidic syringe pumps (neMESYS 290N, Cetoni, Germany). The connected syringes were then attached to a Y-shaped microfluidic PDMS chip using blunt needle (STE-RICAN, 18G). The core and sheath solution were simultaneously introduced into a Y-shaped microfluidic chip at increasing core-to-sheath flow ratio (Q_{core}:Q_{sheath}) from 1:9 to 9:1 with the total flowrate of 200 µL/min. The core and sheath flows were collected at 0.7 wt% $CaCl_2$ solution for the coagulation of alginate solution. Subsequently, as-prepared fibers were kept under 365 nm UV radiation for 5 minutes for the curing of core solution, containing gel precursors. Finally, the protection layer, coagulated alginate, was soaked at 25% NaCl solution for the shell removal. As-prepared core fibers were kept in distilled water for further analysis.

5.3.6 The O_2 sensing performance of the nPVA/MA-PPD6 fibers

To test the oxygen sensitivity, a custom-built environmental chamber located in the spectrofluorometer chamber was purged with an O_2/N_2 gas mixture containing 0%, 1%, 2%, 4%, 8%, 12%, 16%, and 21% O_2. The gas fluxes were controlled with a flow-mixer setup (OxiQuant S, Envitec GmbH, Wismar, Germany). Specifically, before each measurement, the fibers was kept at 100% N_2 flow for 2 minutes. Subsequently, it was purged with the targeted O_2/N_2 mixture for another 2 minutes. Photoluminescence measurements were obtained at the desired O_2/N_2 ratio by exciting the sensors in a range of 280-600 nm and recording an emission spectrum in the range of 300-800 nm.

The lifetime analysis was performed with a Horiba DeltaPro (Horiba Jobin Yvon GmbH, Bensheim, Germany) for fibers at the excitation wavelength of 510 nm under standard air and anoxic environment (100% N_2).

To test the sensor reversibility, the O_2 concentration in the custom-built chamber was switched between 0 and 21% O_2 for ten times. The measurement chamber was purged with a mixture of N_2/CO_2 at the ratio of 60:40 or N_2/CO_2 at the ratio of 100:0 to investigate the sensor cross-sensitivity towards CO_2. Similarly, the chamber was respectively kept under 80% and 20% relative humidity level at room temperature while purging with constant N_2/O_2 flow at the ratio of 79:21 to test the cross-interference of humidity.

5.4 Results and Discussion

5.4.1 Reproducibility of MA-PPD6 nanoparticles

MA-PPD photoemitters were synthesized as described in the previous chapter and according to the literature[262]. Similar to Chapter 4, the photoemitters synthesized through a hydrothermal reaction, named MA-PPD6 with 6 indicating the reaction time in hours, were evaluated based on their chemical and optical characterization. Nanometer-sized particles with average diameters of 3 nm were synthesized at a constant precursor concentration of 1 mg/mL, as shown in the HR-TEM images in Figure 5.1.
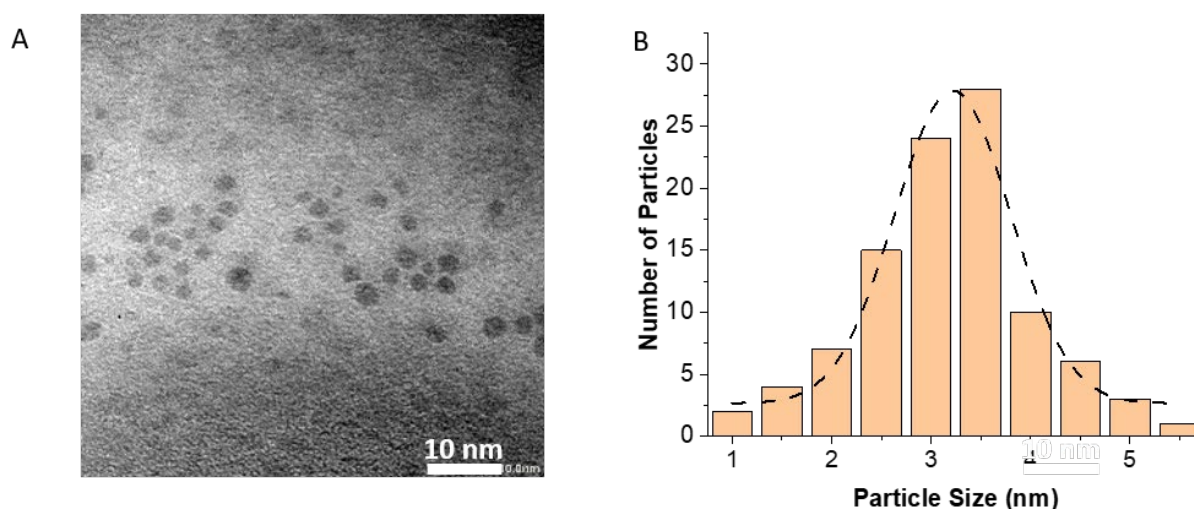
Figure 5.1 High-resolution transmission electron microscopy images. (A) MA-PPD6 and (B) the size distribution of one-hundred MA-PPD6 nanoparticles.

To confirm the successful formation of the expected functional groups of MA-PPD6, I performed FT-IR on our photoemitters. Figure 5.2 shows the FT-IR spectra of previously synthesized and as-synthesized MA-PPD6 nanoparticles. The peaks at 1775 cm^{-1} and 1718 cm^{-1}, attributed to the symmetric and asymmetric carbonyl (C=O) stretching, showed successful imide formation. The presence of the peaks corresponding to the C=O stretching of the amide bond and N-H in-plane bending of amide at 1627 cm^{-1} and 1556 cm^{-1} indicates that the final structure is composed of a mixture of imide and amide bonds. Furthermore, the C-N stretching vibrations of imide and amide, located at 1422 cm^{-1} and 1385 cm$^{-1,}$ respectively, indicate the mixture of amide and imide composition. Therefore, FT-IR analysis reveals that MA-PPD6 nanoparticles were successfully synthesized as described in the previous literature[262].
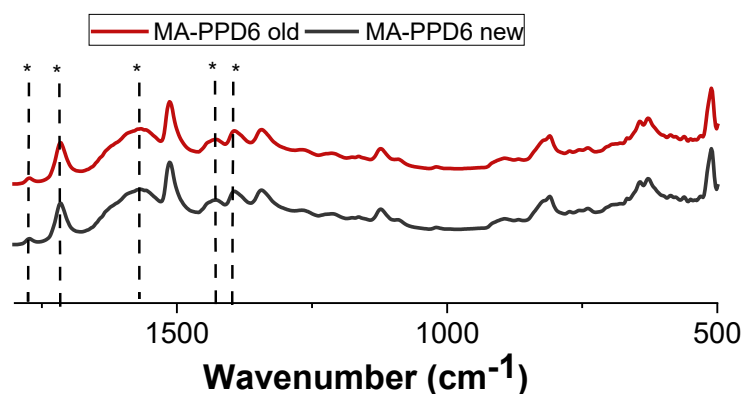
Figure 5.2 FT-IR spectra of MA-PPD6 nanoparticles for synthesized in the previous chapter (chapter 4) and as-synthesized.

To confirm the photoluminescence emission of as-synthesized MA-PPD6 nanoparticles, I recorded the photoluminescence spectra of MA-PPD6 nanoparticles dispersed in aqueous solutions. I observed photoluminescent emission at λ_{exc}= 585 nm, λ_{em}= 609 nm when samples were excited between 280-600 nm, as shown in Figure 5.3. The as-prepared MA-PPD6 nanoparticles show a consistent photoluminescence behavior, as described in chapter 4.
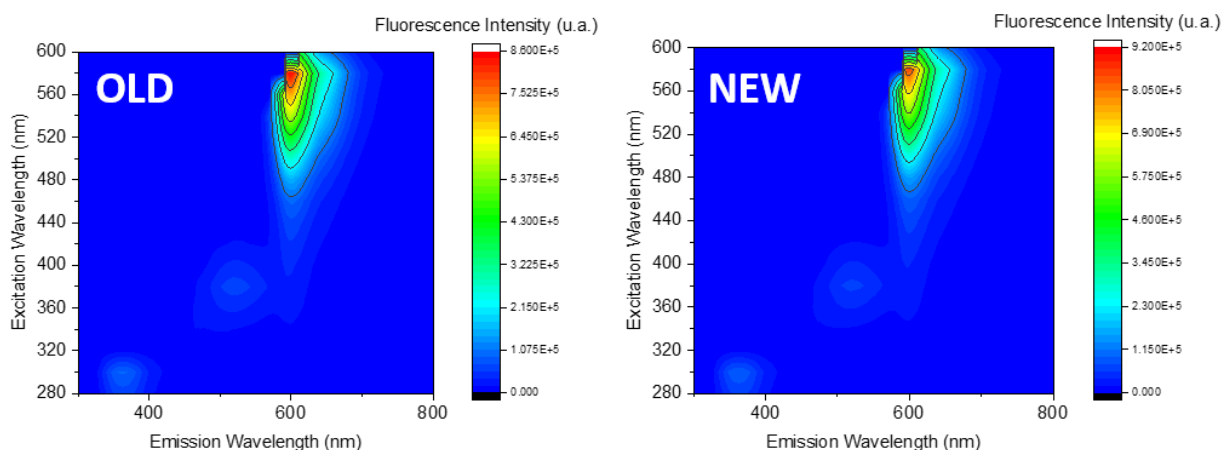
Figure 5.3 Photoluminescence contour plots of MA-PPD6 nanoparticles in aqueous medium for the previous chapter (chapter 4) and as-synthesized.

5.4.2 Viscoelastic Properties of PVA hydrogel

To understand the gelation kinetics and mechanical strength of the hydrogel network, I performed rheometer analysis on our gel precursor to investigate the viscoelastic properties of the norbornene functionalized PVA hydrogel network. The precursor was prepared as described in the method and gelled under UV irradiation to form an intact hydrogel, as confirmed with rheology and shown in Figure 5.4a. Upon UV exposure, nPVA hydrogels that contain MA-PPD6 nanoparticles formed instantly. Time-sweep analysis revealed an average gelation time below 20 s for all nPVA hydrogels regardless of the nanoparticle concentration, as shown in Figure 5.4b. The storage moduli (G') of nPVA hydrogels was 12 kPa independent of the nanoparticle concentration (Figure 5.4c). Thus, the storage moduli of our nPVA hydrogels are in good agreement with previously synthesized nPVA gels[264].
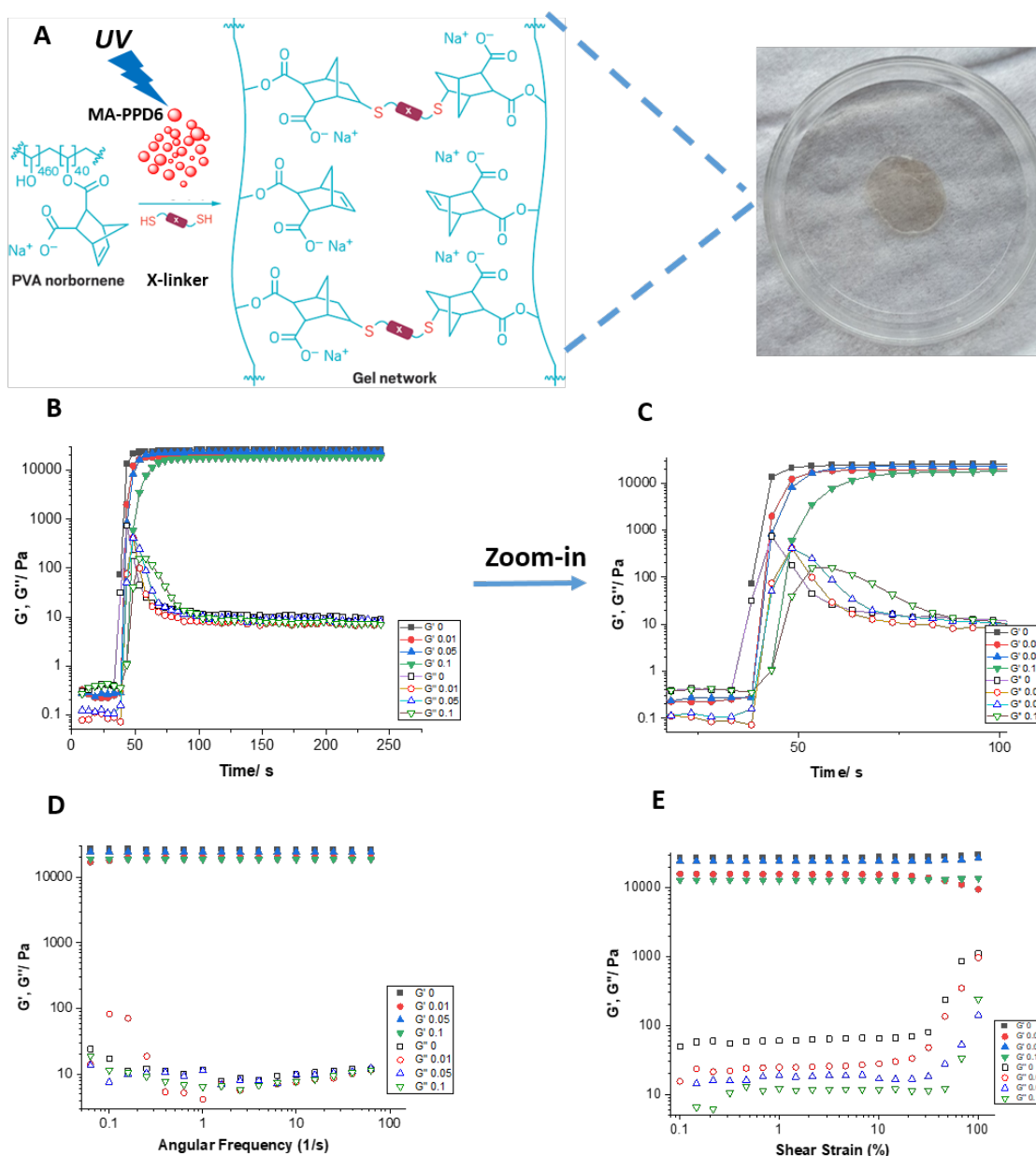
Figure 5.4 Rheometer Analysis of PVA hydrogel containing MA-PPD6 luminophore. (A) Preparation of a pre-polymer solution before rheometer measurement and its final form after the analysis. (The figure is adapted from [28]). (B) Time-sweep of gel storage moduli (G') at varying MA-PPD6 concentrations (0%, 0.01%, 0.05% and 0.1%), 10% nPVA, DTT as crosslinker (thiol-to-ene= 4:10), 0.005% photoinitiator). (C) Zoom-in version of the time-sweep analysis. (D) Frequency-sweep of PVA hydrogel network between 0.5 Hz and 100 Hz. (E) Amplitude-Sweep of PVA hydrogel network between the shear strain of 0.1% and 100%.

To investigate the gel strength, I performed frequency-sweeps and amplitude-sweeps on my nPVA hydrogel network. In the range of 0.5 Hz to 100 Hz, G' was independent of the angular frequency, as shown in Figure 5.4d. These results indicate the covalent cross-linking

of the polymers within the network instead of transient non-covalent cross-linking. Similarly, I did not observe significant changes in G' if shear strained, as shown in Figure 5.4e. These results indicate that my nPVA gels behave solid-like, indicating that the network is highly structured regardless of the nanoparticle concentrations.

5.4.3 Characterization of wet-spun fibers

The performance of optical fibers strongly depends on their dimensions. To quantify this parameter, I performed flow-mapping experiments of core and sheath precursors for different core/sheath flowrate ratios (Q_{core}/ Q_{sheath}) before the wet-spinning process. The core solution consisted of PVA polymer, whereas the sheath solution was alginate in an aqueous solution. The solutions were mixed with red eosine (core) and methylene blue (sheath), respectively, to enhance the image contrast. Figure 5.5 demonstrates the change of the core diameter as a function of the Q_{core}/ Q_{sheath} ratio. The diameter of the core flow increased almost linearly from 160 μm to 600 μm as the Q_{core}/ Q_{sheath} ratio increased from 1:9 and 9:1. This linear relation facilitates the deliberate tuning of the fiber dimensions, and hence, accelerates the wet-spinning. In addition, the faster fabrication process inhibits the self-photopolymerization of gel precursors before fiber formation occurs with the coagulation of sheath alginate solution in $CaCl_2$.
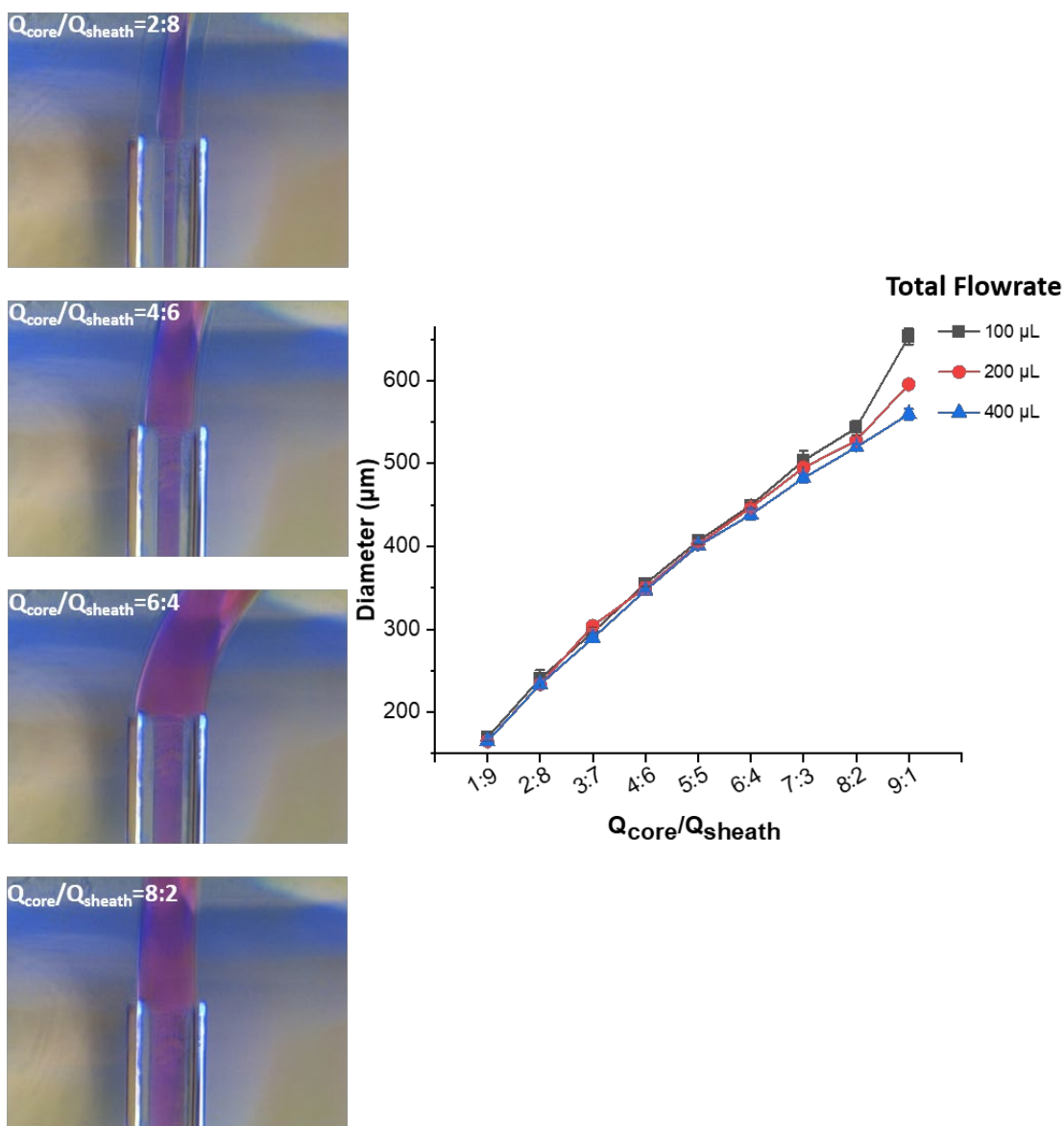
Figure 5.5 Flow-mapping analysis of core (red) and sheath (blue) flow to investigate the core diameter at various Q_{core}/Q_{sheath} ratio.

To compare the actual and expected fiber diameters obtained from flow-mapping analysis, optical microscopy was used to take the images of all wet-spun fibers. The visually measured fiber diameter increased almost linearly with the Q_{core}/Q_{sheath} ratio from 240 μm to 605 μm, as shown in Figure 5.6 and summarized in Table 5.1. This result is in good agreement with my flow-mapping analysis.
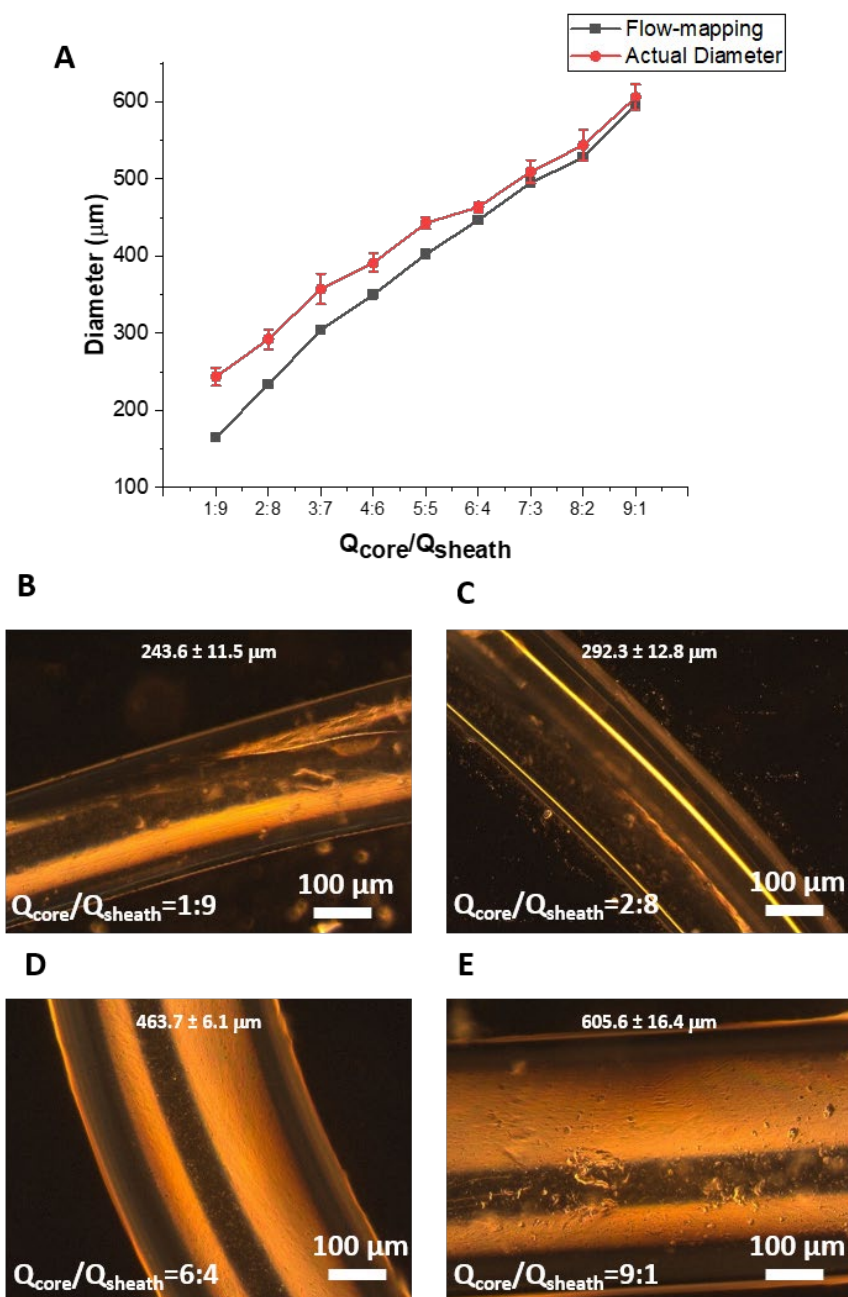
Figure 5.6 Optical microscopy analysis of nPVA/MA-PPD6 hydrogel fibers. (A) Comparison between actual and expected fiber diameter at increasing Q_{core}/Q_{sheath} ratio. Optical microscopy image of wet-spun fibers at Q_{core}/Q_{sheath}= 1:9 (B), 2:8 (C), 6:4 (D) and 9:1 (E).

		Fiber Diameter (μm)
Q_{core}/ Q_{sheath}	1:9	243.6±11.5
	2:8	292.3±12.8
	3:7	347.6±26.3
	4:6	387.4±13.7
	5:5	441.9±8.3
	6:4	463.7±6.1
	7:3	497.7±16.9
	8:2	531.2±21.1
	9:1	605.6±16.4

Table 5.1 nPVA/MA-PPD6 wet-spun fiber diameter at different Q_{core}/ Q_{sheath} ratio.

To investigate the elastic properties of nPVA gel fibers, atomic force microscopy has been performed on each wet-spun fiber-containing different concentrations of MA-PPD6 luminophores. The force vs. indentation depth curve of wet-spun fibers was obtained using the contact mode of AFM, as shown in Figure 5.7a. To calculate the elastic moduli of PVA gel fibers, the Hertz contact mechanic model, well-suited for soft materials, was selected to fit the force vs. indentation depth curve [265]. The Hertz model is;

$$F = \frac{4}{3}\frac{E}{1-\mu^2}\sqrt{R\delta^3} \tag{1}$$

where F is applied force, E is elastic modulus, μ is Poisson's ratio, R is the radius of the probe, and δ is the indentation of the sample. A Poisson's ratio of 0.44 was assumed, as previously calculated for PVA hydrogels[266]. Figure 5.6a shows the fitted Hertz model as a red line. The elastic modulus of my nPVA hydrogels containing 0.5% MA-PPD6 was calculated as 21.9±0.13 kPa. No significant change in elastic modulus was observed for different MA-PPD6 concentrations, indicating that the nanoparticles do not significantly affect the elastic properties of nPVA gel fibers (Figure 5.7b).
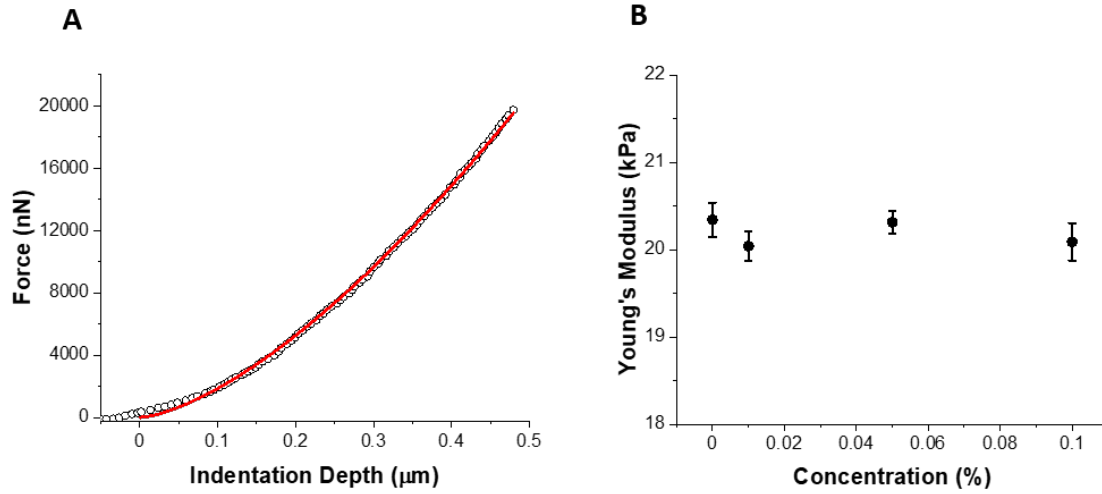
Figure 5.7 AFM analysis for the elastic properties of PVA hydrogel fibers containing MA-PPD6. (A) Force vs. Indentation depth curve fitted with The Hertz Model. (B) Young Modulus of PVA hydrogel fibers with different MA-PPD6 concentration.

E moduli can also be determined from the storage (G') moduli using;

$$E = 2G(1 + \mu) \quad \text{and} \quad G = \sqrt{G'^2 + G''^2} \tag{2}$$

where E is elastic modulus, G is shear modulus, μ is Poisson's ratio, G' is shear storage modulus, and G'' is shear loss modulus. For a Poisson's ratio of 0.44, E moduli correspond to 22.5 kPa based on Equation 2. The calculated E moduli are in good agreement with the values obtained from AFM analysis.

5.4.4 The O_2 sensing performance of nPVA/MA-PPD6 hydrogel fibers

The key characteristic of O_2 sensors is their O_2-dependent photoluminescence. To quantify this parameter, we performed photoluminescence measurement on nPVA/MA-PPD6 hydrogel fibers, having different fiber diameters for O_2 concentrations between 0% and 21%. The PL intensity of MA-PPD6 nanoparticles embedded in a nPVA fiber increases with decreasing oxygen concentration. To quantify this increase, we determine the ratio between the PL intensity at 0% and 21% O_2 as $I_{0\%}/I_{21\%}$. For nPVA/MA-PPD6 hydrogel fibers produced at Q_{core}/Q_{sheath}=9:1, 8:2, 7:3, 6:4, 5:5, 4:6, 3:7, 2:8, and 1:9, $I_{0\%}/I_{21\%}$ was 3.85, 3.97, 4.07, 4.12, 4.21, 4.34, 4.38, 4.47 and 4.51, respectively (Figure 5.8d). The maximum $I_{0\%}/I_{21\%}$ value of 4.51 is 53% higher than those of the previously reported organic optical O_2

sensor films that have a similar sensing range of 0-21% O_2[262,267]. Such a significant increase is ascribed to the high porosity and surface-to-volume ratio of wet-spun hydrogel fibers that facilitate the O_2 diffusion through the sensing unit.
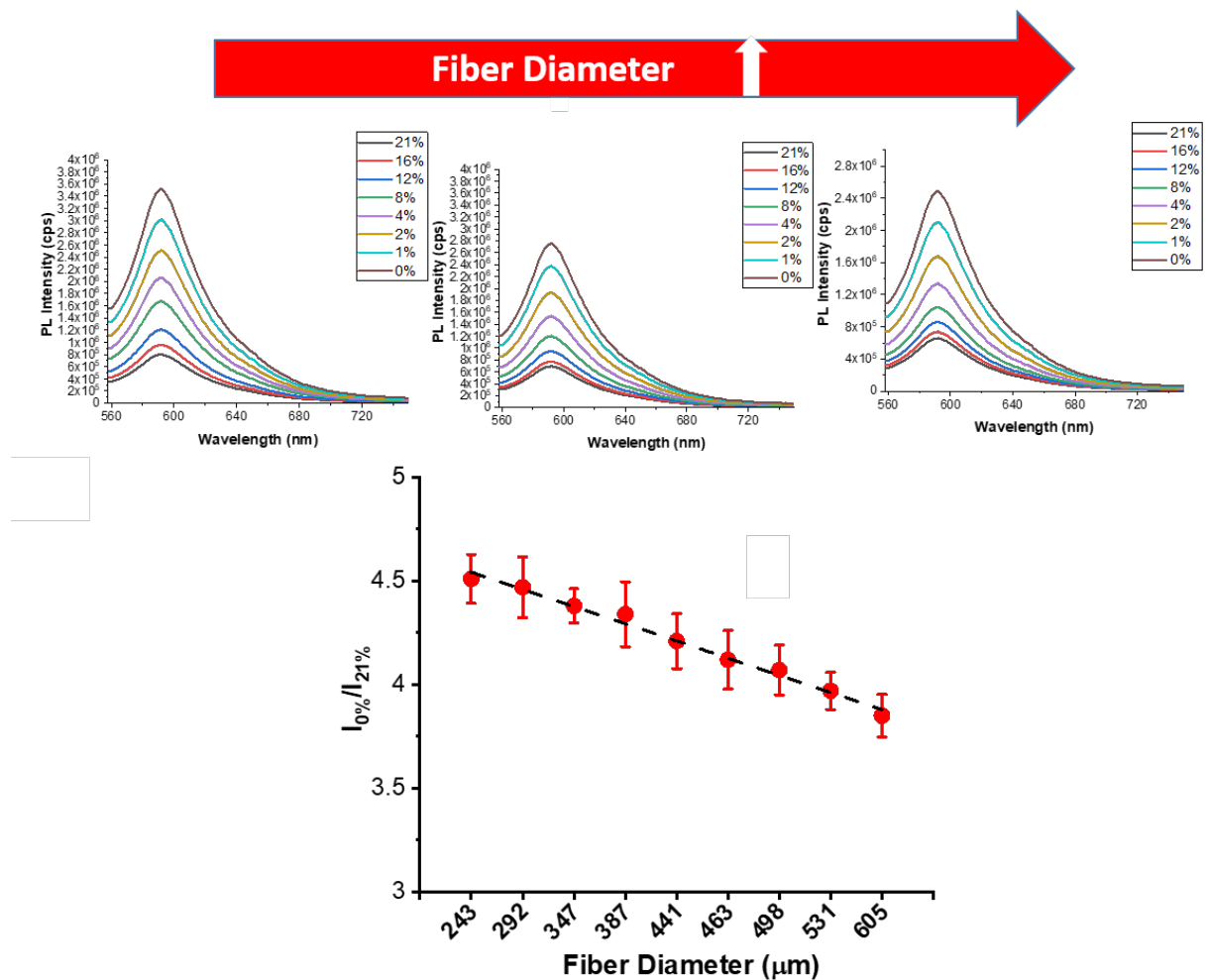
Figure 5.8 Oxygen sensitivity of nPVA/MA-PPD6 hydrogel fiber between 0% and 21% O_2 concentration with increasing fiber diameter.

I observed a linear decrease of the O_2 sensitivity as the fiber diameter increases (Figure 5.8d) with R^2 of 0.991. The relationship between fiber diameter and luminescence intensity as shown below;

$$I_{0\%}/I_{21\%} = -0.08d + 4.62$$

where $I_{0\%}$ is luminescence intensity at 0% O_2, $I_{21\%}$ is luminescence intensity at 21% O_2, and d is fiber diameter (µm).

To investigate this behavior, I performed oxygen permeability measurement on nPVA/MA-PPD6 hydrogel films with different film thicknesses, similar to produced fiber diameter. Therefore, nPVA/MA-PPD6 membranes with a wall thickness from 250 µm to 650µm were fabricated by drop-casting technique. The resultant oxygen transmission rate (OTR) vs. nPVA/MA-PPD6 film thickness was fitted to the second-order polynomial function with R^2 of 0.995. The O_2 diffusion through the nPVA membrane was decreased three times as wall thickness increased from 250 µm to 650 µm, as shown in Figure 5.9a. Figure 5.9b combines the O_2 sensitivity of nPVA/MA-PPD6 hydrogel fiber and O_2 permeability of nPVA hydrogel film. The $I_{0\%}/I_{21\%}$ vs. OTR was fitted to the second-order polynomial function (R^2 equal to 0.991). The oxygen sensitivity increases parabolically with increasing O_2 permeability, reaching the saturation point because the maximum number of MA-PPD6 luminophores colliding with O_2 molecules. This behavior might explain the decrease of O_2 sensitivity at increasing fiber diameters. A thick hydrogel network might prevent O_2 molecules from reaching the luminescent nanoparticles at the center of the fibers within the investigated timeframe.
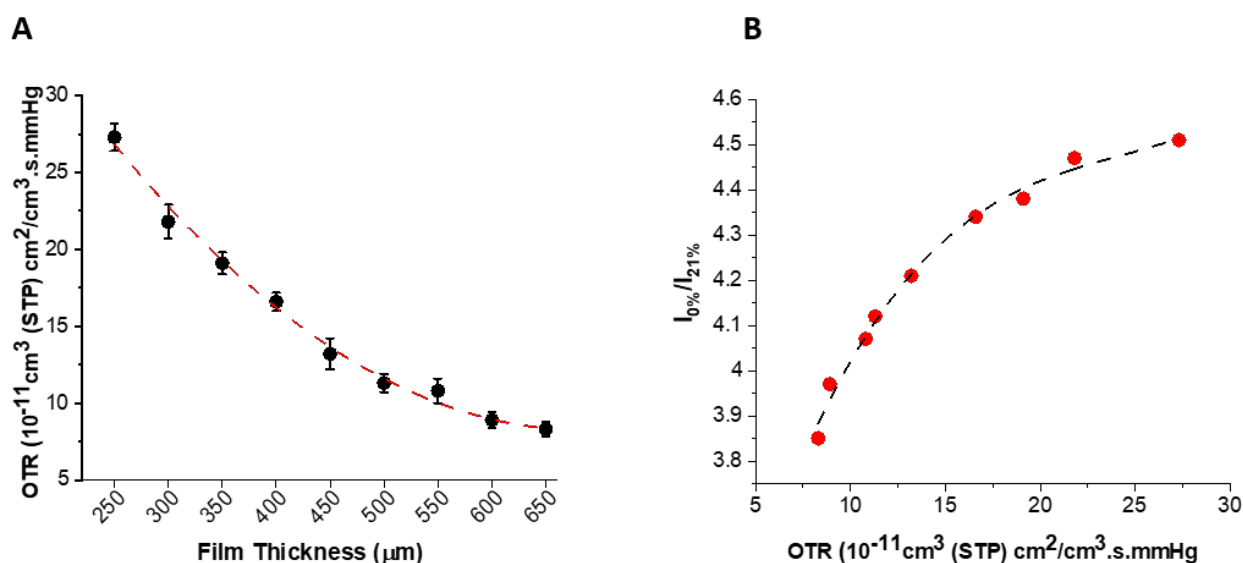
Figure 5.9 (A) Oxygen permeability analysis on nPVA/MA-PPD6 films with different film thickness **(B)** Oxygen permeability of nPVA film vs O_2 sensitivity of nPVA/MA-PPD6 fiber for similar film thickness and fiber diameter.

To quantify the O_2 sensing performance, I analyzed the best performing sample, nPVA/MA-PPD6 hydrogel, with a fiber diameter of 243 µm. I measured the emission spectra within an O_2 concentration range of 0-21%, as shown in Figure 5.10a. The emissive state of MA-PPD6 was quenched until the O_2 concentration reached 21%, as shown in Figure 5.10a,

indicating that my sensors can be used within this O_2 range. Note that the O_2 sensing range has been significantly improved compared to previous systems, which can detect up to 16% O_2[262]. I assign the broader O_2 sensing range (0-21%) of my sensor to the high O_2 permeability and the surface-to-volume ratio of wet-spun fibers obtained by microfluidic wet-spinning[268]. To quantify the sensitivity, I fitted the Stern-Volmer plot to a first-order polynomial function between 0-21% O_2 (R-square = 0.999) (Figure 5.10a). The limit of detection (LOD) was calculated according to the extrapolated concentration at which the signal is three times the averaged standard deviation (3σ) of the fluorescence intensity. A detection limit of 320 ppm was achieved with good linearity in the range of 0-21% O_2. The excellent quality of the fits indicates that my sensors display a linear response to the O_2 concentration up to 21%. It has been previously discussed that the linear calibration curve is desirable for simple one-point instrument calibrations that enable the standard calibration cards for the sensors[269]. The Stern-Volmer quenching constant was calculated in accordance with the Stern-Volmer Equation.

$$ {I_0}/{I} = 1 + K_{sv}.[O_2] \tag{4} $$

where I_0 and I represent the luminescence intensities in the absence and presence of O_2, respectively. K_{sv} is the Stern-Volmer quenching constant, and $[O_2]$ is the oxygen concentration in the environment. The Stern-Volmer constant (K_{sv}) was calculated to be 0.171 kPa^{-1} for the linear response range of 0-21% O_2.
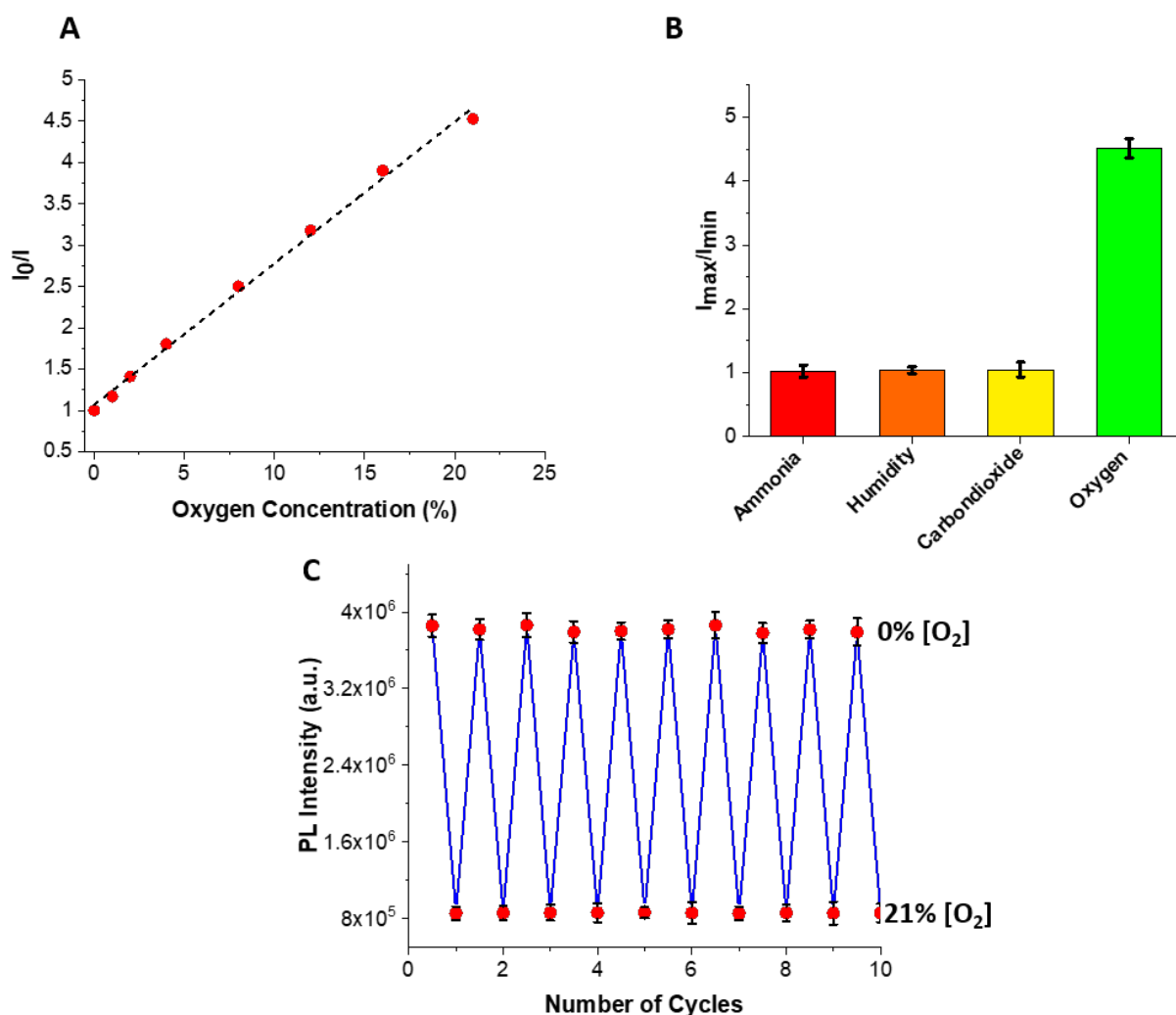
Figure 5.10 O$_2$ Sensor Features of nPVA/MA-PPD6 hydrogel fiber. (A) The Stern-Volmer Fitting of nPVA/MA-PPD6 fibers. (B) Sensing cross-interference of humidity, CO$_2$ and ammonia towards O$_2$. (C) Sensing reversibility of PVA/MA-PPD6 sensor exposed to 10 concentration cycles of 0 - 21% O$_2$.

To investigate the cross-interference of different atmospheric gases, such as humidity, CO$_2$, ammonia towards my optical O$_2$ sensors, I measured luminescent intensity change of my optical sensors in the presence of 20% and 80% relative humidity, in the presence of 0% and 60% CO$_2$, or in the presence of 0 and 200 ppm ammonia, as shown in Figure 5.10b. The result indicates that no significant PL intensity change was observed for nPVA/MA-PPD6 hydrogel fibers when changing the humidity, CO$_2$, or ammonia concentration in the measurement chamber. The maximum and minimum PL intensity (I$_{max}$/I$_{min}$) ratio was calculated 1.03, 1.04, and 1.02 within the range of 20-80% relative humidity, 0-60% CO$_2$ and 0-200 ppm ammonia, respectively. This indicates that nPVA/MA-PPD6 hydrogel fiber can be used for reliable O$_2$ sensing without any cross-interference of other atmospheric gases.

The repetitive detection of O_2 concentration without significant signal loss is crucial for the long-term use of optical O_2 sensors. Therefore, I investigated the reversibility of my O_2 sensors by cycling the O_2 concentration between 0% and 21% O_2 ten times, as shown in Figure 5.10c. The result demonstrates that no significant signal loss was observed within ten cycles, indicating no noticeable photo-oxidatation in nPVA hydrogel fibers containing MA-PPD6 sensing unit.
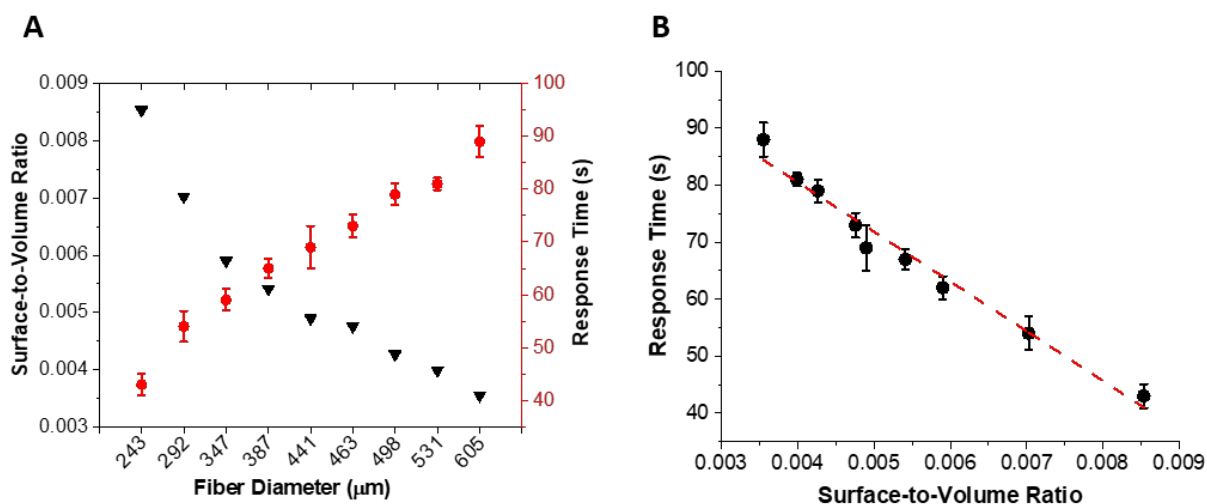
Figure 5.11 Response time of nPVA/MA-PPD6 hydrogel fiber. (A) The response time (red) and surface-to-volume ratio (black) of nPVA/MA-PPD6 fibers with different fiber diameter. (B) The response time vs. Surface-to-volume ratio of nPVA/MA-PPD6 fibers were fitted to first-order polynomial equation.

To test the speed of the sensor response to O_2 concentration changes, the response time of the PVA/MA-PPD6 sensors was measured within one cycle of 0%-21%-0% O_2. Upon exposure to 21% O_2, the time required to reduce the PL intensity by 95% (Δt_{95min}) was 41 seconds for the thinnest nPVA/MA-PPD6 hydrogel fiber, as shown in Figure 5.11a. The response of MA-PPD6 nanoparticles is significantly faster than those of previously reported similar polyimide-based organic optical O_2 sensor[262]. Such a clear improvement in response time is attributed to the high O_2 permeability and the surface-to-volume ratio of PVA hydrogels. Indeed, I observed a linear relationship between the response time and the surface-to-volume ratio of the sensors with R^2 of 0.985, as shown in Figure 5.10b. The greater surface area facilitates the O_2 transportation into the sensing unit, leading to fast response of the optical oxygen sensor.
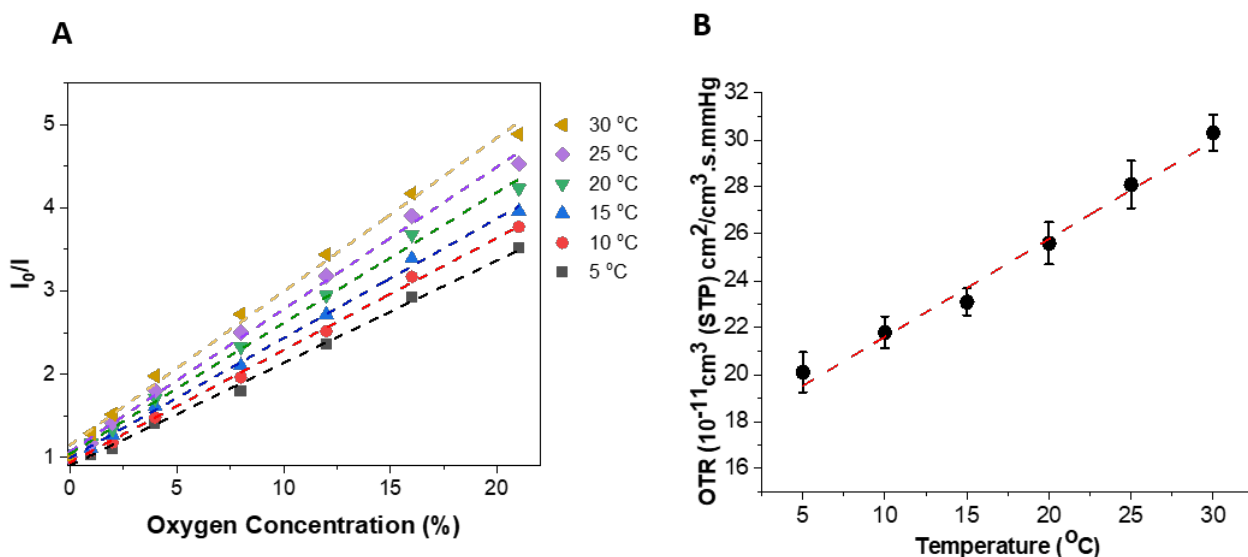
Figure 5.12 (A) Temperature dependence of O_2 sensitivity of nPVA/MA-PPD6 hydrogel fibers. (B) O_2 permeability of nPVA/MA-PPD6 films at different temperatures.

To test the effect of temperature on the sensor performance of nPVA/MA-PPD6 hydrogel fibers, I measured the O_2 sensitivity of our sensor between 5°C and 30°C. The temperature dependence of our O_2 sensor shows a positive slope as the temperature increases (Figure 5.12a). For the desired response range (0-21% O_2), the temperature-dependent Stern-Volmer constant change ($\Delta K_{sv}/\Delta T$) was found to be 0.0096 kPa^{-1} °C^{-1} for the temperature range of 5-30°C (R^2 equals to 0.985). The positive temperature coefficient of nPVA/MA-PPD6 sensor is in good agreement with the previously fabricated optical O_2 sensors[270,271]. I also performed an oxygen permeability test for nPVA/MA-PPD6 hydrogel films with a thickness of 250 µm between 5-30°C to investigate the O_2 diffusion kinetics. OTR of nPVA/MA-PPD6 hydrogel films vs. temperature was fitted to the first-order polynomial equation (R^2 equals 0.984). I observed a significant increase in O_2 transportation through the membrane at elevated temperatures (Figure 5.12b). One reason for the increase in O_2 sensitivity at high temperatures could be the higher oxygen diffusion rate into the nPVA hydrogel network. Other possible reasons could be 1) the solubility of oxygen in the PVA matrix and 2) the dynamic quenching constant, as previously discussed in the literature[272]. Cross-sensitivity of the sensor on temperature change has to be known when using these sensors, especially in biomonitoring and food packaging applications, where the sensors were generally used at low or high temperatures. The linear temperature dependency enables the simple correction for the sensor calibration at different temperatures.

5.4   Conclusion

A purely organic optical O_2 hydrogel fiber sensor was fabricated by embedding polyimide-based nanoparticles within a norbornene-functionalized PVA hydrogel matrix via microfluidic wet-spinning. My results indicate that the O_2 sensitivity of nPVA hydrogel fibers is significantly higher than the conventional PVA-based polymer matrix containing polyimide nanoparticles. The O_2 sensitivity of nPVA hydrogel fiber drastically decreases with increasing fiber diameter due to the thick hydrogel network, resulting in low O_2 permeability. The nPVA/MA-PPD6 sensors can detect O_2 in the whole physiological range up to concentrations of 21% O_2 with an excellent linear response. Furthermore, the high surface-to-volume ratio and porosity of my nPVA hydrogel fiber enable efficient O_2 transportation through the hydrogel network, leading to a drastic decrease in response time. Such metal-free sensors are resistant to photobleaching and atmospheric interference with continuous and fast O_2 sensing, making them appealing for detecting O_2 in the food packaging industry or integrated biomonitoring.

Chapter 6

Conclusion

More than thirty years of research in optical O_2 sensors have produced a plethora of luminophores, encapsulation matrices, designs, and processes to fabricate active elements for O_2 sensing. However, physical encapsulation of the sensing unit in organic or inorganic matrices through mixture formulations and casting of sensor coatings, although it looks simple, has limitations in terms of sensor reproducibility, heterogeneity, luminophore leaching, process control, and overall costs. In this thesis, I study how to fabricate purely organic optical O_2 sensors for broad-range, continuous, reversible, and fast sensing without any significant limitations.

In the first part of this work, I studied how to improve the range of O_2 sensitivity of organic optical O_2 sensors by increasing the structural rigidity of the O_2 sensing unit. Therefore, I synthesized different diamine-based luminophores where I changed the crosslinker molecules between each diamine-based luminophores. Crosslinking the sensing unit with a highly rigid polyimide network leads to an O_2 response range of 0-16% O_2, whereas I could obtain only 0-8% O_2 response if urea is used as linker molecules between diamine-based luminophores. I found out that structural rigidity plays a significant role in the O_2 quenching range of optical O_2 sensors due to suppressing the non-radiative recombination, resulting in an efficient RTP mechanism. I also show that the polyimide-crosslinked sensing material exhibits good sensor reversibility, indicating that no noticeable photo-oxidation occurs in long-term use. Moreover, no significant cross-interference between the other atmospheric gases, such as humidity or CO_2, was observed, enabling my optical sensor reliable for only O_2 sensing for desired applications. However, the slow response time (~7.5 min) of PVA encapsulated polyimide-based optical O_2 sensor, due to the low O_2 permeability of PVA matrix, limits the use of these sensors, especially in biosensing or biomonitoring

In the second part of this work, I studied enhancing O_2 sensitivity and response time of previously fabricated polyimide-based optical O_2 sensors. Therefore, I changed the polymer matrix, which encapsulates the sensing unit, to have efficient O_2 diffusion using porous

and O_2 permeable nPVA hydrogel matrix. I demonstrated that the O_2 sensitivity of MA-PPD6 nanoparticles was improved by 53% when embedded into nPVA hydrogel instead of the conventional PVA matrix. I also show that the O_2 permeability greatly influences the O_2 sensitivity and operational range of optical O_2 sensors. Thick nPVA/MA-PPD6 hydrogel fiber exhibit a drastic decrease in O_2 sensitivity due to the limited O_2 diffusion through the hydrogel network.

Moreover, nPVA/MA-PPD6 hydrogel fiber can detect O_2 concentration up to 21% O_2 with a linear response, enabling simple one-point sensor calibration. I also investigated the effect of the surface-to-volume ratio on the sensor response rate. The best performing nPVA/MA-PPD6 hydrogel fiber shows a response time of 41 s, significantly faster than that of MA-PPD6 embedded into conventional PVA film. High structural porosity and the high surface-to-volume ratio of fibers accelerate O_2 transportation within the hydrogel network, leading to a quick reading of O_2 concentration by organic optical O_2 fiber sensors. This analysis indicates the importance of polymer matrix selection and shape of the sensor to have broad-range and fast optical O_2 sensors.

Such metal ion-free optical O_2 sensors with continuous, broad-range, and reversible sensing can be a good candidate for monitoring the modified atmosphere packaging, where minimum sensor toxicity and broad-range sensing (typically between 0.5% and 40% O_2) is required. Integration of my optical O_2 sensors into packaging could facilitate monitoring packaging failure at any stage, in a non-destructive manner, and each packaged product. Furthermore, the simple one-point calibration and good reversibility enable my optical O_2 sensors to operate accurately and continuously for long-term use.

The future study can be enhancing the O_2 sensitivity range up to the concentration of 40-60% O_2, where red meat products are mostly packaged to improve their color and appearance. For example, controlling the porosity and microarchitectural features of nPVA hydrogel network may help to tune the O_2 diffusion rate, leading to control over the operational range of my optical O_2 sensors. Moreover, fabricating the nPVA/MA-PPD6 hydrogel sensors with different shapes, such as micro/nanotubes or micro/nanocapsules, might improve the response time of my optical O_2 sensors that can enable ultra-fast O_2 detection, especially for biomonitoring and biosensing applications.

Curriculum Vitae

Personal information

Name   Efe Armagan

Date of birth   22.01.1991

Nationality   Turkish

Phone No.   +41792903062

Address   Neptunstrasse,4 9000 St.Gallen/Switzerland

Education

2017-Present   Ph.D at Instute of Materials in Ecole Polytechnique Fédérale de Lausanne (EPFL), Switzerland

2014-2016   M.Sc at Material Science and Nanotechnology in Sabanci University, Turkey

2009-2014   Minor Program in Chemistry, Sabanci University, Turkey

2009-2014   B.Sc at Material Science and Engineering in Sabanci University, Turkey

Research Experience

2017-Present   Ph.D Thesis- Empa, St.Gallen in Laboratory of Biomimetic Membranes and Textiles, supervised by Prof. Esther Amstad (EPFL, Soft Materials Laboratory) and Prof. René Michel Rossi

- Developing purely organic optical O_2 sensing unit with rigid crosslinking network for efficient O_2 quenching
- Investigating the effect of polymer matrix in organic optical O_2 sensor on O_2 sensitivity and robust sensing

2014-2016   M.Sc Thesis- Material Science and Nanotechnology in Sabanci University, supervised by Prof. Gozde Ozaydin-Ince

- Developing pH and temperature responsive co-axial polymer nanotube by initiated chemical vapor deposition for tunable release of drug molecules
- Developing conductive polymeric nanotube by oxidative chemical vapor deposition for humidity sensing application

2013-2014   B.Sc Thesis- Material Science and Engineering in Sabanci University, supervised by Prof. Gozde Ozaydin-Ince

- Fabricating pH responsive polymeric nanotube by initiated chemical vapor deposition for triggered release of drug molecules

Work Experience

06-09/2013   Summer Internship- Chemical Engineering in Massachusetts Institute of Technology (MIT), supervised by Karen Klincewicz Gleason

- Fabricating anti-biofouling surfaces by initiated chemical vapor deposition technique

2012-2016   Teaching Assistantship- Sabanci University

- Nature of Science 1 (NS 101) Teaching Assistantship
- Nature of Science 2 (NS 102) Laboratory Assistantship
- Material Characterization (MAT 405) Teaching Assistantship
- Surface Chemistry (MAT 401) Teaching Assistantship
- Introduction to Nanoscience (MAT 406) Teaching Assistantship

Awards

Sabanci University Full Honor Scholarship

Sabanci University High Honor List

Sabanci University M.Sc Full Honor Scholarship

Publications

1) M. T. Matter, L. Maliqi, K. Keevend, S. Guimond, J. Ng, **E. Armagan**, M. Rottmar, I. K. Herrmann, **"**One-Step Synthesis of Versatile Antimicrobial Nano-Architected Implant Coatings for Hard and Soft Tissue Healing", ACS Appl. Mater. Interfaces, 2021, https://doi.org/10.1021/acsami.1c10121
2) **E.Armagan**, K. Wei, G. Fortunato, E. Amstad, R. M. Rossi, "Reversible and Broad-Range Oxygen Sensing Based on Purely Organic Long-Lived Photoemitters", ACS Appl. Polym. Mater., 2021, 3, 2480.
3) A.Gursoy, K. Iranshahi, K. Wei, A. Tello, **E. Armagan**, L. F. Boesel, F. Sorin, R. M. Rossi, T. Defraeye, C. Toncelli, "Facile Fabrication of Microfluidic Chips for 3D Hydrodynamic Focusing and Wet Spinning of Polymeric Fibers", Polymers, 2020, 12, 633.
4) **E. Armagan**, S. Thiyagarajan, K. Wei, A. Gursoy, G. Fortunato, E. Amstad, R. M. Rossi, C. Toncelli, " Reversible oxygen sensing based on multi-emission fluorescence quenching", Sensors, 2020, 20, 477.
5) **E. Armagan**, D. B. Papkovsky, C. Toncelli, " New polymer-based sensor materials and fabrication technologies for large-scale applications", Detection Science Series No. 11 Quenched-phosphorescence Detection of Molecular Oxygen: Applications in Life Sciences, RSC, 2018, 19-49.

6) C. P. Hsu, Z. Hejazi, **E. Armagan**, S. Zhao, M. Schmid, H. Zhang, H. Guo, L. Weidenbacher, R. M. Rossi, M. M. Koebel, L. F. Boesel, C. Toncelli, " Carbon dots and fluorescein: The ideal FRET pair for the fabrication of a precise and fully reversible ammonia sensor", Sensors and Actuators B, 2017, 253, 714.

7) A. Balkan*, **E. Armagan*,** G. Ozaydin-Ince, " Synthesis of coaxial nanotubes of polyaniline and poly (hydroxyethyl methacrylate) by oxidative/initiated chemical vapor deposition**,** Beilstein J. Nano-technol., 2017, 8, 872. (*equal contribution)

8) M. Nedaei, **E. Armagan**, M. Sezen, G. Ozaydin-Ince, A. Kosar, " Enhancement of Flow Boiling Heat Transfer in pHEMA/pPFDA Coated Microtubes with Longitudinal Variations in Wet-tability", AIP Advances, 2016, 6, 035212.

9) **E. Armagan,** G. Ozaydin-Ince, " Coaxial nanotubes of stimuli responsive polymers with tunable re-lease kinetics", Soft Matter, 2015, 11, 8069.

10) **E. Armagan,** P. Qureshi, G. Ozaydin-Ince, "Functional nanotubes for triggered release of molecules", Nanoscience and Nanotechnology Letters, 2015, 7, 79.

11) T. A. Cikim, **E. Armagan**, G. Ozaydin-Ince, A. Kosar, "Flow boiling enhancement in microtubes with pHEMA coatings", 2013, Journal of Heat Transfer, 136, 081504.

12) C. Petruczok, **E. Armagan**, G. Ozaydin-Ince and K. Gleason, "Initiated chemical vapor deposition and light responsive crosslinking of Poly(Vinyl Cinnamate) thin film", Macromolecular Rapid Communica-tions, 2014, 35, 1345.

13) A. Kaya, R. Demiryurek, **E. Armagan**, G. Ozaydin-Ince, M. Sezen, A. Kosar, " Boiling heat transfer en-hancement in mini/microtubes via polyhydroxyethylmethacrylate (pHEMA) coatings on inner micro-tube walls at high mass fluxes", Journal of Micromechanics and Microengineering, 2013, 23, 115017.

14) G. Ozaydin-Ince, **E. Armagan**, H. Erdogan, F. Buyukserin, L. Uzun, G. Demirel, " One-dimensional sur-face-imprinted polymeric nanotubes for specific biorecognition by initiated chemical vapor deposi-tion (iCVD), ACS Appl. Mater and Interfaces, 2013, 5, 6447.

Presentations

1) Qureshi Parveen, **Armagan Efe** and Ozaydin Ince Gozde (2014) Fabrication of Thermo-Responsive polymeric nanotubes for release and diffusion studies using iCVD. In: NanoTR10, Istanbul, Turkey (Poster)

2) **Armagan Efe** and Ozaydin Ince Gozde (2015) Functional Nanotubes for Triggered Release of Mole-cules. In: NanoTR11, Ankara, Turkey (Poster)

3) **Armagan Efe** and Ozaydin Ince Gozde (2015) Functional Nanotubes for Triggered Release of Mole-cules, In: MRS 2015 Fall, Boston, USA (Poster)

4) **Armagan Efe**, Tufani Ali, and Ozaydin Ince Gozde (2015) Conformal and Non-Conformal Hybrid Mem-brane for Hydrodynamic Permeation, In: MRS 2015 Fall, Boston, USA (Talk)

BIBLIOGRAPHY

(1)   Wolfbeis, O. S. Sensor Paints. *Adv. Mater.* **2008**, *20* (19), 3759–3763. https://doi.org/10.1002/adma.200702276.

(2)   Quaranta, M.; Borisov, S. M.; Klimant, I. Indicators for Optical Oxygen Sensors. **2012**, No. November, 115–157. https://doi.org/10.1007/s12566-012-0032-y.

(3)   Papkovsky, D. B.; Dmitriev, R. I. Biological Detection by Optical Oxygen Sensing. *Chem. Soc. Rev.* **2013**, *42* (22), 8700–8732. https://doi.org/10.1039/c3cs60131e.

(4)   Ding, L.; Wang, X. D. Luminescent Oxygen-Sensitive Ink to Produce Highly Secured Anticounterfeiting Labels by Inkjet Printing. *J. Am. Chem. Soc.* **2020**, *142* (31), 13558–13564. https://doi.org/10.1021/jacs.0c05506.

(5)   Mills, A.; Mills, A. Oxygen Indicators and Intelligent Inks for Packaging Food. **2007**, 1003–1011. https://doi.org/10.1039/b503997p.

(6)   Banerjee, S.; Kelly, C.; Kerry, J. P.; Papkovsky, D. B. High Throughput Non-Destructive Assessment of Quality and Safety of Packaged Food Products Using Phosphorescent Oxygen Sensors. *Trends Food Sci. Technol.* **2016**, *50*, 85–102. https://doi.org/10.1016/j.tifs.2016.01.021.

(7)   Realini, C. E.; Marcos, B. Active and Intelligent Packaging Systems for a Modern Society. *Meat Sci.* **2014**, *98* (3), 404–419. https://doi.org/10.1016/j.meatsci.2014.06.031.

(8)   Lee, S. J.; Rahman, A. T. M. M. *Intelligent Packaging for Food Products*; Elsevier Ltd, 2013. https://doi.org/10.1016/B978-0-12-394601-0.00008-4.

(9)   Amao, Y. Fundamental Review Probes and Polymers for Optical Sensing of Oxygen. **2003**, *12*, 1–12. https://doi.org/10.1007/s00604-003-0037-x.

(10)   Lehner, P.; Staudinger, C.; Borisov, S. M.; Klimant, I. Ultra-Sensitive Optical Oxygen Sensors for Characterization of Nearly Anoxic Systems. *Nat. Commun.* **2014**, *5*, 1–6. https://doi.org/10.1038/ncomms5460.

(11)   Toncelli, C.; Arzhakova, O. V.; Dolgova, A.; Volynskii, A. L.; Kerry, J. P.; Papkovsky, D. B. Phosphorescent Oxygen Sensors Produced by Spot-Crazing of Polyphenylenesulfide Films. *J. Mater. Chem. C* **2014**, *2* (38), 8035–8041. https://doi.org/10.1039/c4tc01390e.

(12)   Toncelli, C.; Arzhakova, O. V.; Dolgova, A.; Volynskii, A. L.; Bakeev, N. F.; Kerry, J. P.; Papkovsky, D. B. Oxygen-Sensitive Phosphorescent Nanomaterials Produced from High-Density Polyethylene Films by Local Solvent-Crazing. *Anal. Chem.* **2014**, *86* (3), 1917–1923. https://doi.org/10.1021/ac404072z.

(13)   Kelly, C. A.; Toncelli, C.; Kerry, J. P.; Papkovsky, D. B. Phosphorescent O2 Sensors Based on Polyolefin Fabric Materials. *J. Mater. Chem. C* **2014**, *2* (12), 2169–2174. https://doi.org/10.1039/c3tc32529f.

(14)   Kelly, C. A.; Toncelli, C.; Kerry, J. P.; Papkovsky, D. B. Discrete O2 Sensors Produced

by a Spotting Method on Polyolefin Fabric Substrates. *Sensors Actuators, B Chem.* **2014**, *203*, 935–940. https://doi.org/10.1016/j.snb.2014.06.103.

(15) Xue, R.; Behera, P.; Xu, J.; Viapiano, M. S.; Lannutti, J. J. Polydimethylsiloxane Core-Polycaprolactone Shell Nanofibers as Biocompatible, Real-Time Oxygen Sensors. *Sensors Actuators, B Chem.* **2014**, *192*, 697–707. https://doi.org/10.1016/j.snb.2013.10.084.

(16) Wang, X.; Yang, Y.; He, B. Improving Oxygen Sensing Performance of Ir(III) Complexes with Fluorine Atoms: Synthesis, Characterization and Sensing Behavior of Their Electrospinning Fibrous Films. *Sensors Actuators, B Chem.* **2017**, *241*, 957–966. https://doi.org/10.1016/j.snb.2016.11.001.

(17) Kai, R.; Jun, W.; Huali, J. Electrospinning Fibrous Films Doped with Iridium Complexes for High Performance Oxygen Sensing: Synthesis and Characterization. *Sensors Actuators, B Chem.* **2017**, *240*, 697–708. https://doi.org/10.1016/j.snb.2016.09.033.

(18) Yazgan, G.; Dmitriev, R. I.; Tyagi, V.; Jenkins, J.; Rotaru, G.-M.; Rottmar, M.; Rossi, R. M.; Toncelli, C.; Papkovsky, D. B.; Maniura-Weber, K.; Fortunato, G. Steering Surface Topographies of Electrospun Fibers: Understanding the Mechanisms. *Sci. Rep.* **2017**, *7* (1), 158. https://doi.org/10.1038/s41598-017-00181-0.

(19) Marín-Suárez, M.; Medina-Rodríguez, S.; Ergeneman, O.; Pané, S.; Fernández-Sánchez, J. F.; Nelson, B. J.; Fernández-Gutiérrez, A. Electrophoretic Deposition as a New Approach to Produce Optical Sensing Films Adaptable to Microdevices. *Nanoscale* **2014**, *6* (1), 263–271. https://doi.org/10.1039/c3nr03336h.

(20) Koren, K.; Borisov, S. M.; Klimant, I. Stable Optical Oxygen Sensing Materials Based on Click-Coupling of Fluorinated Platinum(II) and Palladium(II) Porphyrins - A Convenient Way to Eliminate Dye Migration and Leaching. *Sensors Actuators, B Chem.* **2012**, *169*, 173–181. https://doi.org/10.1016/j.snb.2012.04.062.

(21) Weigel, C.; Schneider, M.; Schmitt, J.; Hoffmann, M.; Kahl, S.; Jurisch, R. Self-Sufficient Sensor for Oxygen Detection in Packaging via Radio-Frequency Identification. *J. Sensors Sens. Syst.* **2015**, *4* (1), 179–186. https://doi.org/10.5194/jsss-4-179-2015.

(22) Quinn, M. K.; Yang, L.; Kontis, K. Pressure-Sensitive Paint : Effect of Substrate. **2011**, 11649–11663. https://doi.org/10.3390/s111211649.

(23) Wolfbeis, O. S. The Clark Electrode. **2015**, 921–928. https://doi.org/10.1002/bies.201500002.

(24) Mills, A. Oxygen Indicators and Intelligent Inks for Packaging Food. *Chem. Soc. Rev.* **2005**, *34* (12), 1003–1011. https://doi.org/10.1039/b503997p.

(25) Wang, X. D.; Wolfbeis, O. S. Optical Methods for Sensing and Imaging Oxygen: Materials, Spectroscopies and Applications. *Chem. Soc. Rev.* **2014**, *43* (10), 3666–3761. https://doi.org/10.1039/c4cs00039k.

(26) Lim, S. H.; Thivierge, C.; Nowak-sliwinska, P.; Han, J.; Bergh, H. Van Den; Wagni, G.;

Burgess, K.; Lee, H. B. In Vitro and In Vivo Photocytotoxicity of Boron Dipyrromethene Derivatives for Photodynamic Therapy. **2010**, 2865–2874. https://doi.org/10.1021/jm901823u.

(27) Wang, C. R.; Gong, Y. Y.; Yuan, W. Z.; Zhang, Y. M. Crystallization-Induced Phosphorescence of Pure Organic Luminogens. *Chinese Chem. Lett.* **2016**, *27* (8), 1184–1192. https://doi.org/10.1016/j.cclet.2016.05.026.

(28) Shimizu, M.; Shigitani, R.; Nakatani, M.; Kuwabara, K.; Miyake, Y.; Tajima, K.; Sakai, H.; Hasobe, T. Siloxy Group-Induced Highly Efficient Room Temperature Phosphorescence with Long Lifetime. *J. Phys. Chem. C* **2016**, *120* (21), 11631–11639. https://doi.org/10.1021/acs.jpcc.6b03276.

(29) Bolton, O.; Lee, D.; Jung, J.; Kim, J. Tuning the Photophysical Properties of Metal-Free Room Temperature Organic Phosphors via Compositional Variations in Bromobenzaldehyde/Dibromobenzene Mixed Crystals. **2014**.

(30) Shi, H.; An, Z.; Li, P. Z.; Yin, J.; Xing, G.; He, T.; Chen, H.; Wang, J.; Sun, H.; Huang, W.; Zhao, Y. Enhancing Organic Phosphorescence by Manipulating Heavy-Atom Interaction. *Cryst. Growth Des.* **2016**, *16* (2), 808–813. https://doi.org/10.1021/acs.cgd.5b01400.

(31) Bolton, O.; Lee, K.; Kim, H.; Lin, K. Y.; Kim, J. Organic Materials by Crystal Design. *Nat. Chem.* **2011**, *3* (3), 205–210. https://doi.org/10.1038/nchem.984.

(32) Chen, H.; Yao, X.; Ma, X.; Tian, H. Amorphous, Efficient, Room-Temperature Phosphorescent Metal-Free Polymers and Their Applications as Encryption Ink. *Adv. Opt. Mater.* **2016**, *4* (9), 1397–1401. https://doi.org/10.1002/adom.201600427.

(33) Kwon, M. S.; Yu, Y.; Coburn, C.; Phillips, A. W.; Chung, K.; Shanker, A.; Jung, J.; Kim, G.; Pipe, K.; Forrest, S. R.; Youk, J. H.; Gierschner, J.; Kim, J. Organic Materials. **2015**. https://doi.org/10.1038/ncomms9947.

(34) Kwon, M. S.; Lee, D.; Seo, S.; Jung, J.; Kim, J. Tailoring Intermolecular Interactions for Efficient Room-Temperature Phosphorescence from Purely Organic Materials in Amorphous Polymer Matrices. *Angew. Chemie* **2014**, *126* (42), 11359–11363. https://doi.org/10.1002/ange.201404490.

(35) Yang, S.-H.; Wu, K.-L.; Chi, Y.; Cheng, Y.-M.; Chou, P.-T. Tris(Thiocyanate) Ruthenium(II) Sensitizers with Functionalized Dicarboxyterpyridine for Dye-Sensitized Solar Cells. *Angew. Chemie* **2011**, *123* (36), 8420–8424. https://doi.org/10.1002/ange.201103515.

(36) Circularly Polarized Persistent Room-Temperature Phosphorescence from Metal-Free Chiral Aromatics in Air. **2016**. https://doi.org/10.1021/acs.jpclett.6b00554.

(37) Hirata, S.; Totani, K.; Zhang, J.; Yamashita, T.; Kaji, H.; Marder, S. R.; Watanabe, T.; Adachi, C. Efficient Persistent Room Temperature Phosphorescence in Organic Amorphous Materials under Ambient Conditions. *Adv. Funct. Mater.* **2013**, *23* (27), 3386–3397. https://doi.org/10.1002/adfm.201203706.

(38) Chaudhuri, D.; Sigmund, E.; Meyer, A.; Rçck, L.; Klemm, P.; Lautenschlager, S.;

Schmid, A.; Yost, S. R.; Voorhis, T. Van; Bange, S.; Hçger, S.; Lupton, J. M. Metal-Free OLED Triplet Emitters by Side-Stepping Kasha s Rule ** Angewandte. **2013**, 13449–13452. https://doi.org/10.1002/anie.201307601.

(39) Ratzke, W.; Schmitt, L.; Matsuoka, H.; Bannwarth, C.; Retegan, M.; Bange, S.; Klemm, P.; Neese, F.; Grimme, S.; Schiemann, O.; Lupton, J. M.; Ho, S. E Ff Ect of Conjugation Pathway in Metal-Free Room-Temperature Dual Singlet − Triplet Emitters for Organic Light-Emitting Diodes. **2016**. https://doi.org/10.1021/acs.jpclett.6b01907.

(40) An, Z.; Zheng, C.; Tao, Y.; Chen, R.; Shi, H.; Chen, T.; Wang, Z.; Li, H.; Deng, R.; Liu, X.; Huang, W. Stabilizing Triplet Excited States for Ultralong Organic Phosphorescence. **2015**, *14* (April). https://doi.org/10.1038/NMAT4259.

(41) Yang, Z.; Mao, Z.; Zhang, X.; Ou, D.; Mu, Y.; Zhang, Y.; Zhao, C.; Liu, S.; Chi, Z.; Xu, J.; Wu, Y.-C.; Lu, P.-Y.; Lien, A.; Bryce, M. R. Intermolecular Electronic Coupling of Organic Units for Efficient Persistent Room-Temperature Phosphorescence. *Angew. Chemie* **2016**, *128* (6), 2221–2225. https://doi.org/10.1002/ange.201509224.

(42) Xue, P.; Wang, P.; Chen, P.; Yao, B.; Gong, P.; Sun, J.; Zhang, Z.; Lu, R. Bright Persistent Luminescence from Pure Organic Molecules through a Moderate Intermolecular Heavy Atom Effect. *Chem. Sci.* **2017**, *8* (9), 6060–6065. https://doi.org/10.1039/c5sc03739e.

(43) Wang, H.; Wang, H.; Yang, X.; Wang, Q.; Yang, Y. Ion-Unquenchable and Thermally "on-Off" Reversible Room Temperature Phosphorescence of 3-Bromoquinoline Induced by Supramolecular Gels. *Langmuir* **2015**, *31* (1), 486–491. https://doi.org/10.1021/la5040323.

(44) Gong, Y.; Zhao, L.; Peng, Q.; Fan, D.; Yuan, W. Z.; Zhang, Y.; Tang, B. Z. Crystallization-Induced Dual Emission from Metal- and Heavy Atom-Free Aromatic Acids and Esters. *Chem. Sci.* **2015**, *6* (8), 4438–4444. https://doi.org/10.1039/c5sc00253b.

(45) Bergamini, G.; Fermi, A.; Botta, C.; Giovanella, U.; Di, S.; Negri, F.; Peresutti, R.; De, D. M. G.; Ceroni, P. A Persulfurated Benzene Molecule Exhibits Outstanding Phosphorescence in Rigid Environments : From Computational Study to Organic Nanocrystals and OLED Applications †. **2013**. https://doi.org/10.1039/c3tc00878a.

(46) Yang, L.; Wang, X.; Zhang, G.; Chen, X.; Zhang, G.; Jiang, J. Aggregation-Induced Intersystem Crossing: A Novel Strategy for Efficient Molecular Phosphorescence. *Nanoscale* **2016**, *8* (40), 17422–17426. https://doi.org/10.1039/c6nr03656b.

(47) Li, Q.; Zhou, M.; Yang, Q.; Wu, Q.; Shi, J.; Gong, A.; Yang, M. E Ffi Cient Room-Temperature Phosphorescence from Nitrogen-Doped Carbon Dots in Composite Matrices. **2016**. https://doi.org/10.1021/acs.chemmater.6b03049.

(48) Deng, Y.; Zhao, D.; Chen, X.; Wang, F.; Song, H.; Shen, D. Long Lifetime Pure Organic Phosphorescence Based on Water Soluble Carbon Dots. *Chem. Commun.* **2013**, *49* (51), 5751–5753. https://doi.org/10.1039/c3cc42600a.

(49) Dong, X.; Wei, L.; Su, Y.; Li, Z.; Geng, H.; Yang, C.; Zhang, Y. Efficient Long Lifetime

Room Temperature Phosphorescence of Carbon Dots in a Potash Alum Matrix. *J. Mater. Chem. C* **2015**, *3* (12), 2798–2801. https://doi.org/10.1039/c5tc00126a.

(50) Liu, W.; Li, C.; Ren, Y.; Sun, X.; Pan, W.; Li, Y.; Wang, J.; Wang, W. Carbon Dots: Surface Engineering and Applications. *J. Mater. Chem. B* **2016**, *4* (35), 5772–5788. https://doi.org/10.1039/c6tb00976j.

(51) Yang, S.; Wang, X.; Wang, H.; Lu, F.; Luo, P. G.; Cao, L.; Meziani, M. J.; Liu, J.; Liu, Y.; Chen, M.; Huang, Y.; Sun, Y. Carbon Dots as Nontoxic and High-Performance Fluorescence Imaging Agents. **2009**, 18110–18114.

(52) Chong, Y.; Ma, Y.; Shen, H.; Tu, X.; Zhou, X.; Xu, J.; Dai, J.; Fan, S.; Zhang, Z. Biomaterials The in Vitro and in Vivo Toxicity of Graphene Quantum Dots. **2014**, *35*. https://doi.org/10.1016/j.biomaterials.2014.03.021.

(53) Baker, S. N.; Baker, G. A. Luminescent Carbon Nanodots : Emergent Nanolights Angewandte. **2010**, 6726–6744. https://doi.org/10.1002/anie.200906623.

(54) Shen, J.; Zhu, Y.; Yang, X.; Li, C. ChemComm Graphene Quantum Dots : Emergent Nanolights for Bioimaging , Sensors , Catalysis and Photovoltaic Devices. **2012**, 3686–3699. https://doi.org/10.1039/c2cc00110a.

(55) Environ, E. Environmental Science Graphene Quantum Dots : An Emerging Material for Energy-Related Applications and Beyond. **2012**, 8869–8890. https://doi.org/10.1039/c2ee22982j.

(56) Sun, Y.; Zhou, B.; Lin, Y.; Wang, W.; Fernando, K. A. S.; Pathak, P.; Meziani, M. J.; Harruff, B. A.; Wang, X.; Wang, H.; Luo, P. G.; Yang, H.; Kose, M. E.; Chen, B.; Veca, L. M.; Xie, S.; Carolina, S. Quantum-Sized Carbon Dots for Bright and Colorful Photoluminescence. **2006**, No. Figure 2, 7756–7757. https://doi.org/10.1021/ja062677d.

(57) Xu, Q.; Liu, Y.; Gao, C.; Wei, J.; Zhou, H.; Chen, Y.; Dong, C.; Sreeprasad, T. S.; Li, N.; Xia, Z. Synthesis, Mechanistic Investigation, and Application of Photoluminescent Sulfur and Nitrogen Co-Doped Carbon Dots. *J. Mater. Chem. C* **2015**. https://doi.org/10.1039/C5TC01912E.

(58) Chem, J. M.; Wang, X.; Qu, K.; Xu, B.; Qu, X. Microwave Assisted One-Step Green Synthesis of Cell-Permeable Multicolor Photoluminescent Carbon Dots without Surface Passivation Reagents. **2011**, 2445–2450. https://doi.org/10.1039/c0jm02963g.

(59) Online, V. A. Investigation from Chemical Structure to Photoluminescent Mechanism : A Type of Carbon Dots from the Pyrolysis of Citric Acid and An. **2015**. https://doi.org/10.1039/C5TC00813A.

(60) Qu, D.; Zheng, M.; Zhang, L.; Zhao, H.; Xie, Z.; Jing, X.; Haddad, R. E. Formation Mechanism and Optimization of Highly Luminescent N-Doped Graphene. **2014**, 1–9. https://doi.org/10.1038/srep05294.

(61) Li, X.; Zhang, S.; Kulinich, S. A.; Liu, Y.; Zeng, H. Engineering Surface States of Carbon Dots to Achieve Controllable Luminescence for Solid-Luminescent

Composites and Sensitive Be 2 1 Detection. **2014**, 1–8. https://doi.org/10.1038/srep04976.

(62) Zhou, M.; Zhou, Z.; Gong, A.; Zhang, Y.; Li, Q. Synthesis of Highly Photoluminescent Carbon Dots via Citric Acid and Tris for Iron(III) Ions Sensors and Bioimaging. *Talanta* **2015**, *143*, 107–113. https://doi.org/10.1016/j.talanta.2015.04.015.

(63) Ogi, T.; Iwasaki, H.; Aishima, K.; Iskandar, F.; Wang, W. N.; Takimiya, K.; Okuyama, K. Transient Nature of Graphene Quantum Dot Formation via a Hydrothermal Reaction. *RSC Adv.* **2014**, *4* (99), 55709–55715. https://doi.org/10.1039/c4ra09159k.

(64) Hao, Y. N.; Guo, H. L.; Tian, L.; Kang, X. Enhanced Photoluminescence of Pyrrolic-Nitrogen Enriched Graphene Quantum Dots. *RSC Adv.* **2015**, *5* (54), 43750–43755. https://doi.org/10.1039/c5ra07745a.

(65) Yuan, F.; Wang, Z.; Li, X.; Li, Y.; Tan, Z.; Fan, L.; Yang, S. Bright Multicolor Bandgap Fluorescent Carbon Quantum Dots for Electroluminescent Light-Emitting Diodes. *Adv. Mater.* **2017**, *29* (3). https://doi.org/10.1002/adma.201604436.

(66) Chen, D.; Gao, H.; Chen, X.; Fang, G.; Yuan, S.; Yuan, Y. Excitation-Independent Dual-Color Carbon Dots: Surface-State Controlling and Solid-State Lighting. *ACS Photonics* **2017**, *4* (9), 2352–2358. https://doi.org/10.1021/acsphotonics.7b00675.

(67) Chen, J.; Wei, J. S.; Zhang, P.; Niu, X. Q.; Zhao, W.; Zhu, Z. Y.; Ding, H.; Xiong, H. M. Red-Emissive Carbon Dots for Fingerprints Detection by Spray Method: Coffee Ring Effect and Unquenched Fluorescence in Drying Process. *ACS Appl. Mater. Interfaces* **2017**, *9* (22), 18429–18433. https://doi.org/10.1021/acsami.7b03917.

(68) Jiang, K.; Sun, S.; Zhang, L.; Lu, Y.; Wu, A.; Cai, C.; Lin, H. Red, Green, and Blue Luminescence by Carbon Dots: Full-Color Emission Tuning and Multicolor Cellular Imaging**. **2015**, 1–5. https://doi.org/10.1002/anie.201501193.

(69) Ding, H.; Yu, S. B.; Wei, J. S.; Xiong, H. M. Full-Color Light-Emitting Carbon Dots with a Surface-State-Controlled Luminescence Mechanism. *ACS Nano* **2016**, *10* (1), 484–491. https://doi.org/10.1021/acsnano.5b05406.

(70) Wang, W.; Damm, C.; Walter, J.; Nacken, T. J.; Peukert, W. Photobleaching and Stabilization of Carbon Nanodots Produced by Solvothermal Synthesis. *Phys. Chem. Chem. Phys.* **2016**, *18* (1), 466–475. https://doi.org/10.1039/c5cp04942c.

(71) Shang, W.; Zhang, X.; Zhang, M.; Fan, Z.; Sun, Y. The Uptake Mechanism and Biocompatibility of Graphene Quantum Dots with Human Neural Stem Cells. **2014**, 5799–5806. https://doi.org/10.1039/c3nr06433f.

(72) Gui, R.; Jin, H.; Wang, Z.; Zhang, F.; Xia, J.; Yang, M.; Bi, S.; Xia, Y. Dots and Graphene Oxide †. **2015**. https://doi.org/10.1039/c4nr07620f.

(73) Jiang, K.; Zhang, L.; Lu, J.; Xu, C.; Cai, C.; Lin, H. Triple-Mode Emission of Carbon Dots: Applications for Advanced Anti-Counterfeiting. *Angew. Chemie* **2016**, *128* (25), 7347–7351. https://doi.org/10.1002/ange.201602445.

(74) Wang, L.; Zhang, H.; Zhou, X.; Liu, Y.; Lei, B. Journal of Colloid and Interface Science

Preparation , Characterization and Oxygen Sensing Properties of Luminescent Carbon Dots Assembled Mesoporous Silica Microspheres. *J. Colloid Interface Sci.* **2016**, *478*, 256–262. https://doi.org/10.1016/j.jcis.2016.06.026.

(75) Tan, J.; Zhang, J.; Li, W.; Zhang, L.; Yue, D. Synthesis of Amphiphilic Carbon Quantum Dots with Phosphorescence Properties and Their Multifunctional Applications. *J. Mater. Chem. C* **2016**, *4* (42), 10146–10153. https://doi.org/10.1039/c6tc03027k.

(76) Kwak, J. S.; Choi, Y. G. Oxygen Sensitivity of Photoluminescence Intensity of Pt Complex Dispersed in Fluorinated Acrylate for Pressure Sensitive Paint Applications. *Electron. Mater. Lett.* **2014**, *10* (5), 991–995. https://doi.org/10.1007/s13391-014-4100-z.

(77) Zhang, K.; Zhang, H.; Wang, Y.; Tian, Y.; Zhao, J.; Li, Y. High Sensitivity and Accuracy Dissolved Oxygen (DO) Detection by Using PtOEP/Poly(MMA-Co-TFEMA) Sensing Film. *Spectrochim. Acta - Part A Mol. Biomol. Spectrosc.* **2017**, *170*, 242–246. https://doi.org/10.1016/j.saa.2016.07.028.

(78) Zaitsev, N. K.; Melnikov, P. V.; Alferov, V. A.; Kopytin, A. V.; German, K. E. Stable Optical Oxygen Sensing Material Based on Perfluorinated Polymer and Fluorinated Platinum(II) and Palladium(II) Porphyrins. *Procedia Eng.* **2016**, *168*, 309–312. https://doi.org/10.1016/j.proeng.2016.11.203.

(79) Gillanders, R. N.; Tedford, M. C.; Crilly, P. J.; Bailey, R. T. Erythrosin B Encapsulated in a Fluoropolymer Matrix for Dissolved Oxygen Optical Sensing in Aggressive Aqueous Environments. *J. Photochem. Photobiol. A Chem.* **2004**, *162* (2–3), 531–535. https://doi.org/10.1016/S1010-6030(03)00417-9.

(80) Gillanders, R. N.; Tedford, M. C.; Crilly, P. J.; Bailey, R. T. A Composite Thin Film Optical Sensor for Dissolved Oxygen in Contaminated Aqueous Environments. *Anal. Chim. Acta* **2005**, *545* (2), 189–194. https://doi.org/10.1016/j.aca.2005.04.086.

(81) Lehner, P.; Larndorfer, C.; Garcia-Robledo, E.; Larsen, M.; Borisov, S. M.; Revsbech, N. P.; Glud, R. N.; Canfield, D. E.; Klimant, I. LUMOS - A Sensitive and Reliable Optode System for Measuring Dissolved Oxygen in the Nanomolar Range. *PLoS One* **2015**, *10* (6), 1–15. https://doi.org/10.1371/journal.pone.0128125.

(82) Kocincova, A. S.; Borisov, S. M.; Krause, C.; Wolfbeis, O. S. Fiber-Optic Microsensors for Simultaneous Sensing of Oxygen and PH, and of Oxygen and Temperature. *Anal. Chem.* **2007**, *79* (22), 8486–8493. https://doi.org/10.1021/ac070514h.

(83) Lamprecht, B.; Tschepp, A.; Čajlaković, M.; Sagmeister, M.; Ribitsch, V.; Köstler, S. A Luminescence Lifetime-Based Capillary Oxygen Sensor Utilizing Monolithically Integrated Organic Photodiodes. *Analyst* **2013**, *138* (20), 5875–5878. https://doi.org/10.1039/c3an00208j.

(84) Quaranta, M.; Murkovic, M.; Klimant, I. A New Method to Measure Oxygen Solubility in Organic Solvents through Optical Oxygen Sensing. *Analyst* **2013**, *138* (21), 6243–6245. https://doi.org/10.1039/c3an36782g.

(85) Chen, R.; Formenti, F.; McPeak, H.; Obeid, A. N.; Hahn, C.; Farmery, A. Experimental

Investigation of the Effect of Polymer Matrices on Polymer Fibre Optic Oxygen Sensors and Their Time Response Characteristics Using a Vacuum Testing Chamber and a Liquid Flow Apparatus. *Sensors Actuators, B Chem.* **2016**, *222*, 531–535. https://doi.org/10.1016/j.snb.2015.08.095.

(86) MacCraith, B. D.; McDonagh, C. M.; O'Keeffe, G.; Keyes, E. T.; Vos, J. G.; O'Kelly, B.; McGilp, J. F. Fibre Optic Oxygen Sensor Based on Fluorescence Quenching of Evanescent-Wave Excited Ruthenium Complexes in Sol-Gel Derived Porous Coatings. *Analyst* **1993**, *4* (118), 385–388. https://doi.org/10.1039/AN9931800385.

(87) Code, F.; Craith, B. D. M. A. C.; Mcdonagh, C.; Keeffe, G. O.; Butler, T. Fibre Optic C h e m i c a l Sensors Based on E v a n e s c e n t Wave Interactions in Sol-Gel-Derived Porous Coatings. **1994**, *665*, 661–665.

(88) Kiernan, P.; Mcdonagh, C.; Maccraith, B. D.; Mongey, K. Ruthenium-Doped Sol-Gel Derived Silica Films: Oxygen Sensitivity of Optical Decay Times - Code: EP4. *J. Sol-Gel Sci. Technol.* **1994**, *2* (1–3), 513–517. https://doi.org/10.1007/BF00486300.

(89) Kuncová, G.; Fialová, M. Optical Oxygen Sensor Based on Metallo-Organic Compound Immobilized by Sol-Gel Technique. *Biotechnol. Tech.* **1995**, *9* (3), 175–178. https://doi.org/10.1007/BF00157074.

(90) Lee, S. K.; Okura, I. Optical Sensor for Oxygen Using a Porphyrin-Doped Sol-Gel Glass. *Analyst* **1997**, *122* (1), 81–84. https://doi.org/10.1039/a604885d.

(91) Lee, S. K.; Okura, I. Porphyrin-Doped Sol-Gel Glass as a Probe for Oxygen Sensing. *Anal. Chim. Acta* **1997**, *342* (2–3), 181–188. https://doi.org/10.1016/S0003-2670(96)00562-4.

(92) Basu, B. J.; Kamble, J. Studies on the Oxygen Sensitivity and Microstructure of Sol-Gel Based Organic-Inorganic Hybrid Coatings Doped with Platinum Porphyrin Dye. *J. Sol-Gel Sci. Technol.* **2009**, *52* (1), 24–30. https://doi.org/10.1007/s10971-009-1996-0.

(93) Zaharieva, J.; Milanova, M.; Todorovsky, D. SiO2/Polyester Hybrid for Immobilization of Ru(Ii) Complex as Optical Gas-Phase Oxygen Sensor. *J. Mater. Chem.* **2011**, *21* (13), 4893–4903. https://doi.org/10.1039/c0jm03169k.

(94) Costa-Fernández, J. M.; Diaz-García, M. E.; Sanz-Medel, A. Sol-Gel Immobilized Room-Temperature Phosphorescent Metal-Chelate as Luminescent Oxygen Sensing Material. *Anal. Chim. Acta* **1998**, *360* (1–3), 17–26. https://doi.org/10.1016/S0003-2670(98)00022-1.

(95) Costa-Fernández, J. M.; Bordel, N.; Campo, J. C.; Ferrero, F. J.; Pérez, M. A.; Sanz-Medel, A. Portable Fibre Optic Oxygen Sensor Based on Room-Temperature Phosphorescence Lifetime. *Mikrochim. Acta* **2000**, *134* (3–4), 145–152. https://doi.org/10.1007/s006040070030.

(96) García, E. A.; Fernández, R. G.; Díaz-García, M. E. Tris(Bipyridine)Ruthenium(II) Doped Sol-Gel Materials for Oxygen Recognition in Organic Solvents. *Microporous Mesoporous Mater.* **2005**, *77* (2–3), 235–239. https://doi.org/10.1016/j.micromeso.2004.09.004.

(97) Wolfbeis, O. S. Fiber-Optic Chemical Sensors and Bio-Sensors. *Anal. Chem.* **2006**, *78*, 3859–3874. https://doi.org/10.3390/s151025208.

(98) Banerjee, S.; Kelly, C.; Kerry, J. P.; Papkovsky, D. B. High Throughput Non-Destructive Assessment of Quality and Safety of Packaged Food Products Using Phosphorescent Oxygen Sensors. *Trends Food Sci. Technol.* **2016**, *50*, 85–102. https://doi.org/10.1016/j.tifs.2016.01.021.

(99) Borisov, S. M.; Zenkl, G.; Klimant, I. Phosphorescent Platinum(II) and Palladium(II) Complexes with Azatetrabenzoporphyrinss New-Red Laser Diode-Compatible Indicators for Optical Oxygen Sensing. *ACS Appl. Mater. Interfaces* **2010**, *2* (2), 366–374. https://doi.org/10.1021/am900932z.

(100) Borisov, S. M.; Fischer, R.; Saf, R.; Klimant, I. Exceptional Oxygen Sensing Properties of New Blue Light-Excitable Highly Luminescent Europium(III) and Gadolinium(III) Complexes. *Adv. Funct. Mater.* **2014**, *24* (41), 6548–6560. https://doi.org/10.1002/adfm.201401754.

(101) Borisov, S. M.; Borisov, S. M.; Klimant, I.; Klimant, I. Ultrabright Oxygen Sensors Based on Cyclometallated Iridium(Iii) Coumarin Complexes. *Anal. Chem.* **2007**, *2* (Iii), 7501–7509.

(102) Borisov, S. M.; Nuss, G.; Klimant, I. Red Light-Excitable Oxygen Sensing Materials Based on Platinum(II) and Palladium(II) Benzoporphyrins. *Anal. Chem.* **2008**, *80* (24), 9435–9442. https://doi.org/10.1021/ac801521v.

(103) Karakus, C.; Fischer, L. H.; Schmeding, S.; Hummel, J.; Risch, N.; Schäferling, M.; Holder, E. Oxygen and Temperature Sensitivity of Blue to Green to Yellow Light-Emitting Pt(II) Complexes. *Dalt. Trans.* **2012**, *41* (32), 9623–9632. https://doi.org/10.1039/C2DT30835E.

(104) Koren, K.; Borisov, S. M.; Saf, R.; Klimant, I. Strongly Phosphorescent Iridium(III)-Porphyrins - New Oxygen Indicators with Tuneable Photophysical Properties and Functionalities. *Eur. J. Inorg. Chem.* **2011**, No. 10, 1531–1534. https://doi.org/10.1002/ejic.201100089.

(105) Borisov, S. M.; Saf, R.; Fischer, R.; Klimant, I. Synthesis and Properties of New Phosphorescent Red Light-Excitable Platinum (II) and Palladium (II) Complexes with Schiff Bases for Oxygen Sensing and Triplet − Triplet Annihilation-Based Upconversion. *Inorg. Chem.* **2013**, *52* (Ii), 1206–1216. https://doi.org/10.1021/ic301440k.

(106) Borisov, S. M.; Alemayehu, A.; Ghosh, A. Osmium-Nitrido Corroles as NIR Indicators for Oxygen Sensors and Triplet Sensitizers for Organic Upconversion and Singlet Oxygen Generation. *J. Mater. Chem. C* **2016**, *5822* (4), 5822–5828. https://doi.org/10.1039/c6tc01126h.

(107) Palma, A. J.; Lopez-Gonzalez, J.; Asensio, L. J.; Fernandez-Ramos, M. D.; Capitan-Vallvey, L. F. Microcontroller-Based Portable Instrument for Stabilised Optical Oxygen Sensor. *Sensors Actuators, B Chem.* **2007**, *121* (2), 629–638. https://doi.org/10.1016/j.snb.2006.03.056.

(108) López-Ruiz, N.; Martínez-Olmos, A.; Pérez de Vargas-Sansalvador, I. M.; Fernández-Ramos, M. D.; Carvajal, M. A.; Capitan-Vallvey, L. F.; Palma, A. J. Determination of O2 Using Colour Sensing from Image Processing with Mobile Devices. *Sensors Actuators B Chem.* **2012**, *171*, 938–945. https://doi.org/10.1016/j.snb.2012.06.007.

(109) Shinar, R.; Ghosh, D.; Choudhury, B.; Noack, M.; Dalal, V. L.; Shinar, J. Luminescence-Based Oxygen Sensor Structurally Integrated with an Organic Light-Emitting Device Excitation Source and an Amorphous Si-Based Photodetector. *J. Non. Cryst. Solids* **2006**, *352* (9-20 SPEC. ISS.), 1995–1998. https://doi.org/10.1016/j.jnoncrysol.2005.12.029.

(110) Santoro, S.; Moro, A. J.; Portugal, C.; Crespo, J. G.; Lima, J. C.; Coelhoso, I. M. Monitoring Oxygen Permeation through Polymeric Packaging Films Using a Ratiometric Luminescent Sensor. *J. Food Eng.* **2016**, *189*, 37–44. https://doi.org/10.1016/j.jfoodeng.2016.05.020.

(111) Fernández-Sánchez, J. F.; Roth, T.; Cannas, R.; Nazeeruddin, M. K.; Spichiger, S.; Graetzel, M.; Spichiger-Keller, U. E. Novel Oxygen Sensitive Complexes for Optical Oxygen Sensing. *Talanta* **2007**, *71* (1), 242–250. https://doi.org/10.1016/j.talanta.2006.03.043.

(112) Escobedo, P.; Erenas, M. M.; López-Ruiz, N.; Carvajal, M. A.; Gonzalez-Chocano, S.; De Orbe-Payá, I.; Capitán-Valley, L. F.; Palma, A. J.; Martínez-Olmos, A. Flexible Passive near Field Communication Tag for Multigas Sensing. *Anal. Chem.* **2017**, *89* (3), 1697–1703. https://doi.org/10.1021/acs.analchem.6b03901.

(113) Koren, K.; Hutter, L.; Enko, B.; Pein, A.; Borisov, S. M.; Klimant, I. Tuning the Dynamic Range and Sensitivity of Optical Oxygen-Sensors by Employing Differently Substituted Polystyrene-Derivatives. *Sensors Actuators, B Chem.* **2013**, *176*, 344–350. https://doi.org/10.1016/j.snb.2012.09.057.

(114) Wang, X.; Wolfbeis, O. S. Optical Methods for Sensing and Imaging Oxygen: Materials, Spectroscopies and Applications. *Chem. Soc. Rev.* **2014**, *43* (10), 3666–3761. https://doi.org/10.1039/c4cs00039k.

(115) Borisov, S. M.; Klimant, I. New Luminescent Oxygen-Sensing and Temperature-Sensing Materials Based on Gadolinium(III) and Europium(III) Complexes Embedded in an Acridone-Polystyrene Conjugate. *Anal. Bioanal. Chem.* **2012**, *404* (10), 2797–2806. https://doi.org/10.1007/s00216-012-6244-8.

(116) Mak, C. S. K.; Pentlehner, D.; Stich, M.; Wolfbeis, O. S.; Chan, W. K.; Yersin, H. Exceptional Oxygen Sensing Capabilities and Triplet State Properties of Ir(Ppy-NPh 2) 3. *Chem. Mater.* **2009**, *21* (11), 2173–2175. https://doi.org/10.1021/cm9003678.

(117) Achatz, D. E.; Meier, R. J.; Fischer, L. H.; Wolfbeis, O. S. Luminescent Sensing of Oxygen Using a Quenchable Probe and Upconverting Nanoparticles. *Angew. Chemie - Int. Ed.* **2011**, *50* (1), 260–263. https://doi.org/10.1002/anie.201004902.

(118) Schroeder, C. R.; Neurauter, G.; Klimant, I. Luminescent Dual Sensor for Time-Resolved Imaging of PCO2 and PO2 in Aquatic Systems. *Microchim. Acta* **2007**, *158* (3–4), 205–218. https://doi.org/10.1007/s00604-006-0696-5.

(119) Douglas, P.; Eaton, K. Response Characteristics of Thin Film Oxygen Sensors , Pt and Pd Octaethylporphyrins in Polymer Films. *Sensors Actuators B* **2002**, *82* (2–3), 200–208.

(120) Ricketts, S. R.; Douglas, P. A Simple Colorimetric Luminescent Oxygen Sensor Using a Green LED with Pt Octaethylporphyrin in Ethyl Cellulose as the Oxygen-Responsive Element. *Sensors Actuators, B Chem.* **2008**, *135* (1), 46–51. https://doi.org/10.1016/j.snb.2008.07.017.

(121) Shen, L.; Ratterman, M.; Klotzkin, D.; Papautsky, I. A CMOS Optical Detection System for Point-of-Use Luminescent Oxygen Sensing. *Sensors Actuators, B Chem.* **2011**, *155* (1), 430–435. https://doi.org/10.1016/j.snb.2011.01.001.

(122) Baleiža, C.; Nagl, S.; Schäferling, M.; Berberan-Santos, M. N.; Wolfbeis, O. S. Dual Fluorescence Sensor for Trace Oxygen and Temperature with Unmatched Range and Sensitivity. *Anal. Chem.* **2008**, *80* (16), 6449–6457. https://doi.org/10.1021/ac801034p.

(123) Eaton, K.; Douglas, P. Effect of Humidity on the Response Characteristics of Luminescent PtOEP Thin ® Lm Optical Oxygen Sensors. *Sensors Actuators B. Chem.* **2002**, *82*, 94–104.

(124) Badocco, D.; Mondin, A.; Pastore, P.; Voltolina, S.; Gross, S. Dependence of Calibration Sensitivity of a Polysulfone/Ru(II)-Tris(4,7-Diphenyl-1,10-Phenanthroline)-Based Oxygen Optical Sensor on Its Structural Parameters. *Anal. Chim. Acta* **2008**, *627* (2), 239–246. https://doi.org/10.1016/j.aca.2008.08.019.

(125) Banerjee, S.; Kuznetsova, R. T.; Papkovsky, D. B. Solid-State Oxygen Sensors Based on Phosphorescent Diiodo-Borondipyrromethene Dye. *Sensors Actuators, B Chem.* **2015**, *212*, 229–234. https://doi.org/10.1016/j.snb.2015.02.016.

(126) Badocco, D.; Mondin, A.; Pastore, P. Determination of Thermodynamic Parameters from Light Intensity Signals Obtained from Oxygen Optical Sensors. *Sensors Actuators, B Chem.* **2012**, *163* (1), 165–170. https://doi.org/10.1016/j.snb.2012.01.030.

(127) Badocco, D.; Mondin, A.; Pastore, P. Rationalization of the Behaviour of a Bi-Label Oxygen Optical Sensor. *Sensors Actuators, B Chem.* **2011**, *158* (1), 54–61. https://doi.org/10.1016/j.snb.2011.05.024.

(128) Badocco, D.; Mondin, A.; Fusar, A.; Pastore, P. Calibration Models under Dynamic Conditions for Determining Molecular Oxygen with Embedded in Polymeric Matrixes. *J. Phys. Chem. C* **2009**, No. model III, 20467–20475.

(129) Voraberger, H. S.; Kreimaier, H.; Biebernik, K.; Kern, W. Novel Oxygen Optrode Withstanding Autoclavation: Technical Solutions and Performance. *Sensors Actuators, B Chem.* **2001**, *74* (1–3), 179–185. https://doi.org/10.1016/S0925-4005(00)00730-9.

(130) Borchert, N. B.; Ponomarev, G. V; Kerry, J. P.; Papkovsky, D. B.; Chemistry, B.; Pharmacy, C. O2 / PH Multisensor Based on One Phosphorescent Dye. *Anal. Chem.* **2011**, *83*, 18–22.

(131) Stubenrauch, K.; Sandholzer, M.; Niedermair, F.; Waich, K.; Mayr, T.; Klimant, I.; Trimmel, G.; Slugovc, C. Poly(Norbornene)s as Matrix Materials for Platinum Tetrakis(Pentafluorophenyl)Porphyrin Based Optical Oxygen Sensors. *Eur. Polym. J.* **2008**, *44* (8), 2558–2566. https://doi.org/10.1016/j.eurpolymj.2008.06.012.

(132) Pang, Z.; Gu, X. H.; Yekta, A.; Masoumi, Z.; Coll, J. B.; Winnik, M. A.; Manners, I. Phosphorescent Oxygen Sensors Utilizing Sulfur-Nitrogen-Phosphorus Polymer Matrices. *Adv. Mater.* **1996**, *8* (9), 768. https://doi.org/10.1002/adma.19960080916.

(133) Fischer, L. H.; Stich, M. I. J.; Wolfbeis, O. S.; Tian, N.; Holder, E.; Schäferling, M. Red-And Green-Emitting Iridium(III) Complexes for a Dual Barometric and Temperature-Sensitive Paint. *Chem. - A Eur. J.* **2009**, *15* (41), 10857–10863. https://doi.org/10.1002/chem.200901511.

(134) Xing, Y.; Liu, C.; Song, X.; Li, J. Photostable Trifluoromethyl-Substituted Platinum(Ii) Emitters for Continuous Monitoring of Molecular Oxygen. *J. Mater. Chem. C* **2015**, *3* (10), 2166–2174. https://doi.org/10.1039/c4tc02915a.

(135) Amao, Y.; Asai, K.; Okura, I.; Shinohara, H.; Nishide, H. Platinum Porphyrin Embedded in Poly(1-Trimethylsilyl-1-Propyne) Film as an Optical Sensor for Trace Analysis of Oxygen. *Analyst* **2000**, *125* (11), 1911–1914. https://doi.org/10.1039/b005838f.

(136) Matsuda, Y.; Nagashima, F.; Yamaguchi, H.; Egami, Y.; Niimi, T. Unsteady 2D Measurement of Dissolved Oxygen Distribution Using Luminescent Sensor Film. *Sensors Actuators, B Chem.* **2011**, *160* (1), 1464–1467. https://doi.org/10.1016/j.snb.2011.07.031.

(137) Amao, Y.; Miyashita, T.; Okura, I. Novel Optical Oxygen Sensing Material: Platinum Octaethylporphyrin Immobilized in a Copolymer Film of Isobutyl Methacrylate and Tetrafluoropropyl Methacrylate. *React. Funct. Polym.* **2001**, *47* (1), 49–54. https://doi.org/10.1016/S1381-5148(00)00070-5.

(138) Köse, M. E.; Carroll, B. F.; Schanze, K. S. Preparation and Spectroscopic Properties of Multiluminophore Luminescent Oxygen and Temperature Sensor Films. *Langmuir* **2005**, *21* (20), 9121–9129. https://doi.org/10.1021/la050997p.

(139) Khalil, G. E.; Coston, C.; Crafton, J.; Jones, G.; Grenoble, S.; Gouterman, M.; Callis, J. B.; Dalton, L. R. Dual-Luminophor Pressure-Sensitive Paint I. Ratio of Reference to Sensor Giving a Small Temperature Dependency. *Sensors Actuators, B Chem.* **2004**, *97* (1), 13–21. https://doi.org/10.1016/S0925-4005(03)00484-2.

(140) Obata, M.; Asato, R.; Mitsuo, K.; Hirohara, S. Radical Polymerization of Trifluoromethyl-Substituted Methyl Methacrylates and Their Application for Use in Pressure-Sensitive Paint. *J. Polym. Sci. Part A Polym. Chem.* **2014**, *52* (7), 963–972. https://doi.org/10.1002/pola.27076.

(141) Zhang, K.; Zhang, H.; Wang, Y.; Tian, Y.; Zhao, J.; Li, Y. High Sensitivity and Accuracy Dissolved Oxygen (DO) Detection by Using PtOEP/Poly(MMA-Co-TFEMA) Sensing Film. *Spectrochim. Acta - Part A Mol. Biomol. Spectrosc.* **2017**, *170*, 242–246. https://doi.org/10.1016/j.saa.2016.07.028.

(142) Lehner, P.; Staudinger, C.; Borisov, S. M.; Klimant, I. Ultra-Sensitive Optical Oxygen Sensors for Characterization of Nearly Anoxic Systems. *Nat. Commun.* **2014**, *5*, 4460. https://doi.org/10.1038/ncomms5460.

(143) Greiner, A.; Wendorff, J. H. Electrospinning: A Fascinating Method for the Preparation of Ultrathin Fibers. *Angew. Chemie Int. Ed.* **2007**, *46* (30), 5670–5703. https://doi.org/10.1002/anie.200604646.

(144) Wang, Y.; Li, B.; Zhang, L.; Zuo, Q.; Li, P.; Zhang, J.; Su, Z. High-Performance Oxygen Sensors Based on EuIII Complex/Polystyrene Composite Nanofibrous Membranes Prepared by Electrospinning. *Chem Commun* **2011**, *12* (39), 5868–5870. https://doi.org/10.1002/cphc.201000884.

(145) Yingkui, L. High Performance Oxygen Sensing Nanofibrous Membranes of Eu(III) Complex/Polystyrene Prepared by Electrospinning. *Spectrochim. Acta - Part A Mol. Biomol. Spectrosc.* **2011**, *79* (2), 356–360. https://doi.org/10.1016/j.saa.2011.03.012.

(146) Kai, R.; Jun, W.; Huali, J. Electrospinning Fibrous Films Doped with Iridium Complexes for High Performance Oxygen Sensing: Synthesis and Characterization. *Sensors Actuators, B Chem.* **2017**, *240*, 697–708. https://doi.org/10.1016/j.snb.2016.09.033.

(147) Songzhu, L.; Xiangting, D.; Jinxian, W.; Guixia, L.; Wenshen, Y.; Ruokun, J. Fabrication of Eu(III) Complex Doped Nanofibrous Membranes and Their Oxygen-Sensing Properties. *Spectrochim. Acta - Part A Mol. Biomol. Spectrosc.* **2010**, *77* (4), 885–889. https://doi.org/10.1016/j.saa.2010.08.025.

(148) Wang, L. Y.; Xu, Y.; Lin, Z.; Zhao, N.; Xu, Y. Electrospinning Fabrication and Oxygen Sensing Properties of Cu(I) Complexpolystyrene Composite Microfibrous Membranes. *J. Lumin.* **2011**, *131* (7), 1277–1282. https://doi.org/10.1016/j.jlumin.2011.03.017.

(149) Wolf, C.; Tscherner, M.; Köstler, S. Ultra-Fast Opto-Chemical Sensors by Using Electrospun Nanofibers as Sensing Layers. *Sensors Actuators, B Chem.* **2015**, *209*, 1064–1069. https://doi.org/10.1016/j.snb.2014.11.070.

(150) Xu, G.; Lu, M.; Huang, C.; Wang, Y.; Ge, S. Study on an Oxygen Sensing Rhenium(I) Complex with Enlarged Sensing/Active Area: Fabrication, Photophysical Parameters and Molecular Oxygen Sensing Performance. *Spectrochim. Acta - Part A Mol. Biomol. Spectrosc.* **2014**, *123*, 369–375. https://doi.org/10.1016/j.saa.2013.12.055.

(151) Wang, C. E. An Oxygen-Sensing Rhenium(I) Complex with a Carbazole "Shield" in Its Diamine Ligand: Synthesis, Characterization, Photophysical Property and Sensing Performance. *J. Lumin.* **2014**, *145*, 531–538. https://doi.org/10.1016/j.jlumin.2013.08.035.

(152) Ongun, M. Z.; Oter, O.; Sabanci, G.; Ertekin, K.; Celik, E. Enhanced Stability of Ruthenium Complex in Ionic Liquid Doped Electrospun Fibers. *Sensors Actuators, B Chem.* **2013**, *183*, 11–19. https://doi.org/10.1016/j.snb.2013.03.060.

(153) Jiang, Z.; Yu, X.; Zhai, S.; Hao, Y. Ratiometric Dissolved Oxygen Sensors Based on Ruthenium Complex Doped with Silver Nanoparticles. *Sensors* **2017**, *17* (3), 548.

https://doi.org/10.3390/s17030548.

(154) Xue, R.; Behera, P.; Xu, J.; Viapiano, M. S.; Lannutti, J. J. Polydimethylsiloxane Core-Polycaprolactone Shell Nanofibers as Biocompatible, Real-Time Oxygen Sensors. *Sensors Actuators, B Chem.* **2014**, *192*, 697–707. https://doi.org/10.1016/j.snb.2013.10.084.

(155) Presley, K. F.; Cheong, S.; Cochran, A.; Tilley, R. D.; Collins, J. E.; Lannutti, J. J. Upconverter-Powered Oxygen Sensing in Electrospun Polymeric Bilayers. *Sensors Actuators, B Chem.* **2016**, *235*, 197–205. https://doi.org/10.1016/j.snb.2016.04.182.

(156) Wang, X.; Wolfbeis, O. S. Optical Methods for Sensing and Imaging Oxygen: Materials, Spectroscopies and Applications. *Chem. Soc. Rev.* **2014**, *43* (10), 3666–3761. https://doi.org/10.1039/c4cs00039k.

(157) *Quenched-Phosphorescence Detection of Molecular Oxygen*; Papkovsky, D. B., Dmitriev, R. I., Eds.; Detection Science; The Royal Society of Chemistry, 2018. https://doi.org/10.1039/9781788013451.

(158) Armagan, E.; Papkovsky, D. B.; Toncelli, C. *CHAPTER 2: New Polymer-Based Sensor Materials and Fabrication Technologies for Large-Scale Applications*; 2018. https://doi.org/10.1039/9781788013451-00019.

(159) Quaranta, M.; Borisov, S. M.; Klimant, I. Indicators for Optical Oxygen Sensors. **2012**, No. November, 115–157. https://doi.org/10.1007/s12566-012-0032-y.

(160) Toncelli, C.; Arzhakova, O. V.; Dolgova, A.; Volynskii, A. L.; Bakeev, N. F.; Kerry, J. P.; Papkovsky, D. B. Oxygen-Sensitive Phosphorescent Nanomaterials Produced from High-Density Polyethylene Films by Local Solvent-Crazing. *Anal. Chem.* **2014**, *86* (3). https://doi.org/10.1021/ac404072z.

(161) Toncelli, C.; Arzhakova, O. V.; Dolgova, A.; Volynskii, A. L.; Kerry, J. P.; Papkovsky, D. B. Phosphorescent Oxygen Sensors Produced by Spot-Crazing of Polyphenylenesulfide Films. *J. Mater. Chem. C* **2014**, *2* (38). https://doi.org/10.1039/c4tc01390e.

(162) Kelly, C. A.; Toncelli, C.; Kerry, J. P.; Papkovsky, D. B. Discrete O2 Sensors Produced by a Spotting Method on Polyolefin Fabric Substrates. *Sensors Actuators, B Chem.* **2014**, *203*. https://doi.org/10.1016/j.snb.2014.06.103.

(163) Kelly, C. A.; Toncelli, C.; Cruz-Romero, M.; Arzhakova, O. V.; Kerry, J. P.; Papkovsky, D. B. Phosphorescent O<Inf>2</Inf> Sensors Integrated in Polymeric Film Materials by Local Solvent Crazing. *Mater. Des.* **2015**, *77*. https://doi.org/10.1016/j.matdes.2015.03.045.

(164) Kwon, M. S.; Lee, D.; Seo, S.; Jung, J.; Kim, J. Tailoring Intermolecular Interactions for Efficient Room-Temperature Phosphorescence from Purely Organic Materials in Amorphous Polymer Matrices. *Angew. Chemie - Int. Ed.* **2014**, *53* (42), 11177–11181. https://doi.org/10.1002/anie.201404490.

(165) Yuan, W. Z.; Shen, X. Y.; Zhao, H.; Lam, J. W. Y.; Tang, L.; Lu, P.; Wang, C.; Liu, Y.; Wang, Z.; Zheng, Q.; Sun, J. Z.; Ma, Y.; Tang, B. Z. Crystallization-Induced

Phosphorescence of Pure Organic Luminogens at Room Temperature. **2010**, 6090–6099.

(166) Siloxy Group-Induced Highly Efficient Room Temperature Phosphorescence with Long Lifetime. **2016**. https://doi.org/10.1021/acs.jpcc.6b03276.

(167) Gong, Y.; Zhao, L.; Peng, Q.; Fan, D.; Yuan, W. Z.; Zhang, Y.; Tang, B. Z. Crystallization-Induced Dual Emission from Metal- and Heavy Atom-Free Aromatic Acids and Esters. *Chem. Sci.* **2015**, *6* (8), 4438–4444. https://doi.org/10.1039/C5SC00253B.

(168) Yang, L.; Wang, X.; Zhang, G.; Chen, X.; Zhang, G.; Jiang, J. Aggregation-Induced Intersystem Crossing: A Novel Strategy for Efficient Molecular Phosphorescence. *Nanoscale* **2016**, *8*, 17422–17426. https://doi.org/10.1039/C6NR03656B.

(169) Chen, H.; Ma, X.; Wu, S.; Tian, H. A Rapidly Self-Healing Supramolecular Polymer Hydrogel with Photostimulated Room-Temperature Phosphorescence Responsiveness. *Angew. Chemie Int. Ed.* **2014**, *53* (51), 14149–14152. https://doi.org/10.1002/anie.201407402.

(170) Kwon, M. S.; Yu, Y.; Coburn, C.; Phillips, A. W.; Chung, K.; Shanker, A.; Jung, J.; Kim, G.; Pipe, K.; Forrest, S. R.; Youk, J. H.; Gierschner, J.; Kim, J. Suppressing Molecular Motions for Enhanced Room-Temperature Phosphorescence of Metal-Free Organic Materials. *Nat. Commun.* **2015**, *6*, 8947. https://doi.org/10.1038/ncomms9947.

(171) Deng, Y.; Zhao, D.; Chen, X.; Wang, F.; Song, H.; Shen, D. Long Lifetime Pure Organic Phosphorescence Based on Water Soluble Carbon Dots. *Chem. Commun. (Camb).* **2013**, *49* (51), 5751–5753. https://doi.org/10.1039/c3cc42600a.

(172) Tan, J.; Zhang, J.; Li, W.; Zhang, L.; Yue, D. Synthesis of Amphiphilic Carbon Quantum Dots with Phosphorescence Properties and Their Multifunctional Applications. *J. Mater. Chem. C* **2016**, *4*, 10146–10153. https://doi.org/10.1039/C6TC03027K.

(173) Tan, J.; Zou, R.; Zhang, J.; Li, W.; Zhang, L.; Yue, D. Large-Scale Synthesis of N-Doped Carbon Quantum Dots and Their Phosphorescence Properties in a Polyurethane Matrix. *Nanoscale* **2016**, *8* (8), 4742–4747. https://doi.org/10.1039/C5NR08516K.

(174) Dong, X.; Wei, L.; Su, Y.; Li, Z.; Geng, H.; Yang, C.; Zhang, Y. Efficient Long Lifetime Room Temperature Phosphorescence of Carbon Dots in a Potash Alum Matrix. *J. Mater. Chem. C* **2015**, *3*, 2798–2801. https://doi.org/10.1039/C5TC00126A.

(175) Li, Q.; Zhou, M.; Yang, Q.; Wu, Q.; Shi, J.; Gong, A.; Yang, M. E Ffi Cient Room-Temperature Phosphorescence from Nitrogen-Doped Carbon Dots in Composite Matrices. **2016**. https://doi.org/10.1021/acs.chemmater.6b03049.

(176) Tao, S.; Lu, S.; Geng, Y.; Zhu, S.; Redfern, S. A. T.; Song, Y.; Feng, T.; Xu, W.; Yang, B. Design of Metal-Free Polymer Carbon Dots: A New Class of Room-Temperature Phosphorescent Materials. *Angew. Chemie* **2018**, *130* (9), 2417–2422. https://doi.org/10.1002/ange.201712662.

(177) Lei, B.; Wang, L.; Zhang, H.; Liu, Y.; Dong, H.; Zheng, M.; Zhou, X. Luminescent Carbon Dots Assembled SBA-15 and Its Oxygen Sensing Properties. *Sensors Actuators B Chem.* **2016**, *230*, 101–108. https://doi.org/https://doi.org/10.1016/j.snb.2016.01.037.

(178) Wang, L.; Zhang, H.; Zhou, X.; Liu, Y.; Lei, B. Journal of Colloid and Interface Science Preparation , Characterization and Oxygen Sensing Properties of Luminescent Carbon Dots Assembled Mesoporous Silica Microspheres. *J. Colloid Interface Sci.* **2016**, *478*, 256–262. https://doi.org/10.1016/j.jcis.2016.06.026.

(179) Chen, J.; Wei, J. S.; Zhang, P.; Niu, X. Q.; Zhao, W.; Zhu, Z. Y.; Ding, H.; Xiong, H. M. Red-Emissive Carbon Dots for Fingerprints Detection by Spray Method: Coffee Ring Effect and Unquenched Fluorescence in Drying Process. *ACS Appl. Mater. Interfaces* **2017**, *9* (22), 18429–18433. https://doi.org/10.1021/acsami.7b03917.

(180) Chen, D.; Gao, H.; Chen, X.; Fang, G.; Yuan, S.; Yuan, Y. Excitation-Independent Dual-Color Carbon Dots: Surface-State Controlling and Solid-State Lighting. *ACS Photonics* **2017**, *4* (9), 2352–2358. https://doi.org/10.1021/acsphotonics.7b00675.

(181) Jiang, K.; Zhang, L.; Lu, J.; Xu, C.; Cai, C.; Lin, H. Triple-Mode Emission of Carbon Dots: Applications for Advanced Anti-Counterfeiting. *Angew. Chemie Int. Ed.* **2016**, *55* (25), 7231–7235. https://doi.org/10.1002/anie.201602445.

(182) Cabrerizo, F. M.; Arnbjerg, J.; Denofrio, M. P.; Erra-Balsells, R.; Ogilby, P. R. Fluorescence Quenching by Oxygen: "Debunking" a Classic Rule. *ChemPhysChem* **2010**, *11* (4), 796–798. https://doi.org/10.1002/cphc.201000002.

(183) Kikuchi, K.; Sato, C.; Watabe, M.; Ikeda, H.; Takahashi, Y.; Miyashi, T. New Aspects on Fluorescence Quenching by Molecular Oxygen. *J. Am. Chem. Soc.* **1993**, *115* (12), 5180–5184. https://doi.org/10.1021/ja00065a033.

(184) Abdel-Shafi, A. A.; Wilkinson, F. Charge Transfer Effects on the Efficiency of Singlet Oxygen Production Following Oxygen Quenching of Excited Singlet and Triplet States of Aromatic Hydrocarbons in Acetonitrile. *J. Phys. Chem. A* **2000**, *104* (24), 5747–5757. https://doi.org/10.1021/jp0000432.

(185) Erickson, H. P. Size and Shape of Protein Molecules at the Nanometer Level Determined by Sedimentation, Gel Filtration, and Electron Microscopy. *Biol. Proced. Online* **2009**, *11* (1), 32–51. https://doi.org/10.1007/s12575-009-9008-x.

(186) Losito, I.; Palmisano, F.; Zambonin, P. G. O-Phenylenediamine Electropolymerization By Cyclic Voltammetry Combined With Electrospray Ionization-Ion Trap Mass Spectrometry. *Anal. Chem.* **2003**, *75* (19), 4988–4995. https://doi.org/10.1021/ac0342424.

(187) Keuleers, R.; Desseyn, H. O.; Rousseau, B.; Van Alsenoy, C. Vibrational Analysis of Urea. *J. Phys. Chem. A* **1999**, *103* (24), 4621–4630. https://doi.org/10.1021/jp984180z.

(188) Badawi, H. M.; Förner, W.; Ali, S. A. A Comparative Study of the Infrared and Raman Spectra of Aniline and O-, m-, p-Phenylenediamine Isomers. *Spectrochim. Acta - Part A Mol. Biomol. Spectrosc.* **2013**, *112*, 388–396.

https://doi.org/10.1016/j.saa.2013.04.075.

(189) Schaber, P. M.; Colson, J.; Higgins, S.; Thielen, D.; Anspach, B.; Brauer, J. Thermal Decomposition (Pyrolysis) of Urea in an Open Reaction Vessel. *Thermochim. Acta* **2004**, *424* (1), 131–142. https://doi.org/https://doi.org/10.1016/j.tca.2004.05.018.

(190) Martins, N. C. T.; Ângelo, J.; Girão, A. V.; Trindade, T.; Andrade, L.; Mendes, A. N-Doped Carbon Quantum Dots/TiO2 Composite with Improved Photocatalytic Activity. *Appl. Catal. B Environ.* **2016**, *193*, 67–74. https://doi.org/10.1016/j.apcatb.2016.04.016.

(191) Chen, X.; Zhang, J.; Ma, S.; Hu, H.; Zhou, Z. Microstructure, Mechanical, and Tribological Properties of CN Xthin Films Prepared by Reactive Magnetron Sputtering. *Acta Metall. Sin. (English Lett.* **2014**, *27* (1), 31–36. https://doi.org/10.1007/s40195-013-0004-4.

(192) Das, S. K.; Dickinson, C.; Lafir, F.; Brougham, D. F.; Marsili, E. Synthesis, Characterization and Catalytic Activity of Gold Nanoparticles Biosynthesized with Rhizopus Oryzae Protein Extract. *Green Chem.* **2012**, *14* (5), 1322–1334. https://doi.org/10.1039/c2gc16676c.

(193) Liu, J.; Zhang, T.; Wang, Z.; Dawson, G.; Chen, W. Simple Pyrolysis of Urea into Graphitic Carbon Nitride with Recyclable Adsorption and Photocatalytic Activity. *J. Mater. Chem.* **2011**, *21* (38), 14398–14401. https://doi.org/10.1039/c1jm12620b.

(194) Zhang, W.; Wang, S.; Ji, J.; Li, Y.; Zhang, G.; Zhang, F.; Fan, X. Primary and Tertiary Amines Bifunctional Graphene Oxide for Cooperative Catalysis. *Nanoscale* **2013**, *5* (13), 6030–6033. https://doi.org/10.1039/c3nr01323e.

(195) Ding, H.; Yu, S.; Wei, J.; Xiong, H. Full-Color Light-Emitting Carbon Dots with a Surface-State-Controlled Luminescence Mechanism. **2015**. https://doi.org/10.1021/acsnano.5b05406.

(196) Wei, Y.; Yang, C.; Ding, T. Tetrahedron Leuers,. *Science (80-.).* **1996**, *4039* (6), 731–734.

(197) Pham, Q. L.; Haldorai, Y.; Nguyen, V. H.; Tuma, D.; Shim, J. J. Facile Synthesis of Poly(p-Phenylenediamine)/MWCNT Nanocomposites and Characterization for Investigation of Structural Effects of Carbon Nanotubes. *Bull. Mater. Sci.* **2011**, *34* (1), 37–43. https://doi.org/10.1007/s12034-011-0049-9.

(198) Miraqyan, N. A.; Arakelyan, R. H.; Durgaryan, N. A.; Durgaryan, A. H. Synthesis and Investigation of Poly(p-Phenylenediamine)–Poly(1,4-Benzoquinonediimine-N,N-Diyl-1,4-Phenylene). *Chem. Pap.* **2018**, *72* (6), 1517–1524. https://doi.org/10.1007/s11696-017-0378-2.

(199) Part, I. Soc. (b), 1969. **1969**, No. 818, 818–822.

(200) Song, Y.; Zhu, S.; Zhang, S.; Fu, Y.; Wang, L.; Zhao, X.; Yang, B. Investigation from Chemical Structure to Photoluminescent Mechanism: A Type of Carbon Dots from the Pyrolysis of Citric Acid and an Amine. *J. Mater. Chem. C* **2015**, *3* (23), 5976–5984. https://doi.org/10.1039/c5tc00813a.

(201) He, J.; He, Y.; Chen, Y.; Zhang, X.; Hu, C.; Zhuang, J.; Lei, B.; Liu, Y. Construction and Multifunctional Applications of Carbon Dots/PVA Nanofibers with Phosphorescence and Thermally Activated Delayed Fluorescence. *Chem. Eng. J.* **2018**, *347* (January), 505–513. https://doi.org/10.1016/j.cej.2018.04.110.

(202) Laws, W. R.; Contino, P. B. Fluorescence Quenching Studies: Analysis of Nonlinear Stern-Volmer Data. *Methods Enzymol.* **1992**, *210* (C), 448–463. https://doi.org/10.1016/0076-6879(92)10023-7.

(203) Yuan, W. Z.; Shen, X. Y.; Zhao, H.; Lam, J. W. Y.; Tang, L.; Lu, P.; Wang, C.; Liu, Y.; Wang, Z.; Zheng, Q.; Sun, J. Z.; Ma, Y.; Tang, B. Z. Crystallization-Induced Phosphorescence of Pure Organic Luminogens at Room Temperature. J. Phys. Chem. 2010, 114, 6090–6099.

(204) Gong, Y.; Zhao, L.; Peng, Q.; Fan, D.; Yuan, W. Z.; Zhang, Y.; Tang, B. Z. Crystallization-Induced Dual Emission from Metal- and Heavy Atom-Free Aromatic Acids and Esters. Chem. Sci. 2015, 6 (8), 4438–4444.

(205) Jiang, K.; Zhang, L.; Lu, J.; Xu, C.; Cai, C.; Lin, H. Triple-Mode Emission of Carbon Dots: Applications for Advanced Anti-Counterfeiting. Angew. Chem. Int. Ed. 2016, 128, 7347–7351.

(206) Xiang, Y.; Zhao, Y.; Xu, N.; Gong, S.; Ni, F.; Wu, K.; Luo, J.; Xie, G.; Lu, Z. H.; Yang, C. Halogen-Induced Internal Heavy-Atom Effect Shortening the Emissive Lifetime and Improving the Fluorescence Efficiency of Thermally Activated Delayed Fluorescence Emitters. J. Mater. Chem. C 2017, 5 (46), 12204–12210.

(207) Kwon, M. S.; Lee, D.; Seo, S.; Jung, J.; Kim, J. Tailoring Intermolecular Interactions for Efficient Room-Temperature Phosphorescence from Purely Organic Materials in Amorphous Polymer Matrices. Angew. Chem. Int. Ed. 2014, 53 (42), 11177–11181.

(208) Wang, J.; Gu, X.; Ma, H.; Peng, Q.; Huang, X.; Zheng, X.; Sung, S. H. P.; Shan, G.; Lam, J. W. Y.; Shuai, Z.; Tang, B. Z. A Facile Strategy for Realizing Room Temperature Phosphorescence and Single Molecule White Light Emission. Nat. Commun. 2018, 9 (1), 1–9.

(209) Shimizu, M.; Shigitani, R.; Nakatani, M.; Kuwabara, K.; Miyake, Y.; Tajima, K.; Sakai, H.; Hasobe, T. Siloxy Group-Induced Highly Efficient Room Temperature Phosphorescence with Long Lifetime. J. Phys. Chem. C 2016, 120 (21), 11631–11639.

(210) Yang, L.; Wang, X.; Zhang, G.; Chen, X.; Zhang, G.; Jiang, J. Aggregation-Induced Intersystem Crossing: A Novel Strategy for Efficient Molecular Phosphorescence. Nanoscale 2016, 8 (40), 17422–17426.

(211) Chen, H.; Ma, X.; Wu, S.; Tian, H. A Rapidly Self-Healing Supramolecular Polymer Hydrogel with Photostimulated Room-Temperature Phosphorescence Responsiveness. Angew. Chem. Int. Ed. 2014, 53 (51), 14149–14152.

(212) Kwon, M. S.; Yu, Y.; Coburn, C.; Phillips, A. W.; Chung, K.; Shanker, A.; Jung, J.; Kim, G.; Pipe, K.; Forrest, S. R.; Youk, J. H.; Gierschner, J.; Kim, J. Suppressing molecular

motions for enhanced room-temperature phosphorescence of metal-free organic materials. Nat. Commun. 2015, 6, 8947-8955.

(213) Tan, J.; Zhang, J.; Li, W.; Zhang, L.; Yue, D. Synthesis of Amphiphilic Carbon Quantum Dots with Phosphorescence Properties and Their Multifunctional Applications. J. Mater. Chem. C 2016, 4, 10146–10153.

(214) Tan, J.; Zou, R.; Zhang, J.; Li, W.; Zhang, L.; Yue, D. Large-Scale Synthesis of N-Doped Carbon Quantum Dots and Their Phosphorescence Properties in a Polyurethane Matrix. Nanoscale 2016, 8 (8), 4742–4747.

(215) Deng, Y; Zhao, D.; Chen, X; Wang, Fei; Song, H; Shen, D. Long Lifetime Pure Organic Phosphorescence Based on Water Soluble Carbon Dots. Chem. Commun. 2013, 49, 5751–5753.

(216) Charlesworth, J. M. Optical Sensing of Oxygen Using Phosphorescence Quenching. Sensors Actuators B. Chem. 1994, 22 (1), 1–5.

(217) Chan, M. A.; Lawless, J. L.; Lam, S. K.; Lo, D. Fiber Optic Oxygen Sensor Based on Phosphorescence Quenching of Erythrosin B Trapped in Silica-Gel Glasses. Anal. Chim. Acta 2000, 408 (1–2), 33–37.

(218) Badía, R.; Díaz-García, M. E.; García-Fresnadillo, A. A Sensitive Probe for Oxygen Sensing in Gas Mixtures, Based on Room-Temperature Phosphorescence Quenching. Mikrochim. Acta 1995, 121 (1–4), 51–61.

(219) Zhang, G.; Palmer, G. M.; Dewhirst, M. W.; Fraser, C. L. A Dual-Emissive-Materials Design Concept Enables Tumour Hypoxia Imaging. Nat. Mater. 2009, 8 (9), 747–751.

(220) DeRosa, C. A.; Seaman, S. A.; Mathew, A. S.; Gorick, C. M.; Fan, Z.; Demas, J. N.; Peirce, S. M.; Fraser, C. L. Oxygen Sensing Difluoroboron β-Diketonate Polylactide Materials with Tunable Dynamic Ranges for Wound Imaging. ACS Sensors 2016, 1 (11), 1366–1373.

(221) Sayre, R. M.; Dowdy, J. C.; Gerwig, A. J.; Shields, W. J.; Lloyd, R. V. Unexpected Photolysis of the Sunscreen Octinoxate in the Presence of the Sunscreen Avobenzone. Photochem. Photobiol. 2005, 81 (2), 452-456.

(222) Armagan, E.; Thiyagarajan, S.; Wei, K.; Gursoy, A.; Fortunato, G.; Amstad, E.; Rossi, R. M.; Toncelli, C. Reversible Oxygen Sensing Based on Multi-Emission Fluorescence Quenching. Sensors (Switzerland) 2020, 20 (2), 477-490.

(223) Ronova, I. A.; Bruma, M.; Schmidt, H. W. Conformational Rigidity and Dielectric Properties of Polyimides. Struct. Chem. 2012, 23 (1), 219–226.

(224) Kanosue, K.; Ando, S. Polyimides with Heavy Halogens Exhibiting Room-Temperature Phosphorescence with Very Large Stokes Shifts. ACS Macro Lett. 2016, 5 (12), 1301–1305.

(225) Kanosue, K.; Hirata, S.; Vacha, M.; Augulis, R.; Gulbinas, V.; Ishige, R.; Ando, S. A Colorless Semi-Aromatic Polyimide Derived from a Sterically Hindered Bromine-Substituted Dianhydride Exhibiting Dual Fluorescence and Phosphorescence Emission. Mater. Chem. Front. 2019, 3 (1), 39–49.

(226) Kim, T.; Park, B.; Lee, K. M.; Joo, S. H.; Kang, M. S.; Yoo, W. C.; Kwak, S. K.; Kim, B. S. Hydrothermal Synthesis of Composition- and Morphology-Tunable Polyimide-Based Microparticles. ACS Macro Lett. 2018, 7 (12), 1480–1485.

(227) Zeng, D. W.; Yung, K. C.; Xie, C. S. XPS Investigation of the Chemical Characteristics of Kapton Films Ablated by a Pulsed TEA CO2 Laser. Surf. Coatings Technol. 2002, 153 (2–3), 210–216.

(228) Yang, G.; Han, H.; Du, C.; Luo, Z.; Wang, Y. Facile Synthesis of Melamine-Based Porous Polymer Networks and Their Application for Removal of Aqueous Mercury Ions. Polymer (Guildf). 2010, 51 (26), 6193–6202.

(229) Barshilia, H. C.; Ananth, A.; Gupta, N.; Anandan, C. Superhydrophobic Nanostructured Kapton® Surfaces Fabricated through Ar + O 2 Plasma Treatment: Effects of Different Environments on Wetting Behaviour. Appl. Surf. Sci. 2013, 268, 464–471.

(230) Kanosue, K.; Hirata, S.; Vacha, M.; Augulis, R.; Gulbinas, V.; Ishige, R.; Ando, S. A Colorless Semi-Aromatic Polyimide Derived from a Sterically Hindered Bromine-Substituted Dianhydride Exhibiting Dual Fluorescence and Phosphorescence Emission. Mater. Chem. Front. 2019, 3 (1), 39–49.

(231) Jiang, K.; Zhang, L.; Lu, J.; Xu, C.; Cai, C.; Lin, H. Triple-Mode Emission of Carbon Dots: Applications for Advanced Anti-Counterfeiting. Angew. Chem. Int. Ed. 2016, 55 (25), 7231–7235.

(232) Kelly, C. A.; Toncelli, C.; Cruz-Romero, M.; Arzhakova, O. V.; Kerry, J. P.; Papkovsky, D. B. Phosphorescent O2sensors integrated in polymeric film materials bylocal solvent crazing. Materials and Design 2015, 77, 110–113.

(233) Zhang, G.; Chen, J.; Payne, S. J.; Kooi, S. E.; Demas, J. N.; Fraser, C. L. Multi-Emissive Difluoroboron Dibenzoylmethane Polylactide Exhibiting Intense Fluorescence and Oxygen-Sensitive Room-Temperature Phosphorescence. J. Am. Chem. Soc. 2007, 129 (29), 8942–8943.

(234) Chu, C. S.; Che, A. L. Optical fiber sensor for dual sensing of temperature and oxygen basedon PtTFPP/CF embedded in sol–gel matrix. Sensors and Actuators B 2014, 195, 259-265.

(235) Gaume, J.; Wong-Wah-Chung, P.; Rivaton, A.; Thérias, S.; Gardette, J. L. Photochemical Behavior of PVA as an Oxygen-Barrier Polymer for Solar Cell Encapsulation. RSC Adv. 2011, 1 (8), 1471–1481.

(236) Obeidat, Y. M.; Evans, A. J.; Rivaton, A.; Tedjo, W.; Chicco, A. J.; Carnevale, E.; Chen, T. W. Monitoring oocyte/ embryo Respiration Using Electrochemical-based Oxygen Sensors. Sensors and Actuators B 2018, 276, 72–81.

(237) Stedim, S. Innovations in Cell Culture New Flexsafe Bag Family . **2014**, *12*.

(238) Trivellin, N.; Barbisan, D.; Badocco, D.; Pastore, P.; Meneghesso, G.; Meneghini, M.; Zanoni, E.; Belgioioso, G.; Cenedese, A. Study and Development of a Fluorescence Based Sensor System for Monitoring Oxygen in Wine Production: The WOW Project. *Sensors (Switzerland)* **2018**, *18* (4). https://doi.org/10.3390/s18041130.

(239) Wang, Q.; Jing, J. Y.; Zhao, W. M.; Fan, X. C.; Wang, X. Z. A Novel Fiber-Based Symmetrical Long-Range Surface Plasmon Resonance Biosensor with High Quality Factor and Temperature Self-Reference. *IEEE Trans. Nanotechnol.* **2019**, *18*, 1137–1143. https://doi.org/10.1109/TNANO.2019.2947697.

(240) Wu, S.; Wu, S.; Yi, Z.; Zeng, F.; Wu, W.; Qiao, Y.; Zhao, X.; Cheng, X.; Tian, Y. Hydrogel-Based Fluorescent Dual PH and Oxygen Sensors Loaded in 96-Well Plates for High-Throughput Cell Metabolism Studies. *Sensors (Switzerland)* **2018**, *18* (2). https://doi.org/10.3390/s18020564.

(241) Amao, Y. Fundamental Review Probes and Polymers for Optical Sensing of Oxygen. **2003**, *12*, 1–12. https://doi.org/10.1007/s00604-003-0037-x.

(242) Papkovsky, D. B. Luminescent Porphyrins as Probes for Optical (Bio)Sensors. *Sensors Actuators B. Chem.* **1993**, *11* (1–3), 293–300. https://doi.org/10.1016/0925-4005(93)85267-E.

(243) Peterson, J. I.; Fitzgerald, R. V.; Buckhold, D. K. Fiber-Optic Probe for in Vivo Measurement of Oxygen Partial Pressure. *Anal. Chem.* **1984**, *56* (1), 62–67. https://doi.org/10.1021/ac00265a017.

(244) Tsukada, K.; Sakai, S.; Hase, K.; Minamitani, H. Development of Catheter-Type Optical Oxygen Sensor and Applications to Bioinstrumentation. *Biosens. Bioelectron.* **2003**, *18* (12), 1439–1445. https://doi.org/10.1016/S0956-5663(03)00072-1.

(245) Healey, B. G.; Walt, D. R. Improved Fiber-Optic Chemical Sensor for Penicillin. *Anal. Chem.* **1995**, *67* (24), 4471–4476. https://doi.org/10.1021/ac00120a007.

(246) Vander Donckt, E.; Camerman, B.; Herne, R.; Vandeloise, R. Fibre-Optic Oxygen Sensor Based on Luminescence Quenching of a Pt(II) Complex Embedded in Polymer Matrices. *Sensors Actuators, B Chem.* **1996**, *32* (2), 121–127. https://doi.org/10.1016/0925-4005(96)80120-1.

(247) Otto, S.; Volmer, M.; Fluoreszenz, A. Der. Otto Sterns Veröffentlichungen – Band 2. *Otto Sterns Veröffentlichungen – Band 2* **2016**, *188* (1919), 79–80. https://doi.org/10.1007/978-3-662-46962-0.

(248) Wolf, C.; Tscherner, M.; Köstler, S. Ultra-Fast Opto-Chemical Sensors by Using Electrospun Nanofibers as Sensing Layers. *Sensors Actuators, B Chem.* **2015**, *209*, 1064–1069. https://doi.org/10.1016/j.snb.2014.11.070.

(249) Greiner, A.; Wendorff, J. H. Electrospinning: A Fascinating Method for the Preparation of Ultrathin Fibers. *Angew. Chemie Int. Ed.* **2007**, *46* (30), 5670–5703. https://doi.org/10.1002/anie.200604646.

(250) Wang, Y.; Li, B.; Zhang, L.; Zuo, Q.; Li, P.; Zhang, J.; Su, Z. High-Performance Oxygen Sensors Based on EuIII Complex/Polystyrene Composite Nanofibrous Membranes

Prepared by Electrospinning. *Chem Commun* **2011**, *12* (39), 5868–5870. https://doi.org/10.1002/cphc.201000884.

(251) Yingkui, L. High Performance Oxygen Sensing Nanofibrous Membranes of Eu(III) Complex/Polystyrene Prepared by Electrospinning. *Spectrochim. Acta - Part A Mol. Biomol. Spectrosc.* **2011**, *79* (2), 356–360. https://doi.org/10.1016/j.saa.2011.03.012.

(252) Wang, X.; Yang, Y.; He, B. Improving Oxygen Sensing Performance of Ir(III) Complexes with Fluorine Atoms: Synthesis, Characterization and Sensing Behavior of Their Electrospinning Fibrous Films. *Sensors Actuators, B Chem.* **2017**, *241*, 957–966. https://doi.org/10.1016/j.snb.2016.11.001.

(253) Songzhu, L.; Xiangting, D.; Jinxian, W.; Guixia, L.; Wenshen, Y.; Ruokun, J. Fabrication of Eu(III) Complex Doped Nanofibrous Membranes and Their Oxygen-Sensing Properties. *Spectrochim. Acta - Part A Mol. Biomol. Spectrosc.* **2010**, *77* (4), 885–889. https://doi.org/10.1016/j.saa.2010.08.025.

(254) Gursoy, A.; Iranshahi, K.; Wei, K.; Tello, A.; Armagan, E.; Boesel, L. F.; Sorin, F.; Rossi, R. M.; Defraeye, T.; Toncelli, C. Facile Fabrication of Microfluidic Chips for 3D Hydrodynamic Focusing and Wet Spinning of Polymeric Fibers. *Polymers (Basel).* **2020**, *12* (3). https://doi.org/10.3390/polym12030633.

(255) Cheng, J.; Jun, Y.; Qin, J.; Lee, S. H. Electrospinning versus Microfluidic Spinning of Functional Fibers for Biomedical Applications. *Biomaterials* **2017**, *114*, 121–143. https://doi.org/10.1016/j.biomaterials.2016.10.040.

(256) Hu, M.; Kurisawa, M.; Deng, R.; Teo, C. M.; Schumacher, A.; Thong, Y. X.; Wang, L.; Schumacher, K. M.; Ying, J. Y. Cell Immobilization in Gelatin-Hydroxyphenylpropionic Acid Hydrogel Fibers. *Biomaterials* **2009**, *30* (21), 3523–3531. https://doi.org/10.1016/j.biomaterials.2009.03.004.

(257) Oh, J.; Kim, K.; Won, S. W.; Cha, C.; Gaharwar, A. K.; Selimović, Š.; Bae, H.; Lee, K. H.; Lee, D. H.; Lee, S. H.; Khademhosseini, A. Microfluidic Fabrication of Cell Adhesive Chitosan Microtubes. *Biomed. Microdevices* **2013**, *15* (3), 465–472. https://doi.org/10.1007/s10544-013-9746-z.

(258) Lee, K. H.; Shin, S. J.; Kim, C. B.; Kim, J. K.; Cho, Y. W.; Chung, B. G.; Lee, S. H. Microfluidic Synthesis of Pure Chitosan Microfibers for Bio-Artificial Liver Chip. *Lab Chip* **2010**, *10* (10), 1328–1334. https://doi.org/10.1039/b924987g.

(259) Shin, S. J.; Park, J. Y.; Lee, J. Y.; Park, H.; Park, Y. D.; Lee, K. B.; Whang, C. M.; Lee, S. H. "On the Fly" Continuous Generation of Alginate Fibers Using a Microfluidic Device. *Langmuir* **2007**, *23* (17), 9104–9108. https://doi.org/10.1021/la700818q.

(260) Onoe, H.; Takeuchi, S. Cell-Laden Microfibers for Bottom-up Tissue Engineering. *Drug Discov. Today* **2015**, *20* (2), 236–246. https://doi.org/10.1016/j.drudis.2014.10.018.

(261) Jun, Y.; Kang, E.; Chae, S.; Lee, S. H. Microfluidic Spinning of Micro- and Nano-Scale Fibers for Tissue Engineering. *Lab Chip* **2014**, *14* (13), 2145–2160. https://doi.org/10.1039/c3lc51414e.

(262) Armagan, E.; Wei, K.; Fortunato, G.; Amstad, E.; Rossi, R. M. Reversible and Broad-Range Oxygen Sensing Based on Purely Organic Long-Lived Photoemitters. *ACS Appl. Polym. Mater.* **2021**, *3* (5), 2480–2488. https://doi.org/10.1021/acsapm.1c00064.

(263) Qin, X. H.; Labuda, K.; Chen, J.; Hruschka, V.; Khadem, A.; Liska, R.; Redl, H.; Slezak, P. Development of Synthetic Platelet-Activating Hydrogel Matrices to Induce Local Hemostasis. *Adv. Funct. Mater.* **2015**, *25* (42), 6606–6617. https://doi.org/10.1002/adfm.201501637.

(264) Qin, X. H.; Wang, X.; Rottmar, M.; Nelson, B. J.; Maniura-Weber, K. Near-Infrared Light-Sensitive Polyvinyl Alcohol Hydrogel Photoresist for Spatiotemporal Control of Cell-Instructive 3D Microenvironments. *Adv. Mater.* **2018**, *30* (10), 1–7. https://doi.org/10.1002/adma.201705564.

(265) Chau, A. L.; Cavanaugh, M. K.; Chen, Y. T.; Pitenis, A. A. A Simple Contact Mechanics Model for Highly Strained Aqueous Surface Gels. *Exp. Mech.* **2021**, *61* (4), 699–703. https://doi.org/10.1007/s11340-021-00699-5.

(266) Lee, J. H.; Lee, S. S.; Chang, J. D.; Thompson, M. S.; Kang, D. J.; Park, S.; Park, S. A Novel Method for the Accurate Evaluation of Poisson's Ratio of Soft Polymer Materials. *Sci. World J.* **2013**, *2013*. https://doi.org/10.1155/2013/930798.

(267) Charlesworth, J. M. Optical Sensing of Oxygen Using Phosphorescence Quenching. *Sensors Actuators B. Chem.* **1994**, *22* (1), 1–5. https://doi.org/10.1016/0925-4005(94)01263-6.

(268) Morimoto, Y.; Hsiao, A. Y.; Takeuchi, S. Point-, Line-, and Plane-Shaped Cellular Constructs for 3D Tissue Assembly. *Adv. Drug Deliv. Rev.* **2015**, *95*, 29–39. https://doi.org/10.1016/j.addr.2015.09.003.

(269) Kelly, C. A.; Toncelli, C.; Cruz-Romero, M.; Arzhakova, O. V.; Kerry, J. P.; Papkovsky, D. B. Phosphorescent O2 Sensors Integrated in Polymeric Film Materials by Local Solvent Crazing. *Mater. Des.* **2015**, *77*, 110–113. https://doi.org/10.1016/j.matdes.2015.03.045.

(270) Chu, C. S.; Lin, C. A. Optical Fiber Sensor for Dual Sensing of Temperature and Oxygen Based on PtTFPP/CF Embedded in Sol-Gel Matrix. *Sensors Actuators, B Chem.* **2014**, *195*, 259–265. https://doi.org/10.1016/j.snb.2014.01.032.

(271) Bittig, H. C.; Körtzinger, A.; Neill, C.; van Ooijen, E.; Plant, J. N.; Hahn, J.; Johnson, K. S.; Yang, B.; Emerson, S. R. Oxygen Optode Sensors: Principle, Characterization, Calibration, and Application in the Ocean. *Front. Mar. Sci.* **2018**, *4* (JAN), 1–25. https://doi.org/10.3389/fmars.2017.00429.

(272) Lakowicz, J. R.; Weber, G. Quenching of Fluorescence by Oxygen. a Probe for Structural Fluctuations in Macromolecules. *Biochemistry* **1973**, *12* (21), 4161–4170. https://doi.org/10.1021/bi00745a020.